Toward cryogenic beams of nanoparticles and proteins

Dissertation
zur Erlangung des Doktorgrades
an der Fakultät für Mathematik, Informatik und Naturwissenschaften
Fachbereich Physik
der Universität Hamburg

vorgelegt von

Lena Worbs

Hamburg

2022

Gutachter der Dissertation:	Prof. Dr. Jochen Küpper Prof. Dr. Holger Lange
Zusammensetzung der Prüfungskommission:	Prof. Dr. Jochen Küpper Prof. Dr. Holger Lange Prof. Dr. Arwen Pearson Dr. Amit K. Samanta Prof. Dr. Michael Potthoff
Vorsitzende/r der Prüfungskommission:	Prof. Dr. Michael Potthoff
Datum der Disputation:	17.10.2022
Vorsitzender Fach-Promotionsausschusses PHYSIK:	Prof. Dr. Wolfgang J. Parak
Leiter des Fachbereichs PHYSIK:	Prof. Dr. Günter H. W. Sigl
Dekan der Fakultät MIN:	Prof. Dr.-Ing. Norbert Ritter

Abstract

To determine the structure of (bio-)nanoparticles, and possibly, the dynamics and function of it, the ultrashort and bright pulses generated from x-ray free-electron lasers can be used. X-ray free-electron lasers provide x-ray pulses with pulse durations of a few tens of femtoseconds and high photon numbers, sufficiently high to record scattering off a single macromolecule. This method of imaging is called single-particle diffractive imaging. The ultrashort pulses outrun radiation damage and an intact particle is imaged. This promising technique has one bottleneck: sample injection. Currently, the output of the experiments is limited by a low number of collected diffraction patterns and a low hit rate. The (bio-)nanoparticles are injected into the x-ray beam with aerosol injectors consisting of an aerosolization source and an aerodynamic lens stack to generate a continuous stream of nanoparticles. One concern despite the low hit rate in these experiments is the purity of the particle beam, that is consisting of clusters of nanoparticles, different charge states and spatial conformers. Within this thesis, sample delivery methods are improved toward the overall goal of imaging single proteins. To study the injector properties, a novel particle-beam characterization method to image the transverse particle beam profile is presented, capable of characterizing the particle flux and the particles' velocity from an aerodynamic lens stack injector. Improvements on the aerosol sample delivery are made based on existing aerosol injectors to improve the hit rate through better particle focusing. Using simulations, the optimization of the geometry is performed efficiently. The optimized injector geometry is implemented in the setup and used for generating a particle beam of gold nanoparticles. Toward the aim of imaging single proteins, important steps are taken in understanding the particle-beam formation for smaller nanoparticles using particle trajectory calculations and extending the particle-beam detection towards smaller nanoparticles using optical scattering. Another crucial step in sample delivery is taken by generating a particle beam consisting of shock-frozen sub-100 nm particles, opening up the path toward a sample delivery setup that is capable of providing a pure particle beam for single-particle imaging experiments.

Zusammenfassung

Um die Struktur von (Bio-)Nanoteilchen, sowie ihre Dynamik und Funktion zu bestimmen, können ultrakurze und brillante Pulse genutzt werden, die von Röntgen-Freie-Elektronen-Lasern erzeugt werden. Freie-Elektronen-Laser erzeugen Röntgenpulse mit Pulsdauern von einigen zehn Femtosekunden und hohen Photonenzahlen, hoch genug, um Streuung von einem Makromolekül zu detektieren. Diese Abbildungsmethode wird *single-particle diffractive imaging* genannt. Die ultrakurzen Pulse sind kurz genug, um ein Streubild zu erzeugen, bevor Strahlungsschäden in den Nanoteilchen entstehen. Diese vielversprechende Methode hat eine Schwierigkeit: die Injektion der Teilchen. In den meisten Fällen ist das Resultat dieser Experimente durch eine geringe Anzahl von Streubildern limitiert. Gegenwärtig werden die (Bio-)Nanoteilchen mit einem Aerosolinjektor in den Röntgenstrahl gebracht. Dieser Aufbau besteht aus einer Aeorosolquelle und einer aerodynamischen Linse, um einen kontinuierlichen Teilchenstrahl zu erzeugen. Neben der Hitrate spielt auch die Reinheit des Teilchenstrahls eine große Rolle. Es können Cluster, verschiedene Ladungszustände oder auch Konformere vorhanden sein. Innerhalb dieser Arbeit werden die Injektionsmethoden verbessert, um dem Ziel der Strukturabbildung von einzelnen Proteinen näher zu kommen. Um die Injektorparameter zu beurteilen, wird eine neue Methode zur Strahlcharakterisierung präsentiert, die das transversale Strahlprofil abbildet und den Teilchenfluss und die Geschwindigkeit der Teilchen bestimmen kann. Verbesserungen an einem existierenden Aerosolinjektor werden gemacht, um die Hitrate durch bessere Teilchenstrahlerzeugung, zu erhöhen. Mit Hilfe von Simulationen wird die Geometrie der aerodynamischen Linse effizient optimiert. Der optimierte Injektor wird in dem experimentellen Aufbau realisiert und für die Teilchenstrahlerzeugung von Goldnanoteilchen benutzt. Um dem Ziel von der Abbildung einzelner Proteine näher zu kommen, wird die Teilchenstrahlerzeugung für kleinere Nanoteilchen untersucht und durch simulierte Teilchentrajektorien verstanden. Der Aufbau wird verbessert, um mit optischer Streuung kleine Nanoteilchen detektieren zu können. Ein weiterer wichtiger Schritt ist die Erzeugung von schockgefrorenen Nanoteilchen von weniger als 100 nm Durchmesser. Diese bereiten den Weg für Probeninjektionsaufbauten, die reine Strahlen von Nanoteilchen für *single-particle imaging* Experimente erzeugen können.

Contents

Chapter 1

Introduction

Understanding processes in nature on different scales in space and time is motivating research and developments in all fields including biology, chemistry and physics. From the overall growth process of a plant on a centimeter to meter length scale and time scales of days and weeks to several years down to the process of photosynthesis involving the functional units of the protein complexes absorbing light inside the leaves of the plants on a nanometer length scale and femtosecond time scale, all processes are of interest to understand nature around us and to create a complete image. Especially biophysics, biochemistry and structural biology rely on imaging the structure and the dynamics of biologically relevant building blocks of nature, such as proteins and biological (macro-) molecules with atomic resolution, i. e., with sub-nanometer spatial and femtosecond temporal resolution to address key challenges in each field. Imaging on an atomic scale and observing how molecules break apart, form new bonds and interact is the idea behind recording a so-called molecular movie [1–3].

Apart from proteins and biological (macro-)molecules, the importance of nanometer-sized particles (NPs) for biological and technical development was recognized. From using magnetic nanoparticles in solar panel fabrication for increased efficiency [4] to linking nanoparticles, especially gold nanoparticles (AuNPs), and important molecules for drug delivery [5], the fundamental research for these developments is resolving structures of a few nanometers, their dynamics and functionality with sub-nanometer ($<10^{-9}$ m) resolution [6], i. e., on an atomic range and observing the dynamic on a femtosecond time scale, i. e., on a time scale of atomic structural changes within the nanostructures. To be able to resolve these spatial and temporal ranges, hard x-ray photons are needed for spatial resolution and femtosecond pulses for the wanted temporal resolution and outrunning radiation damage [7–9].

In life science and biophysics, resolving the structure of a biomolecule or -particle opens the path to their role in a process according to the structure-function-relationship: The structure of a molecule determines its function and therefore, its role in a dynamical biological process. Knowledge about a process gives one the ability to manipulate it to, e. g., suppress the process or on the contrary, increase its efficiency.

Many different ways of resolving the structure of biomolecules and -particles have been developed and used in the past. Determining the atomic composition of isolated gas-phase molecules is achieved through, e. g., native mass spectrometry [10]. To study the structure of relatively small molecules in solution, nuclear magnetic resonance spectroscopy (NMR) can be used [11]. A successful structure determination technique is x-ray crystallography, which provides atomic resolution of molecules and proteins that can be crystallized [12]. A drawback of x-ray crystallography is the need for large crystals and most of biologically relevant proteins, especially membrane proteins, cannot be crystallized. To mitigate radiation damage on the proteins within the crystal due to the

energy deposition from the x-ray photons that do not scatter, the crystals are cooled to cryogenic temperatures, increasing complexity of the experiment.

A similar resolution can be achieved in cryo-electron microscopy (CEM), where a record-breaking resolution of 0.125 nm has been presented for apoferritin [13]. In CEM, there is no need for crystallization and single molecules are deposited on a grid directly from solution. However, the molecules are immobilized on the grid for imaging, limiting the imaging to static structures without dynamics. CEM is advancing in availability at research centers and is imaging more and more structures that cannot be crystallized with high resolution [14]. Recent advances in single-particle CEM are enabling the generation of numerous near-atomic resolution structures breaking barriers to facilitate drug discovery [15].

With the advent of experiments at x-ray free-electron lasers (XFELs), such as the Linac Coherent Light Source (LCLS) [16] or the European XFEL (EuXFEL) [17], new experimental methods could be explored and the usage of intense and short x-rays pulses became inherent for structural biology [18]. With the shorter pulse durations of a few tens of femtoseconds and photon numbers of $> 10^{12}$ photons per pulse, the radiation dose on the sample is high, but due to the short pulse duration, even at high photon numbers and energies, atomic scattering factors and positions can be retrieved close to a structure without radiation damage. This principle is called diffraction-before-destruction [7, 19]. As a consequence of higher photon flux, the scattering signal is increasing, meaning the crystal size and the number of scatterers that contribute to the coherent scattering signal can be reduced. This realization opened the field of reducing the crystal size to nanocrystals (crystal size < 1 µm, 1 µm $= 10^{-6}$ m). With smaller crystals the scattering signal is high enough and due to the deposited energy by the x-rays the nanocrystal is destroyed. As this nanocrystal would produce a radiation damaged image of the sample, a new nanocrystal must be present in the interaction region when the next x-ray pulse arrives. To replace the nanocrystal, a stream of a nanocrystal suspension acts as sample delivery method. This method of serial femtosecond crystallography (SFX) yields high resolution structure results with room-temperature nanocrystals [20–24]. Reducing the sample size to one single protein may be possible by injection the sample-buffer-solution directly, but recording a scattering signal from that one protein alone in solution is impossible. The scattering signal will vanish in the background solvent scattering.

Another approach is the idea of imaging those proteins and nanoparticles isolated from their environment in the gas-phase [25]. In addition to a background-free scattering signal, no environment-effects on the dynamics are expected and the protein structure can be explored individually. The diffraction-before-destruction principle still remains valid for isolated macromolecules [7]. The principle of single-particle diffractive imaging (SPI), past and future developments and challenges are discussed in the following paragraphs.

X-ray pulses generated at XFELs are well-suited for structure determination of an isolated bioparticle in gas-phase. Due to the high photon energies in the soft and hard x-ray regime and short pulse durations, the diffraction pattern from a single isolated bioparticle can be recorded [26]. In contrast to crystallography, in SPI single isolated particles are imaged to determine the structure factors. Without the need for crystals, more bioparticles and especially membrane proteins that do not crystallize can be imaged. In SPI, an x-ray pulse is interacting with an isolated particle in gas-phase. The x-ray photon energy is typically in the hard x-ray regime (photon energy $E_{\mathrm{ph}} > 5 \ldots 10$ keV). During the illumination of the bioparticle with the x-ray pulse, not only elastic scattering occurs, but also the absorption of photons and the deposited energy forces the particle to break apart due to ionization and charge repulsion. The scattered photons are detected on a position sensitive detector. From the recorded diffraction patterns the particle structure can be retrieved as follows: First, the orientation of the randomly oriented particle has to be determined and the oriented patterns are merged with iterative phasing into a diffraction volume. From this phased

diffraction volume, the electron density map of the particle can be determined. However, thousands of diffraction patterns are necessary due to the low signal strength. A recent computational study estimates the amount of diffraction patterns for a protein to be in the order of $10^5 - 10^6$ diffraction patterns for a 0.3 nm resolution depending on the x-ray beam parameters [27]. As every particle is destroyed by the x-ray pulse, a continuous stream of particles has to be generated.

Imaging of isolated (biological) particles has been demonstrated on different samples, e. g., large viruses, such as the Mimivirus ($d = 450$ nm) [28], Melbourne virus ($d \approx 200$ nm) [29] and PR772 bacteriophage ($d = 70$ nm) [30] and sucrose particles [31] and AuNPs [32].

Due to improvements in sample delivery, the particles imaged via SPI got smaller in size in recent years, starting from larger viruses down to protein complexes [33]. In order to resolve structures like these with higher resolution, sample delivery is the bottleneck and improvements on the experimental sample delivery have to be addressed [34]. Especially for smaller bioparticles, the hit rate is very low due to inefficient sample delivery and high background signal. In this context, hit rate is understood as the percentage of detector images containing a useful diffraction image from the sample.

To bring the sample initially suspended in an evaporative buffer solution into the interaction region it is aerosolized and aerodynamically focused into a particle beam that is intersected by the focus of the x-ray beam.

One requirement for SPI is the preparation of particles such that the particles are present in the interaction region with an x-ray pulse as isolated, but hydrated and intact particles in their native structure in vacuum. *Isolated* corresponds to the interaction of the particles with other particles or with being present in a solution, *intact* refers to their (biological) function and the *native* structure is the structure the particles have in their functional structure, e. g. the native protein structure is referred to as the folded and functional 3D structure of a protein. During aerosolization and transition into vacuum, this structural change has to be considered, or rather methods should be used to avoid these structural changes. Aerosolization methods typically leave a thin layer of solution around the sample. Those hydrated sample particles are imaged and if the layer is below 1 nm thin, no increasing effect of radiation damage on the sample due to the layer is to be expected and the diffraction pattern contains information about the small and high resolution features [35]. Once the particles are in vacuum and illuminated with an intense x-ray pulse, the particles are destroyed by the deposited energy. This requires a constant delivery of particles into the interaction region. In an ideal case, each x-ray pulse is interacting with one - and only one - particle and a diffraction pattern is recorded, but in reality, the hit rates are way below this ideal case with typically below 1 %. This shows the main problem: this small hit rate corresponds to sample waste, which may take months to prepare, but also the x-ray pulses are not used efficiently. The bottleneck of improving SPI experiments is, therefore, sample injection, i. e. an increase in hit rate. One way to improve the hit rate is improving the particle-beam generation. The particle beam is typically generated from an aerodynamic lens stack (ALS) [25] Initially, ALS injectors were designed for particle transport of nanoparticles in mass spectrometry and nanoparticle deposition experiments and operated at higher pressures [36, 37]. Adapting the ALS injector to be used for SPI has been demonstrated at LCLS and has been used and improved ever since [34]. Also other fluid dynamics particle-beam injectors, such as a convergent nozzle injector have been demonstrated for injection of nanoparticles into the x-ray beam [38].

In current experiments, creating an aerosol from the particles of interest in an evaporative buffer solution is achieved either via liquid jet breakup aerosolization using a gas-dynamic virtual nozzle [39] or via electrospray ionization [40]. Both methods produce droplets of the buffer solution and those droplets contain ideally one - and only one - particle. With time and when introducing the droplets into vacuum, the droplet dries and the isolated particle is remaining. Both aerosolization

methods use a carrier gas or carrier gas mixture. The amount of gas is reduced before the ALS and the remaining gas is used to aerodynamically focus the particles into a particle beam. One commonly used injector at FELs is the so-called "Uppsala-injector", built from an aerosolization source, a differential pumping stage and an aerodynamic lens stack for focusing particles between 70 and 2000 nm in diameter. It has been used in various experiments at FELs [28–32, 41–44].

Following similar experimental steps, our group put forth an effort to design our own injector similar to the "Uppsala-injector". The crucial difference is that our ALS has been designed to be fully-variable and adjustable [45]. In addition, a simulation framework of the particle trajectories through the ALS carrier-gas flow field has been established [46] and is used throughout this thesis. The fully-variable ALS geometry allows the optimization of the geometry for a specific particle size and density.

While the particle-beam generation for larger nanoparticles with diameters above 50 nm works nicely using these room-temperature ALS injectors, smaller particles suffer from Brownian motion effects, i. e., a broadening of the particle beam due to the stochastic force. Reducing Brownian motion, e. g., by reducing the temperature, and improving the particle-beam generation for small NPs is currently a major challenge in sample delivery.

The need for shock-freezing nanoparticles for SPI experiment originates not only in reducing the effects of Brownian motion, but from structural changes and varieties that are considered impurities in the particle beam, e. g., if a special spatial conformer is of interest. Impurities in the particle beam and thus, collecting diffraction images of the impurities will reduce the resolution of the retrieved 3D structure and should be avoided. Sorting diffraction patterns for impurities in the data analysis part of the experiment is possible if the shape is fundamentally different [47], but otherwise small structural changes will decrease the overall resolution, as the retrieved structure is averaged over all collected diffraction patterns. Structural conformers, clusters, charge states and buffer residues are some examples of impurities that can be present in the interaction region. For small molecules, spatial separation of structural conformers was pioneered in our group with the use of electric fields [48–50]. Starting point of this separation is a cold molecular beam. To create cold particle beams of nanoparticles, the method of using a cryogenic buffer-gas cell (BGC) is adapted from research in atomic physics [51], and had so far not been applied to systems with more than a few tens of atoms [52, 53], until generating a particle beam from a BGC was demonstrated for nanoparticles [54]. In this study, large nanoparticles and virus capsids were used (d>200 nm). A particle beam consisting of shock-frozen nanoparticles at cryogenic temperatures was reported and is used as the starting point for further work toward cold particle beams of smaller nanoparticles within this thesis, working toward imaging of single proteins using SPI.

Outline of this thesis

The main objective of the work presented in this thesis was the generation of dense and cyogenically-cooled particle beams containing shock-frozen particles in well defined structures for the use in SPI experiments. In preparation of generating cryogenically-cooled particle beams, the working principle of the room-temperature aerodynamic lens injector was studied and the setup was improved. The knowledge from particle-beam characterization and generation at room-temperatures can be applied to cold particle beams. The presented work is improving sample delivery methods for SPI experiments and is contributing to the path toward imaging a single protein with high resolution at XFELs.

This thesis is organized as follows: chapter 2 provides the fundamental concepts of the work presented in the following chapters. It covers the generation of particle beams for the use in SPI from the aerosolization to the overlap with an x-ray pulse, the in-laboratory characterization

methods and the overall generic setups used. In addition, the simulation framework is explained to simulate and predict the particle beams emerging from the investigated injectors.

The chapters 3 to 6 are the main part of this thesis. They are based on manuscripts published or soon to be published in scientific peer-reviewed journals [55–58].

In chapter 3, a particle-beam characterization method is presented. In contrast to previous work, where the particle beam is observed from the side or the particle beam is destructively measured on microscope slides [59], this method of *light-sheet imaging* (LSI) is able to record the transverse particle-beam profile on the fly and determine the absolute particle number density.

In chapter 4, an optimization procedure for the geometry of an aerodynamic lens stack (ALS) is provided. A previously developed variable geometry ALS was optimized for 50 nm gold nanoparticles (AuNPs) using simulations of the carrier-gas flow field and the particle trajectories. Simulating the particle beam instead of changing the apertures in the experiment and measuring the particle beam properties saves preparation time for experiments significantly.

In chapter 5, the optimized ALS injector from chapter 4 is used to explore the particle-beam generation ability for smaller NPs with sizes down to 25 nm, currently limited by the imaging method. The particle-beam focus position shift is investigated and understood via the particles' simulated phase-space distributions and in terms of aerodynamic focusing parameters.

In chapter 6, the knowledge from previous work is used to generate a cryogenically-cooled particle beam consisting of intermediately sized NPs. By combining a buffer-gas cell with an aerodynamic lens, the generation of cryogenically cooled particle beams was extended to smaller NPs, paving the way toward the generation of particle beams consisting of even smaller NPs and potentially proteins.

In chapter 7, developments and proposed changes on the sample injection toward the injection of 10 nm NPs are presented. The summary is presented in chapter 8.

Chapter 2

Fundamental concepts

This chapter provides an overview of the fundamental concepts used as a basis for the following chapters of this thesis. It covers the particle-beam generation of (small) nanoparticles for single-particle diffractive imaging (SPI) experiments at x-ray free-electron lasers (XFELs) with the goal of imaging the structure and dynamics of proteins without crystallization. In addition to the experimental techniques, ranging from aerosolization methods to particle detection, the simulation framework for predicting the particle-beam formation is described. These predictions are necessary for optimizing the injector geometry and for predicting hit rates and the feasibility of a planned experiment.

2.1 Experimental methods

The sample of interest in SPI experiments comes in solution like water or a specific buffer solution. The imaging itself is performed on isolated, gas-phase sample in vacuum and requires a new particle each FEL shot due to destruction of the sample by the deposited energy [7, 25, 26]. Therefore, a continuous stream of particles needs to be generated with a density in the order of 1 particle/interaction volume/pulse. FEL pulse focusing improved over the past years and reaches focus sizes below 1 µm. As a consequence, the particle-beam size needs to reduce to avoid wasting sample unexposed to the x-ray beam. The pulse duration is expected to be between $10 \ldots 50$ fs. Due to higher achievable repetition rates of the FELs, sample speed has to increase as well to avoid double exposure on the same sample particle from two different FEL pulses, as observed in a recent experiment [32].

In addition to the number of particles imaged, the purity of the sample is crucial for a good resolution. Even though sample preparation can be done carefully, still impurities may remain in the generated particle beam. In order to separate, e. g., spatial conformers, charge states or align the particles, other techniques known for small molecules can be applied to the particle beam before imaging [60]. To achieve, e. g., alignment or conformer separation, the sample may undergo rapid shock-freezing [54].

To bring the sample from solution into gas-phase, the sample is aerosolized using a gas-dynamic virtual nozzle or electrospray ionization. The excess gas from these processes is removed in a differential pumping stage and the remaining gas is used to aerodynamically form a particle beam using an aerodynamic lens stack. For shock-freezing the sample, the buffer-gas cell is introduced and the used particle detection methods are described. These processes, as well as the generic setup and the applications in SPI are described in the following sections.

2.1.1 Nanoparticle-beam generation

The starting point for generating a nanoparticle beam is a sample, e. g., polystyrene spheres, gold nanostructures or bioparticles, suspended in a buffer solution. Typical sample concentrations in the solution are in the order of $10^6 \dots 10^7$ particles/ml when using liquid jet aerosolization and $10^{11} \dots 10^{13}$ particles/ml when using electrospray ionization.

Aerosolization

To aerosolize the sample solution, two different methods are used: the breaking of a gas-focused liquid jet, as produced from a gas-dynamic virtual nozzle (GDVN) [39] or electrospray ionization [40].

The geometry and working principle of a GDVN is shown in Figure 2.1 a. A GDVN consists of an inner and an outer part. The inner part with an inner diameter (ID) of typically 25 µm is used for the liquid sample. The sample is diluted in water and flow rates are typically $1 \dots 3$ µl/min. The inner capillary is surrounded by an outer part through which helium gas is flowing. In combination of the liquid flow and the surrounding gas, a liquid jet with a diameter of typically < 10 µm is formed [39]. The surrounding pressure in the aerosolization chamber is close to atmospheric pressure, but a liquid jet can also be formed in sufficiently low vacuum for direct x-ray imaging of nanocrystals or NPs in the liquid jet [20]. For aerosolization purposes, the stable liquid jet is breaking after a short distance and generating droplets in the diameter range of 1 µm. This method is used for aerosolizing larger nanoparticles above 100 nm in diameter, as the initial droplet diameter is large. Smaller sample would be left with a residue layer of water in the interaction region [61] or with a higher chance of clustering inside the larger droplets. The GDVN performance depends on the glueing of the lines and is therefore not highly reproducible. In past years, efforts were made to make GDVN production more reliable, e. g., using 3D-printed GDVNs [62] or to use GDVNs with lower flow rates, generating smaller initial droplets especially for the use in SPI experiments [63]. Otherwise, liquid jets are the standard tool to generate liquid jets for serial femtosecond crystallography experiments using nanocrystals [20, 23], solution experiments on small molecular water clusters [64] or for generating microjets and observing shear-induced ordering of nanoparticles in the liquid jet [65].

To generate isolated nanoparticles with diameters below 100 nm, electrospray ionization (ESI) is used. Throughout this thesis, a commercial electrospray is used (TSI Advanced Electrospray generator model 3842). The principal setup of an ESI device is shown in Figure 2.1 b. For ESI, the sample is present in an evaporative and conductive solution. Mostly, Ammonium Acetate (AmAc) 20 mM in water is used. The sample flows through a typically $30 \dots 50$ µm ID capillary with an angled tip at flow rates of $150 \dots 600$ nl/min. Nitrogen and CO_2 in a $\approx 90/10$ mixture are surrounding the capillary and in combination with an applied voltage of $1.5 \dots 2.5$ kV forming a Taylor-cone. Due to the electric field, the generated droplets are highly charged and need to be neutralized. Here, a soft x-ray neutralizer is used. The evaporation and charge distribution of the droplets is an ongoing field of research, currently multiple ESI mechanisms are proposed to explain how the charges are distributed and moving inside the droplet [66].

Due to the lower sample flow and the stable Taylor cone spraying conditions, this method produces smaller initial droplets and therefore, creating less residue on the sample in the interaction region [61]. A disadvantage of ESI is the use of nitrogen and CO_2 compared to helium as the scattering cross section is higher in SPI experiments, making it difficult to record signal above the gas background level for small bioparticles [33].

ESI is also used in native mass spectrometry experiments of proteins. In these experiments, no neutralizer is used and the charges are used for guiding the particles into the detection region using electric fields [67, 68].

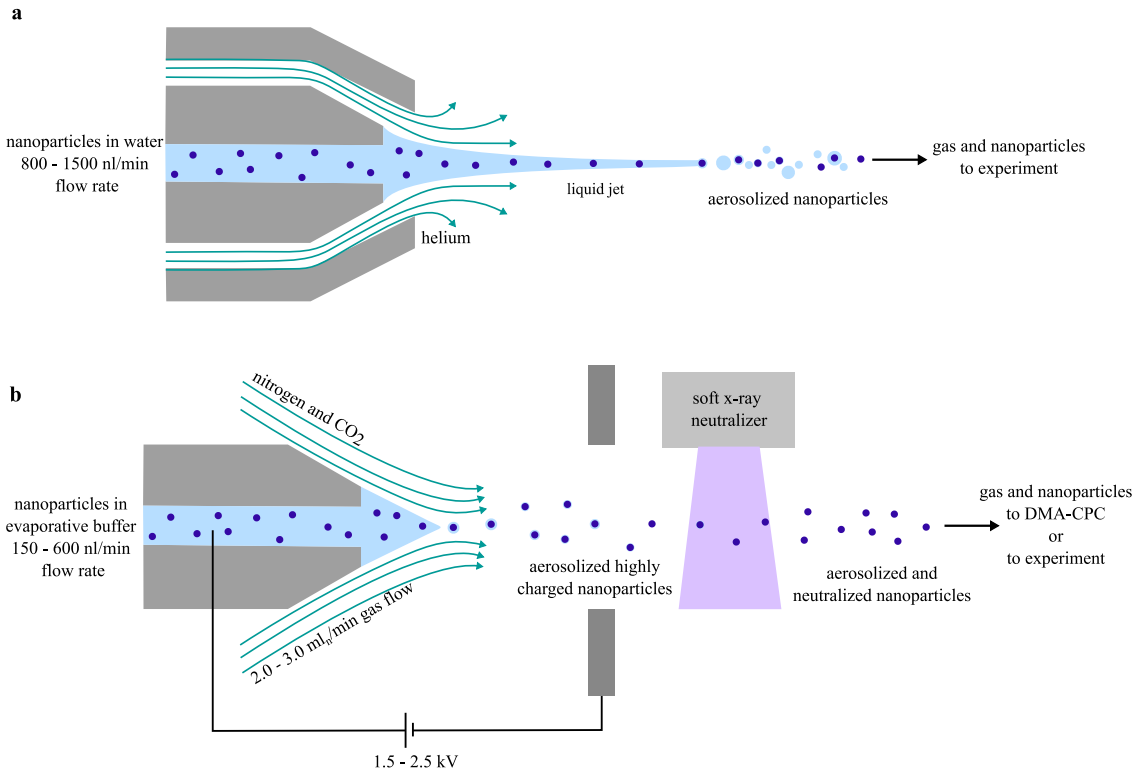

Figure 2.1: a.) Schematic GDVN setup. The sample in water is pushed through a thin capillary. Helium gas flows around the inner capillary tip and forming a liquid jet. The jet is breaking up, forming droplets with around 1 µm diameter. b.) Schematic electrospray ionization setup. The sample in evaporative, conductive buffer is pushed through a capillary with 40 µm ID and nitrogen and CO_2 gas flows around it. Together with an applied electric field, a Taylor cone is forming and small droplets are generated. The aerosol is passing a soft x-ray neutralizer region to neutralize the highly charged droplets.

The generated aerosol and droplet size distribution from both methods can be measured using a differental-mobiliy-analyser (DMA) and a condensation particle counter (CPC). These commercially available devices can be used to optimize sample conditions, such as sample concentration, buffer conductivity, liquid flow rate, etc. to generate particles without a thick layer of water or buffer around it. DMA-CPC measurements can also be used to determine the sample concentration in the solution [69].

Differential pumping

The aerosolization processes both come with a high gas background of helium (for GDVN) and nitrogen and CO_2 (for ESI). Both processes operate under nearly atmospheric pressures. Nitrogen and CO_2 from the ESI process are causing a high scattering background in SPI experiments when using hard x-rays due to an increased scattering cross section. To reduce the amount of gas injected into the interaction region, a differential pumping stage is used consisting of a nozzle-skimmer combination with pumping in between. Typically, the skimmer tips are $2 \ldots 4$ mm apart and the skimmer tip diameters are $0.2 \ldots 1.0$ mm. As the gas mass is way lower than the particle mass, the particles are passing the pumping section with small changes in their trajectories and enter the lower skimmer, whereas the gas is pumped away in between. Using one skimmer combination after the GDVN aerosolization and two skimmer combinations after ESI aerosolization, the pressure is reduced to below 1 mbar, although for some measurements, a higher pressure is used. This is the

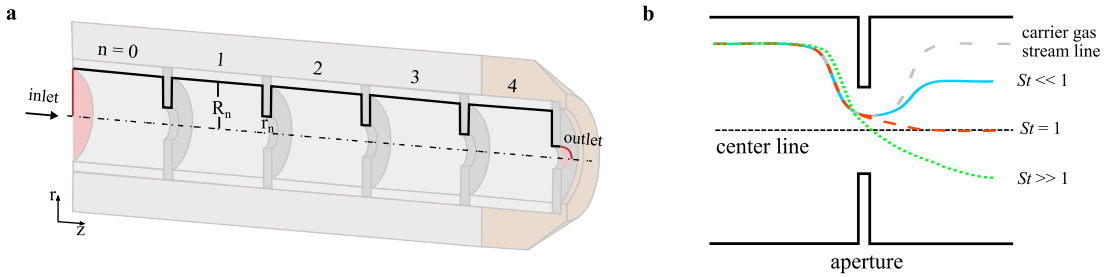

Figure 2.2: a.) Aerodynamic lens geometry. Carrier gas and particle flow is from left to right. The black solid line is the geometry used for simulating the 2D cylindrically symmetric flow field. The apertures and tubes can be changed individually. Taken from own publication [56]. b.) Working principle of focusing at an aperture. The carrier gas stream line is shown in dashed gray. After an aperture, the gas is expanding again to the same distance from the center line. In contrast, the particle trajectory (shown in solid blue) does not expand to the original distance again, but stays at a closer distance due to the particles' higher mass.

pressure after the differential pumping stage and right before the injector.

Nanoparticle focusing

To generate a room-temperature particle beam, an aerodynamic lens stack (ALS) is used [70]. The geometry consists of tubes and apertures. With a higher gas pressure before the ALS (around $0.5 \ldots 2.5$ mbar) and the exit being in low vacuum (below 10^{-5} mbar), the carrier-gas is flowing into the lower pressure region. The apertures cause a contraction of the carrier gas, creating an aerodynamic lens (ADL) effect that can focus particles. The experiments performed in this thesis use a modular ALS injector consisting of 5 tube/aperture pairs that can be changed individually. An illustration of the ALS injector is shown in Figure 2.2. A detailed description of the modular ALS is given in [45]. To generate particle beams from different particle species, the geometry i. e. the diameters of the tubes and apertures are changed to create a flow field capable of focusing said particles. The geometry optimization procedure for focusing a specific sample is presented in chapter 4.

The working principle and underlying fluid and aerodynamics are described in various publications with a focus on generating particle beams [70–72]. The basic principles are summarized in the following.

Generating a nanoparticle beam using an aerodynamic lens stack is based on axisymmetric flow contraction of the particle trajectories in a carrier-gas flow field. The carrier-gas flow field is generated from the contraction of the flow in thin orifices [70]. In an optimal case, at each contraction, a so-called aerodynamic lens, the particles are moving closer to the center line. The parameter describing the optimal case of focusing nanoparticles is the Stokes number. In the following it is assumed that the gas flow is laminar, continuous and subsonic. The parameter describing whether a flow is laminar is the Reynolds number Re. It is defined via

$$Re = \frac{\rho_\mathrm{l} u L}{\mu_\mathrm{l}} \tag{2.1}$$

with ρ_l the liquid or in this case gas density, u the liquid or gas velocity, L a characteristic linear dimension and μ_l the liquid or gas viscosity. In our example of using an ALS with nitrogen as carrier gas and an upstream pressure of $0.2 \ldots 3.0$ mbar, $Re < 5$, which validates the laminar flow assumption. Typical gas speed inside the ALS tubes is not exceeding 20 m/s and only at the exit into low vacuum, the speed increases above the speed of sound in nitrogen, indicating the

break-down of Stokes flow. Inside the ALS, the assumption holds.

The Stokes number St is a dimensionless number that defines the ratio of the particle response time in a fluid flow and can be written as

$$St = \frac{2\rho_\mathrm{p} d_\mathrm{p}^2 C_\mathrm{c} \dot{m}}{9\pi\rho_\mathrm{l}\mu_\mathrm{l} d_\mathrm{f}^3} \tag{2.2}$$

in accordance with [72], where ρ_p the particle density, d_p the particle diameter, C_c the Cunningham slip correction factor (see below), $\dot{m}$ the mass flow, ρ_l the liquid or in this case gas density upstream and d_f the orifice diameter. The Cunningham slip correction factor C_c is given by

$$C_\mathrm{c} = 1 + Kn_\mathrm{p} \cdot \left(1.231 + 0.4695 \cdot \exp\left(\frac{-1.1783}{Kn_\mathrm{p}}\right)\right) \tag{2.3}$$

with Kn_p as the particle Knudsen number. The number factors of the correction factor on the Stokes number were found empirically [73]. Kn_p is a dimensionless parameter given by the ratio of the mean free path λ_l and the particle diameter: $Kn_\mathrm{p} = 2\lambda_\mathrm{l}/d_\mathrm{p}$. At a given pressure p and temperature T of the gas, the Knudsen number is given by

$$Kn_\mathrm{p} = \frac{k_B T}{\sqrt{2}\pi d_\mathrm{p}^2 p}. \tag{2.4}$$

In general, smaller and lighter particles have a smaller Stokes number, showing a faster response to the fluid flow and following fluid streamlines, whereas heavier and larger particles respond slower due to a higher inertia. Three limits of the Stokes number for particle focusing are defined: At $St \approx 1$, the particles are focusing efficiently onto the center line. For $St \gg 1$, particles detach from the flow field streamlines and cross the center line, leading to an over-focusing and therefore, defocusing of the particles. The third case with $St \ll 1$ describes the behavior for particles following the streamlines almost exactly, leading to a movement off-center after the ADL. All three cases are illustrated in Figure 2.2 b. When designing an ALS, Stokes numbers close to 1 are desirable. A lens calculator has been published in 2006, providing a powerful tool for designing an ALS [72]. However, to further understand the underlying processes and particle-beam formation inside the ALS, a numerical simulation environment has been developed to optimize these systems for the need of SPI experiments [46].

For the daily use of ALS injectors and the application in SPI, the important factors determining the ALS performance are particle transmission, particle-beam focus position z_0 and particle-beam focus size w_0. Therefore, it is necessary to simulate and measure the particle-beam properties from an ALS injector. Details on the actual particle trajectory calculations are given in Section 2.2 and the experimental characterization of the particle beam is presented in subsection 2.1.2.

Nanoparticle cooling

Despite a good particle beam with high particle number density, another important parameter for SPI experiments is the purity of the sample. Even with careful sample preparation, there may be different species present, such as conformers, clusters and charge states. Without additional effort for separating the impurities from the pure sample, these species reduce the resolution of the retrieved 3D structure if not taken care of in the data analysis [47]. To separate the wanted species from the unwanted ones, inspiration comes from small molecules. For example, to spatially separate the conformers of a molecule, an inhomogeneous electric field can be used. As a starting point a cold molecular beam is required. For small molecules, this is achieved via supersonic expansion from

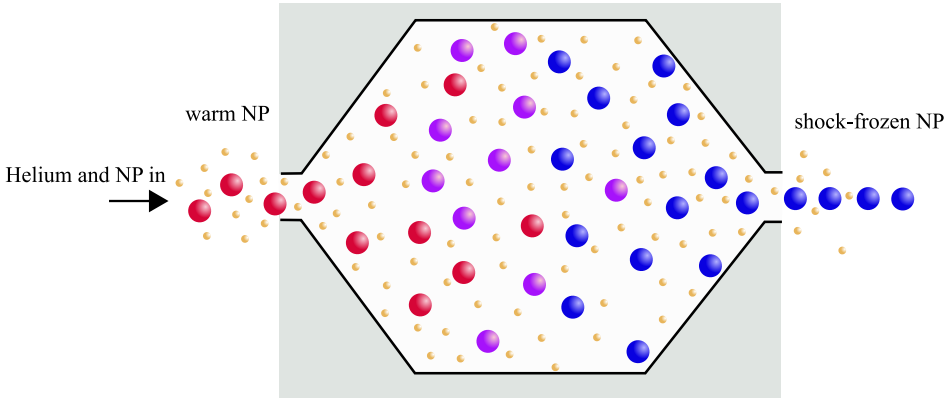

Figure 2.3: Illustration of the working principle of a cryogenic buffer-gas cell (BGC). Warm NPs ($T_0 = 297$ K) and cold ($T_{\mathrm{He}} = 4$ K) helium gas enter the BGC. During collisions, the NPs thermalize and are rapidly cooled. The shock-frozen NPs exit the BGC through an aperture into vacuum in a particle beam [54].

an Even-Lavie valve [74] and using an electrostatic deflector to generate pure molecular beams of specific rotational states or to separate cluster orders. For nanoparticles, using an Even-Lavie valve is not possible. Most biological larger molecules and particles denature and break upon heating. Instead of generating cold beams from supersonic expansion, shock-freezing larger NPs using a cryogenic buffer-gas cell (BGC) was demonstrated [54], based on ideas to use the BGC for atoms and small molecules [51]. The basic principle is shown in Figure 2.3. Warm nanoparticles (shown in red) at room temperature ($T_0 = 297$ K) enter a buffer-gas cell of a few centimeters dimension filled with cold ($T_{\mathrm{He}} = 4$ K) helium gas. During elastic collisions in the high gas number density, the NPs thermalize (shown in blue) and exit the BGC in a particle beam. Helium atoms are shown in beige color. Particle-beam formation is happening in a flow field generated from the exit aperture and a pressure difference inside and outside the BGC. The NPs are rapidly thermalized translationally and rotationally on a microsecond time scale, minimizing denaturation.

The cooling and particle-beam generation using a BGC was demonstrated for larger spherical NPs and virus capsids (> 200 nm diameter) [54]. Using Newtons law of cooling, the particle temperature and cooling rate could be calculated. At rather high helium flow in the BGC of 70 $\mathrm{ml_n/min}$, the cooling rate for sub 50 nm particles and proteins exceeded 10^6 K/s, higher than the cooling rate needed to form amorphous ice of 10^4 K/s and higher than the cooling rates reported for CEM [75, 76]. However, the drawback of particle-beam generation directly from a BGC is the particle-beam density, i. e., the particle-beam size. Improving the particle-beam generation for smaller NPs requires adding an ALS part to the BGC. This is presented in chapter 6.

2.1.2 Nanoparticle-beam characterization

The generated particle beam consisting of particles with diameters ranging from $25 \ldots 220$ nm is characterized in the laboratory using optical scattering, which is presented in the following section. Other techniques for nanoparticle-beam detection, especially of smaller NPs are, e. g., laser-induced breakdown detection (LIBD) [77] or via strong-field ionization [78].

Scattering theory

Optical scattering is well described using the Mie-scattering law to determine the particle brightness depending on the particle diameter [79]. As the particle diameter d_{p} is smaller than the wavelength λ of the used laser, the light scattering can be approximated using Rayleigh scattering. The

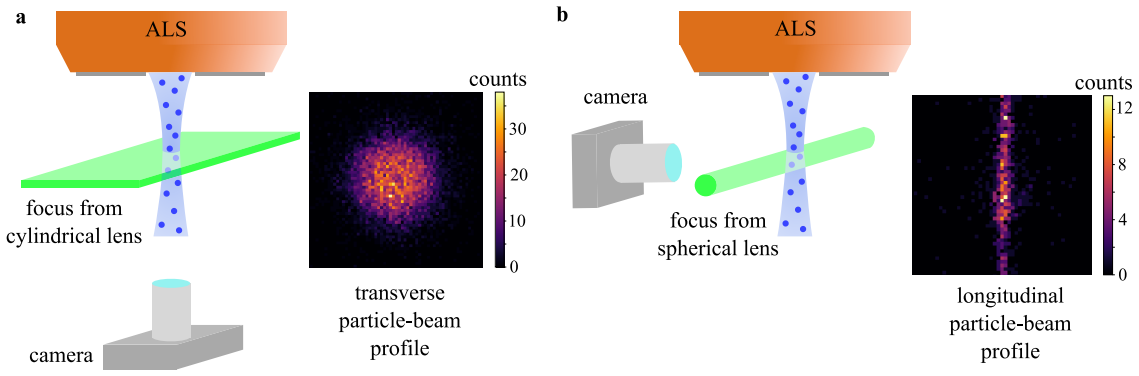

Figure 2.4: Different particle-beam characterization geometries. a.) Transverse particle-beam imaging, i. e., light-sheet imaging. The particles pass the focus of a cylindrical lens and the scattering is collected looking into the particle beam. The inset shows an example of a measured transverse particle-beam profile. b.) Longitudinal particle-beam imaging, i. e., side-view imaging. The particles pass a focus of a spherical lens and the scattering is collected perpendicular to the particle beam and the laser path. The inset shows an example of a measured longitudinal particle-beam profile.

Rayleigh scattering intensity I_{det} is proportional to the sixth power of the particle diameter,

$$I_{\mathrm{det}} \propto d_{\mathrm{p}}^{6} \tag{2.5}$$

i. e., a 50 nm particle scatters 64 times less than a 100 nm particle in the same laser pulse. The validation of this approximation was demonstrated for NPs in a particle beam generated from an ALS in a particle size range of 40 . . . 125 nm [80]. Smaller particle diameters could not be detected in the reported experiment, showing the importance of high laser intensities and a clean background.

Other important parameters for the scattering intensity are the material, i. e., the absorption properties of the material and the detection angle relative to the illumination of the NP.

Experimental geometries

In our laboratory two experimental geometries for optical scattering particle detection are used: transverse and longitudinal imaging. The imaging geometries are shown in Figure 2.4.

To image the transverse particle-beam profile a *light-sheet imaging* (LSI) technique is used [55]. Detailed information about this method is given in chapter 3 and this method is used for particle detection in chapter 6. In short, a continuous-wave (CW) green laser ($\lambda = 532$ nm) is focused using a cylindric lens, generating an elliptic focus, i. e., a light sheet, crossing the particle beam at a right angle. The scattering off the particles is recorded with a camera-based microscope system, as shown in Figure 2.4 a. A blob finding algorithm is used on the collected camera frames to retrieve the blob central position, as well as the intensity of the found blob [81]. A 2D histogram of the found particle positions yields the transverse particle-beam profile as shown in the inset. From the scattering intensity, the speed of the particle is determined: Slower particles are crossing the light sheet in a longer time period, i. e., more photons are hitting the particle that can be scattered. Faster particles are illuminated by less photons, i. e., the scattering intensity is lower. A particle-beam evolution can be recorded by moving the ALS up/down and record 2D histograms at varying distance from the ALS exit. This method can be used to detect transverse asymmetries in the particle-beam profile induced by, e. g., an asymmetric flow field [54]. Due to the CW illumination, the particle flux can be determined and data collection time is only lacking real time due to shutter and read-out speed of the used camera. A disadvantage of the CW illumination is the limitation to detect particles ≥ 70 nm diameter. For smaller NPs, a pulsed laser is used.

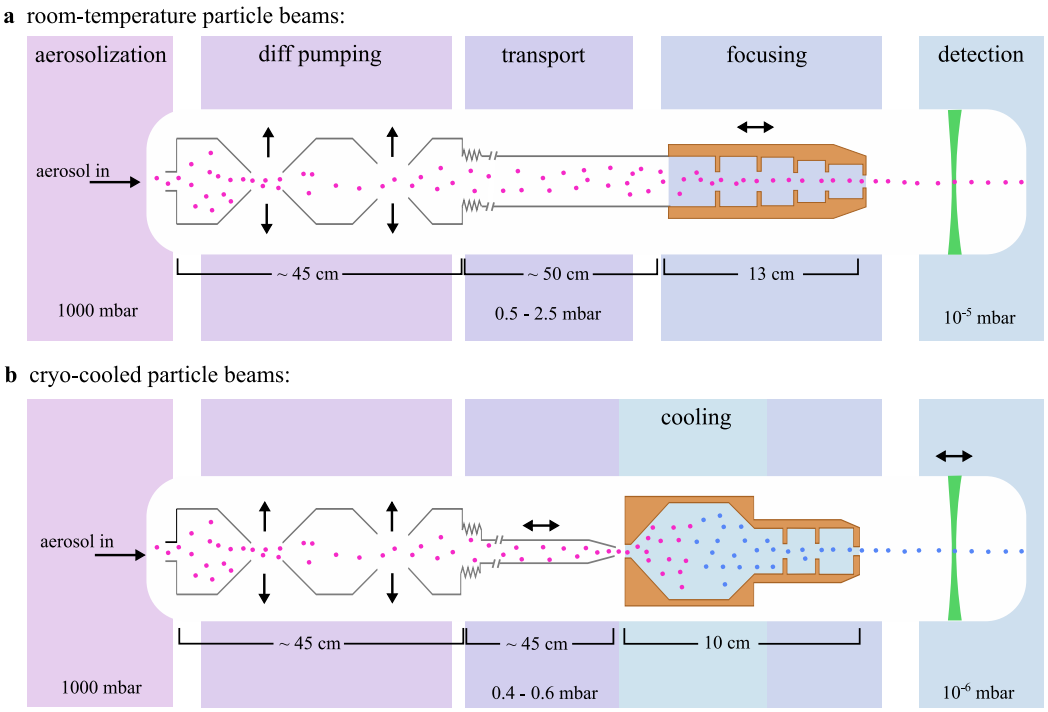

Figure 2.5: Schematic setups. a.) Room-temperature particle-beam setup. The aerosol enters a differential pumping stage and passing a transport tube into the ALS for generating a particle beam. The particle beam is detected via optical scattering. b.) Cryogenically-cooled particle-beam setup. The aerosol enters a differential pumping stage and passing a transport tube before being injected into the BGC filled with cold helium via a source tip. The BGC leads into an ALS to generate a focused particle beam. The particle beam is detected via optical scattering. See text for more details.

The second detection geometry is used to image the longitudinal particle-beam profile, we call this method *side-view imaging* (SVI). The setup is shown in Figure 2.4 b. Here, a pulsed laser source with central wavelength of $\lambda = 532$ nm, a pulse duration of 10 ns and a repetition rate of 20 Hz is used. The laser beam is focused using a spherical lens. The scattering off the particles is collected perpendicular to the laser and the particle beam. Within the 10 ns illumination, the particles are considered static. Their movement of less than 500 nm, assuming a particle speed of 50 m/s is smaller than the spatial resolution of the microscope camera. The image analysis is performed in the same way as for the light-sheet imaging and the 2D histogram of the found blobs is giving the longitudinal particle-beam profile and moving the ALS up/down yields the particle-beam evolution. Using a more powerful laser, we imaged PS NPs down to 25 nm diameter. This method is used in chapter 4 and chapter 5.

2.1.3 Experimental setup

Typical setups used in the presented work are sketched in Figure 2.5. Both setups for room-temperature particle beams and shock-frozen particle beams are presented.

The experiments were performed on different samples. A standard nanoparticle, commercially and in large quantities available, is a polystyrene sphere (PS). The diameter used ranges from $25 \ldots 220$ nm, and depending on the aerosolization method and particle size, different particle concentrations in solutions were used. For GDVN aerosolization and 220 nm PS, typical sample concentrations were $5 \cdot 10^6$ particles/ml and for 25 nm PS using ESI, sample concentrations of $2.7 \cdot 10^{13}$ particles/ml were used. In addition to PS, sucrose solutions with different concentrations

(2 . . . 10 %) were used for focusing experiments, but in general as alignment particles due to the high number of generated particles in the ESI process. With higher sucrose concentration, the generate sucrose balls are larger, same effect as for the flow rate: A higher flow rate results in a larger initial droplet size i. e., a larger sucrose ball. Furthermore, gold nanoparticles (AuNPs) were used with diameters of 27 nm.

The setup for room-temperature particle beams is shown in Figure 2.5 a. Either GDVN or ESI is used to generate aerosolized NPs and the aerosol is entering a differential pumping stage. In the differential pumping stage, the excess gas from the aerosolization process is removed by pumping in between the skimmers. The pressure is reduced from 1000 mbar at the aerosol inlet to around 11 . . . 25 mbar after the first skimmer stage to 0.5 . . . 2.5 mbar after the second skimmer stage, i. e., before the ALS. After the skimmer stages, the particles - together with a fraction of the gas - are following though a transport tube into the ALS. Transport of the particles is ensured due to pressure differences throughout the setup. After the long transport tube, the particles speed is assumed to be equal to the flow field speed. The upper part of the setup is mounted on an xyz-manipulator to move the particle beam with respect to the interaction region with the laser. Inside the ALS, the particles are following the flow field such that a particle beam is generated. The particles exit the ALS through an aperture into the main vacuum chamber, usually kept between $10^{-4} \ldots 10^{-6}$ mbar depending on the pressure before the ALS. In the laboratory, the particle beam is crossed by a focused laser and the scattering off the particles is detected using a camera-based microscope. For SPI experiments, the upper part of the chamber is mounted on the beamline setup and the particle beam is crossed by an x-ray beam.

The setup to generate particle beams of shock frozen nanoparticles is shown in Figure 2.5 b. The generated aerosol is entering a differential pumping stage, similar to the room-temperature setup. In contrast to the room-temperature setup, the transport tube is not connected to the BGC, but ends in a source tip in vacuum a few millimeters outside the BGC entrance. The source is generating a diverging particle beam that enters the BGC. The source is not cooled and mounted together with the upper part of the setup on an xyz-manipulator to align the source with the BGC entrance. The source pressure is held at 0.4 . . . 0.6 mbar. Inside the BGC, the particles thermalize with the cold helium gas ($T = 4$ K) and exit the ALS through an aperture into vacuum, typically $10^{-6} \ldots 10^{-5}$ mbar, depending on the amount of helium inside the BGC. The particle beam is detected via optical scattering using the LSI method using a camera-based microscope. In this setup, the particle beam source i. e., the BGC is fixed in position. To detect the particle beam at different distances from the BGC exit, the laser beam and the camera have to be moved.

2.2 Simulation methods

The last sections showed the experimental approach to determine the particle-beam diameter generated from an ALS using optical scattering. In addition to the experimental setup, a simulation framework saves significant time optimizing the set of parameters that influence the generated particle beam, such as the input pressure, the geometry of the ALS and the particle parameters like diameter and material itself.

This section describes the calculation of the carrier gas flow field inside an ALS at room temperature and inside the BGC-ALS at 4 K, and the calculation of the particle trajectories through these flow fields.

The carrier gas type depends on the aerosolization method and is typically helium or a mixture of nitrogen and CO_2. The mixture is consisting of mostly nitrogen (> 90 %) and therefore, the CO_2 is neglected in the carrier gas flow field calculations.

Due to the high number of gas molecules compared to the number of particles, only the interaction of gas and particle are modeled and the particle-particle interaction is neglected.

2.2.1 Flow-field calculations

To determine the fluid dynamic regime of the flow, the Knudsen number Kn, a dimensionless parameter, is calculated. Kn is described by the ratio of the mean free path of a carrier gas atom or molecule to a characteristic length. In an ALS for nitrogen at 1 mbar, the mean free path is around 69 µm and the characteristic length as an aperture is >1.5 mm. For the BGC at 1 mbar, the mean free path of helium at 4 K is around 2 µm and the characteristic length is roughly the same. With this, the Knudsen number is well below 1 ($Kn < 0.05$ and $Kn < 0.0015$) and the number of collisions are not treated individually, but the carrier gas is described in a continuum flow formulation using a set of partial differential equations: the Navier-Stokes equations.

The Navier-Stokes equations are based on conservation of mass and momentum and the solution is a vector field representing the flow velocity. From the flow velocity, other parameters of interest, such as the pressure are derived.

For calculating flows in 2D cylindrically symmetric geometries, such as the ALS, an available finite-element solver to solve the Navier-Stokes equations is used [82]. For more complicated and non-symmetric flows and geometries, such as the BGC-ALS, a more advanced finite-volume solver is used [83]. The laminar flow module can be used, as the Reynolds number, the ratio of inertial to viscous forces is typically low ($Re < 5$, see Section 2.1.1). For high Reynolds numbers, the flow is considered turbulent.

An example of the converged, steady-state flow field solved with the finite-element solver for the ALS at 1 mbar inlet pressure and nitrogen as carrier gas is shown in Figure 2.6 a. For visualization, the flow field is shown as a central cut through the ALS geometry. Inside the ALS, the gas speed is high at the apertures and inside the last ALS tube due to the reduced diameter. Outside the ALS, the gas is accelerated to high speed values (> 200 m/s). The gas speed is also visualized in Figure 2.6 b (purple line), which shows the gas speed at the center line, $r = 0$, throughout the ALS. At each aperture, a peak in the gas speed is observed. In addition, the pressure (orange line) is shown. At each aperture, the pressure is dropping and staying almost constant within one lens piece. In the last lens piece, the pressure is continuously decreasing and finally, a steep pressure drop is observed close to and outside the ALS ($z > 0$).

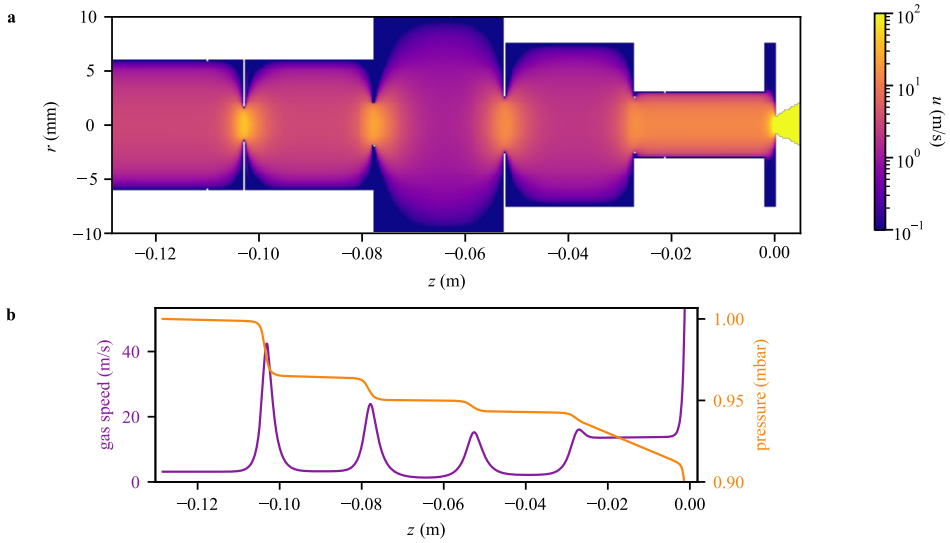

Figure 2.6: Simulated carrier gas flow fields for the ALS using COMSOL [82]. a.) Central slice of the nitrogen carrier gas flow field in the ALS geometry. The gas flow direction is from left to right. The inlet pressure is set to 1 mbar. b.) Nitrogen carrier gas speed in the center of the ALS ($r = 0$) throughout the ALS geometry (purple line). At each aperture, the gas speed in increasing and decreasing in the tube part of the flow field. Within the exit aperture and outside of the ALS, the gas is accelerated to speed values > 200 m/s. The pressure (orange line) inside the ALS is dropping at each aperture. Within the last ALS piece and outside the ALS exit, the pressure is dropping rapidly to values < 0.01 mbar.

2.2.2 Nanoparticle trajectory calculations

Drag force

After calculating the flow field, the particle trajectories are calculated. As discussed above, particle-particle interaction is neglected and only particle-gas interaction is taken into account. The force the particle is experiencing in the flow field is the drag force. For the case of particles inside an ALS, the drag force is reduced from the drag force in a continuous flow by the Cunningham correction factor C_c:

$$\vec{F}_{\text{drag}} = \frac{3\pi\mu_l d_p \Delta\vec{u}}{C_c}, \tag{2.6}$$

where μ_l is the dynamic viscosity of the fluid or the gas, d_p the diameter of the particle and $\Delta\vec{u}$ the velocity difference between the fluid and the particle. C_c is the Cunningham correction factor as described in Equation 2.3.

To calculate the drag force in 4 K helium flow fields, a different description of the drag force is used [84]. This model description is based on Epsteins description and promises a wide application to temperature ranges without the need for correction factors. From this method, the particle temperature can be extracted directly and is used for calculating the cooling rate of particles inside the BGC.

Brownian motion

In addition to the drag force, the particles experience an additional stochastic force: Brownian motion [85]. The force the particles experience is given by

$$F_B = m_p \vec{G} \sqrt{\frac{\pi S_0}{\Delta t}} \text{ with } S_0 = \frac{216\mu_l kT}{\pi^2 d_p^5 \rho_p^2 C_c} \tag{2.7}$$

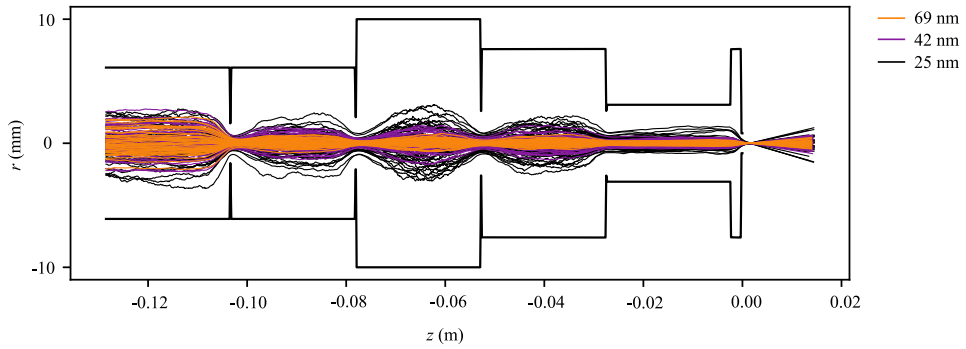

Figure 2.7: Calculated particle trajectories for 69 nm (orange), 42 nm (purple) and 25 nm (black) polystyrene spheres. For 25 nm, clear wiggles in the trajectories are visible, showing the effect of Brownian motion on small particles. For the calculations, CMInject [86] was used and the same carrier gas flow field and starting conditions for all particle sizes.

with m_p being the particle mass, $\vec{G}$ a vector of zero mean with unit variance, giving independent Gaussian random numbers, Δt the time step of the solver (typically 10^{-5} s), k the Boltzmann constant.

The force due to Brownian motion is temperature dependent. It is smaller at lower temperatures, reducing the random walk around the particle trajectories. The temperature dependence is one reason to move toward lower temperatures in particle focusing for small nanoparticles in the future. With decreasing particle diameter, Brownian motion is increasing, as shown from trajectory calculations in Figure 2.7. When decreasing the particle size from 69 nm (orange trajectories) to 25 nm (black trajectories) the wiggles in the particle trajectories are clearly visible, counteracting the focusing of the particles.

Throughout this thesis, already existing particle tracing codes are used. In chapter 4, the code from a previous publication was used [46], which later was developed into a python package called CMInject [86]. CMInject is used in chapter 5 and chapter 6. It is a computational framework that includes drag forces and Brownian motion to calculate the particle trajectories through a given gas flow field.

Nanoparticle-beam evolution

The simulated particle beam and its parameters such as the particle-beam focus position and width is the object of interest when simulating the particle trajectories through the flow fields. To include the gas flow field effect outside the geometry, i. e., after the exit, the flow field is extended a few millimeters outside and within the CMInject package, the detector feature is used to store and trace the particles position in r at each detector position z_D. The result at each detector is a histogram of the number of particles at the radial position r. The width of this distribution is determined via a Gaussian fit and taken as the full width at half maximum (FWHM). Placing the detectors at different distances yields a particle-beam evolution as shown in Figure 2.8 (shown as dots). To determine the particle-beam focus width and position, a Gaussian beam evolution curve fit is used (dashed lines). As the 1D particle-beam profiles were fitted using a Gaussian beam, this beam evolution function agrees nicely with the values. Similar fitting functions were used in an experimental publication [80].

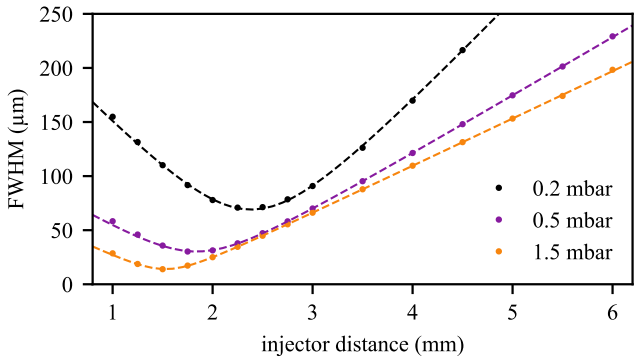

Figure 2.8: Simulated particle-beam evolution curves for spherical polystyrene particles with a diameter of 69 nm. The particle-beam width at different distances from the injector exit were simulated using CMInject [86]. Dots are the calculated values at each detector, the dashed lines correspond to a Gaussian beam evolution fit. For different injector pressures, the particle-beam properties, i. e., the focus position, width and divergence of the particle beam, change.

Chapter 3

Light-sheet imaging of nanoparticle beams[1]

Imaging biological molecules in the gas-phase requires novel sample delivery methods, which generally have to be characterized and optimized to produce high-density particle beams. A non-destructive characterization method of the transverse particle beam profile is presented. It enables the characterization of the particle beam in parallel to the collection of, for instance, x-ray-diffraction patterns. As a rather simple experimental method, it requires the generation of a small laser-light sheet using a cylindrical telescope and a microscope. The working principle of this technique was demonstrated for the characterization of the fluid-dynamic-focusing behavior of 220 nm polystyrene beads as prototypical nanoparticles. The particle flux was determined and the velocity distribution was calibrated using Mie-scattering calculations.

3.1 Introduction

Knowledge of the structure of biological molecules, such as proteins or viruses, is fundamental for understanding their function. A recently pioneered approach for directly recording high-resolution structures of intact single molecules is single-particle coherent diffractive imaging using x-ray free-electrons lasers (XFELs) [3, 7]. To reconstruct a three-dimensional molecular structure, this approach requires the collection of a large number of individual diffraction patterns from single molecules [28, 87]. In order to achieve this within the limited amount of time available at central XFEL facilities, therefore, requires a high particle flux in the gas-phase. Furthermore, as the samples investigated get smaller in size, now approaching the limit of single proteins, the necessary x-ray intensity for recording a single-shot diffraction pattern increases. Experimentally, this higher intensity is typically achieved by focusing the x-ray beam to a smaller spot, in SPI experiments typically to sizes of only ∼100 nm. This places stringent demands on the employed sample delivery methods, typically aerodynamic lens stacks (ALS) [42, 46, 70], and requires their characterization and optimization prior to XFEL experiments with laboratory-based methods.

Any characterization method for nanoparticle injectors would ideally reconstruct the full six-dimensional phase space of nanoparticles emitted, and would do so on-the-fly, *in situ*, non-destructive, and universally for any nanoparticle. Furthermore, the simultaneous characterization of sheath gas

[1]This chapter is based on the publication: L. Worbs, J. Lübke, N. Roth, A. K. Samanta, D. A. Horke, and J. Küpper, "Light-sheet imaging for the recording of transverse absolute density distributions of gas-phase particle-beams from nanoparticle injectors", *Opt. Express* **27**, 36580-36586 (2019) [55]. I contributed to the implementation of the optics setup, recorded the data, analyzed the data, prepared figures for the manuscript, wrote the first draft and updated the manuscript in discussion with all authors.

flows would be advantageous, but that seems to be well delegated to offline analysis [88]. None of the currently available nanoparticle-imaging methods fulfills all these requirements [59]. The most commonly employed method is optical imaging of the particle stream using side-illumination with a laser beam [59]. This allows one to measure the longitudinal position of nanoparticles, as well as their longitudinal velocity through the use of double-pulse lasers [80], commonly termed *particle imaging velocimetry*, or by recording light streaks from the particles through the use of appropriate illumination or exposure times [59]. While this side-view light-scattering approach fulfills the requirements for *in situ* operation and largely the universality for any nanoparticle, it does not detect asymmetries in the transverse nanoparticle-beam profile without scanning the laser focus through the particle beam. For larger particle beams this approach can, furthermore, suffer from a mismatch between particle-beam size and focal depth of the used imaging objective.

A direct way to record the transverse profile of particles has so far only been available through so-called dusting, where particles are caught on a sticky surface in-vacuum, which is subsequently imaged [59]. This approach has the obvious drawback of being destructive. Furthermore, it does not allow the recording of absolute particle densities, as the sticking probability of particles is not unity, nor of particle velocities.

Here, we present a different approach, combing the advantages of laser-based scattering microscopy with the ability to measured transverse particle positions: light-sheet imaging (LSI). A sheet of light is generated and the scattered light from the particles passing through the sheet is collected using a microscope. This method provides a simple, non-destructive, and *in situ* method to record transverse particle-beam profiles, including absolute number densities, as well as the velocity of particles passing through the light sheet. For best general applicability and overall characterization of the injection we employed a continuous detection scheme, which provides the maximal information on the sample beam and enables the characterization for any x-ray repetition rate. However, the method is general and could as well be utilized with a pulsed-laser illumination, e. g., a synchronized optical laser provided by the x-ray facility [89].

3.2 Experimental setup

A schematic overview of the LSI setup is shown in Figure 3.1. It mainly consisted of three parts: the optical setup for the generation of the light sheet from a continuous-wave laser, an ALS to generate a nanoparticle beam, and a microscope-detector setup for recording the scattered light.

The light sheet was generated from a continuous-wave laser system (Coherent Verdi V, 5 W, 532 nm), operated at 0.5 W and with vertical polarization. The initial beam diameter of 2.25(23) mm is increased by a factor of two using a Galilean telescope ($f_{L1} = -50$ mm, $f_{L2} = 100$ mm); throughout the manuscript all laser-beam widths are specified to the $1/e^2$ intensity. A second cylindrical-lens telescope ($f_{L3} = -50$ mm, $f_{L4} = 150$ mm) further increases the vertical diameter of the beam by a factor of three, yielding an elliptical beam with a vertical width of $h = 13.5$ mm and a horizontal width of $w = 4.1$ mm. This beam is focused using a cylindrical lens ($f_{L5} = 300$ mm), generating the light sheet in the center of the vacuum chamber. The created light sheet has a thickness of 24.8 µm (14.6 µm full-width-half-maximum, FWHM), a Rayleigh length of $z_R = 1.5$ mm, and a horizontal width of $w = 4.1$ mm. The corresponding maximum power density in the focus is $\sim 2.8 \times 10^3$ W/cm^2, well below the typical damage threshold for nanoparticles.

The nanoparticle beam was generated using a previously described ALS [46]. Briefly, 220 nm polystyrene beads in solution (Alfa Aesar, particle size 220 ± 17.3 nm) were diluted to 5×10^6 particles/ml and aerosolized using a gas-dynamic virtual nozzle (GDVN) [39, 90]. Following a differential pumping stage, nanoparticles entered the ALS, which produced a tightly collimated and focused particle stream in the vacuum chamber; the chamber pressure was typically held at

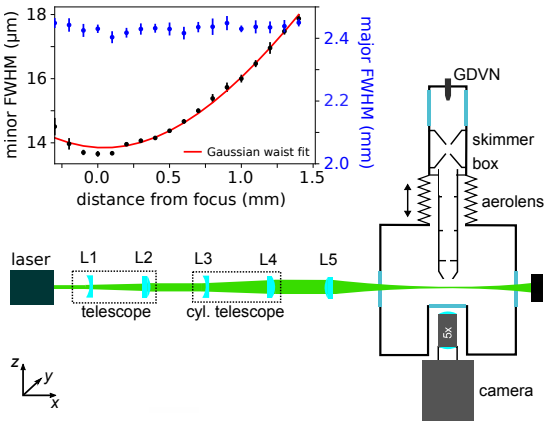

Figure 3.1: Schematic of the light-sheet imaging setup for the characterization of nanoparticle beams emerging from an aerodynamic lens stack. The light sheet is generated using a spherical telescope, a cylindrical-lens telescope, and a spherical focusing lens to create an elliptical focus. The inset shows the measured values of the minor, z, and major, y, widths along the light beam and the corresponding Gaussian beam-waist fit to determine the Rayleigh length $z_R = 1.5$ mm. Light is detected with a microscope and camera setup along the y direction.

6×10^{-5} mbar during experiments. The entire ALS system was placed on a motorized xyz-translation stage to allow accurate positioning of the particle stream.

Particles emerging from the the ALS passed through the light sheet and the scattered light was collected by a camera-based microscope system. This consisted of a long working-distance objective (Edmund Optics, 5× magnification, numerical aperture 0.14, working distance 34 mm) with a depth of view of 14 µm, chosen to match the sheet thickness to get sharp images of particle scatter, and a high-efficiency sCMOS camera (Photometrics Prime 95B, quantum efficiency 0.95 at 532 nm, 1200 × 1200 pixels). This yields a nominal resolution of 0.54 px/µm. Images were collected with a 1 ms exposure time and at a frame rate of 82 fps at full-frame size. Collected images were analyzed using a centroiding algorithm based on Hessian blob-finding [81], yielding sub-pixel particle positions as well as an accurate estimate of the number of recorded photons per particle.

The data shown were typically recorded for 2 000 frames and limited to a region of interest covering 350×350 pixels. Transverse beam profiles were generated as 2D histograms of the recorded particle positions. For the full three-dimensional reconstruction of the particle beam, the distance between the ALS exit and the light sheet was varied to build up a series of 2D transverse profiles. To recover the velocity of particles passing through the sheet, the recorded scattering intensity was compared with calculations based on Mie theory, performed using a homebuilt Python script based on the freely available Bohren and Huffman code [79], taking into account the experimental parameters, e. g., the scattering angle, the numerical aperture, and the particle size.

3.3 Results and discussion

An example image showing two nanoparticles passing through the light sheet simultaneously is shown in Figure 3.2 a. Here, the concentration of the nanoparticle solution was reduced from stock to ensure that camera frames contained no more than 2 particles. An example of a measured full particle-beam profile is shown in Figure 3.2 b, recorded 6 mm below the ALS injector. In Figure 3.2 c, the 3D beam profile is shown as individual 2D histograms recorded at several distances. These

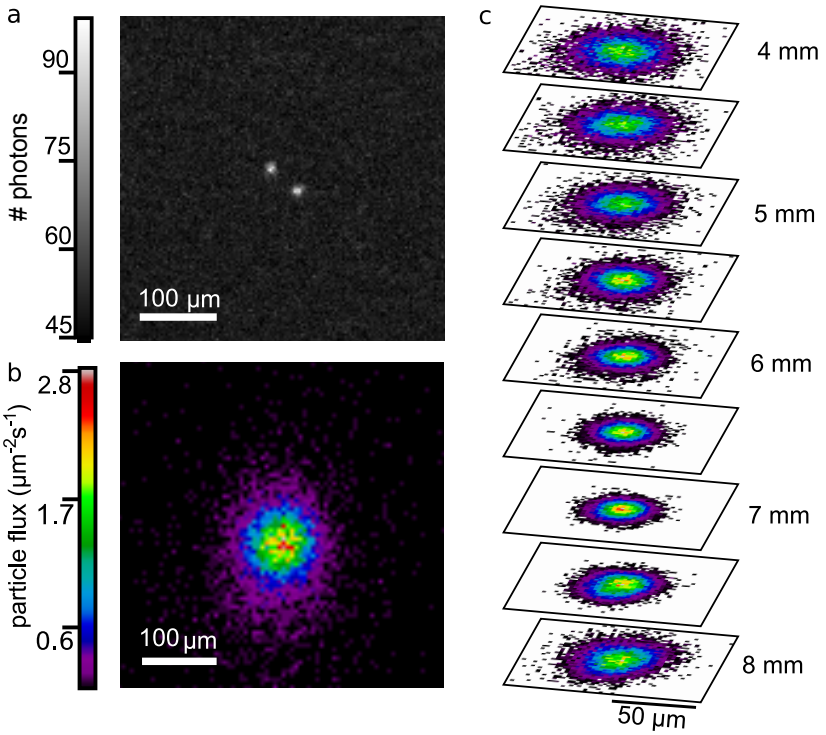

Figure 3.2: (a) Raw image of a single camera frame containing two particles. (b) Transverse beam profile 6 mm below the injector tip, shown as a 2D histogram of the determined particle positions; the colorscale represents particle flux. (c) 3D beam profile shown as individual 2D histograms measured at different distances from the ALS exit. The colorscale is the same as in (b).

measurements directly reveal, for instance, any astigmatism that might be present in the particle beam. From Figure 3.2 c it is clear that moving away from the injector tip the particle-beam widths changes, showing the characteristic focusing behavior of the injector [46]. Recorded particle-beam profiles typically show a Gaussian intensity distribution and the evolution of the particle beam can be accurately described by fitting a 2D Gaussian function to the recorded data, thus allowing for an easy evaluation of the beam widths and asymmetry through the minor and major axis of the fitted 2D Gaussian. The analysis of the size at 7 mm downstream the injector reveals that, without any specific optimization of the ALS, we generated a particle beam with a focus FWHM of 44.6(33) µm.

Since the measurement is based on counting individual particles, the histograms reveal the absolute particle flux, that is, the number of particles per area per second. The rate of particles is recovered from the observation time, which due to the continuous illumination is simply given by the number of frames multiplied by their exposure times. The particle flux can then be calculated from the number of particles detected per pixel or histogram bin. The peak particle flux per μm^2 per second as a function of the distance from the ALS exit is shown in Figure 3.3 a. Under the given conditions, the maximum particle flux of 4.3 particles/μm^2/s is measured 7.0 mm below the injector tip.

In order to recover the velocity of particles passing through the light sheet, the recorded intensity distribution from single particles was modeled by Mie theory. As the illumination region of the particles is constant, i. e., the thickness of the light sheet, the number of scattered photons depends on the time the particles need to pass the light sheet, i. e., their velocity. From this and the scattering probability as a function of particle size, from Mie theory, we can correlate the number of photons, i. e., the scattered light intensity, recorded per particle with its velocity. We assumed a particle size-distribution of 220 ± 17 nm as specified by the manufacturers. This results in a velocity

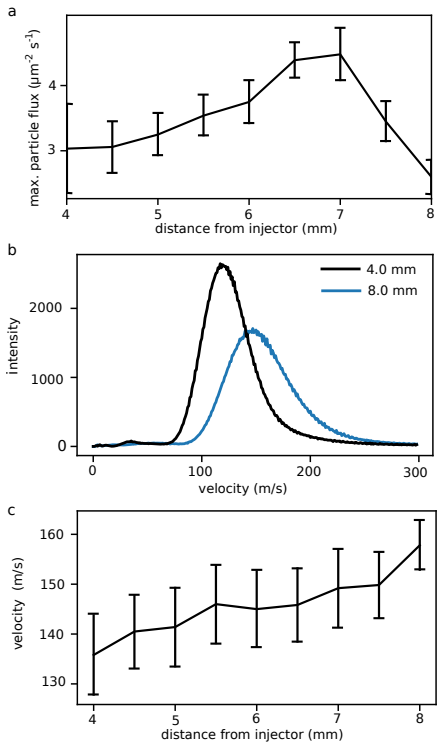

Figure 3.3: (a) Maximum particle flux as a function of the distance from the ALS, vertical bars represent the standard errors. (b) Velocity distributions measured at distances of 4 mm (black) and 8 mm (blue) from the ALS. (c) Mean of the velocity distribution depending on the distance from the injector.

probability distribution for every single measured particle. The velocity distribution of all particles measured at a certain distance from the ALS exit is the sum of the individual velocity probability distributions, see Figure 3.3 b. At 4 mm (black curve) downstream the ALS exit, the velocity distribution is centered around 122 m/s and the FWHM is 49 m/s. At 8 mm (blue curve) the mean velocity is 151 m/s with a FWHM of 66 m/s. Figure 3.3 c shows the mean velocity of the particle stream as a function of distance to the ALS exit. Both, mean velocity and the width of the velocity distribution increased with distance from the ALS exit, consistent with recent observations [80]. We ascribe the increasing velocity to acceleration by the helium gas co-emerging from the ALS, hinting at the need to correlate this acceleration with measurements of the gas density [88] in future work. The observed velocities above 100 m/s show that the particles are fast enough to clear the interaction region with an x-ray beam in a typical single-particle imaging experiment in between two pulses, assuming a µm beam size, including tails, and the 4.4 MHz repetition rate of the EuXFEL [91].

3.4 Conclusion

Light-sheet imaging (LSI) provides a non-destructive measurement technique for transverse nanoparticle-beam profiles. It is general and applicable to beams from any gas-phase nanoparticle-beam injector. Here, we characterized a nanoparticle beam generated from an aerodynamic lens stack. A light sheet with a thickness comparable to the depth of view of the used microscope objective was generated using cylindrical lenses. The scattered light from the nanoparticles was collected and utilized to determine the particle positions in order to measure the transverse beam profile and the absolute particle flux. The number of collected scattered photons was used for determining the velocity of

the nanoparticles.

In current single-particle diffractive-imaging experiments, the initial particle concentration in solution is in the order of 10^{14} particles/ml, which increases the maximum particle flux in our experiment to $\sim 10^7$ particles/µm^2/s, corresponding to $\sim 10^4$ particles/µm^2/frame at 1 ms exposure time. In this case, an *in situ* characterization would be enabled through limited effective illumination, e. g., using a pulsed illumination scheme.

Future single-particle diffractive-imaging experiments on biological molecules, with particle sizes of ∼10 nm, require the benchmarking of ALSs for such small particle sizes. The use of light-sheet imaging for such small particles requires increased laser powers. In our specific setup, e. g., with a 5 W green laser, the detection of particles is limited to particles down to ∼100 nm to be distinguishable from noise. The detection of smaller particles, e. g., 10 nm proteins with typical velocities from an ALS of ∼100 m/s, a cw laser power of 54 MW would be necessary, which is practically infeasible [92]. However, the sizes of these small particles sizes are typically more precisely known *a priori* and pulsed illumination, enabling such strong peak intensities, mimicking or even sub-sampling the XFEL temporal pulse profiles would provide equivalent information. This could still be feasible with standard laser technology routinely available at XFEL facilities.

Chapter 4

Geometry optimization of aerodynamic-lens stack injectors[1]

Single-particle x-ray diffractive imaging (SPI) of small (bio-)nanoparticles (NPs) requires optimized injectors to collect sufficient diffraction patterns to allow for the reconstruction of the NP structure with high resolution. Typically, aerodynamic-lens-stack injectors are used for NP injection. However, current injectors were developed for larger NPs (> 100 nm) and their ability to generate high-density NP beams suffers with decreasing NP size. Here, an aerodynamic-lens-stack injector with variable geometry and a geometry-optimization procedure are presented. The optimization for 50 nm gold-NP (AuNP) injection using a numerical simulation infrastructure capable of calculating the carrier gas flow and the particle trajectories through the injector is introduced. The simulations were experimentally validated using spherical AuNPs and sucrose NPs. In addition, the optimized injector was compared to the standard-installation "Uppsala-injector" for AuNPs and results for these heavy particles showed a shift in the particle-beam focus position rather than a change in beam size, which results in a lower gas background for the optimized injector. Optimized aerodynamic-lens stack injectors will allow to increase NP beam density, reduce the gas background, discover the limits of current injectors, and contribute to structure determination of small NPs using SPI.

4.1 Introduction

Simulations predicted the possibility of deriving high-resolution structures of biological macromolecules using x-ray free-electron lasers (XFELs) [7]. The ultra-short and extremely bright pulses of coherent x-rays provided by free-electron lasers (FELs) can outrun radiation damage processes before the particle has time to structurally respond and eventually be destroyed by the deposited energy [93]. Thus, the single-particle diffractive imaging (SPI) method at XFELs can be used to elucidate the structure of biological molecules [25, 26] without the need of highly ordered crystalline sample. SPI allows to retrieve the three-dimensional (3D) structure of biomolecules by reconstruction from a large number of two dimensional diffraction patterns, assembled into a 3D diffraction volume, requiring a high probability of an x-ray pulse interacting with an injected particle [28–30, 32]. High-density particle beams with ideally one particle per pulse and focus volume are generated to use both, x-rays and sample, efficiently. However, for the atomic resolution,

[1] This chapter is based on the publication: L. Worbs, N. Roth, J. Lübke, A. D. Estillore, L. X. Paulraj, A. K. Samanta, and J. Küpper, "Optimizing the geometry of aerodynamic-lens stack injectors for single-particle diffractive imaging", *J. Appl. Cryst.* **54**(6), 1730-1737 (2021) [56]. I contributed to the optimization procedure and ran the simulations based on an existing code. I contributed to the experimental implementation, recorded the data, analyzed the data, prepared figures for the manuscript, wrote the first draft and updated the manuscript in discussion with all authors.

$\sim$ 100 pm, reconstruction of a protein, 10^5 to 10^6 diffraction patterns need to be collected [27].

Delivery of high-density single-particle beams was demonstrated using aerodynamic-lens stacks (ALS) to generate focused beams of aerosolized particles from ambient conditions into vacuum [25, 70]. An ALS contains sets of thin apertures to manipulate the particles' lateral spatial distribution before it exits through the last aperture into vacuum. Aerodynamic lenses enable successive contractions of a flowing particle beam and provide focusing to high particle densities for wide range of particle sizes [87, 94]. Before adaption for SPI, they were mainly used in aerosol mass spectrometry to ensure a high transmission for a large particle size range [95]. A widely used injection system for SPI is the so-called "Uppsala injector", which usually contains an ALS (TSI AFL100), which can deliver collimated or focused beams for a range of particle sizes, e. g., 0.1–3 µm [42]. It was successfully used in various experiments at XFELs facilities and showed injection of 30 nm to 1 µm particles [31, 41, 42, 44, 61]. A recent experiment performed at EuXFEL showed the successful collection of more than 10 million diffraction patterns from single gold nanoparticles using this injector and shows the opportunities provided by careful sample preparation and injection [32].

However, currently sample injection and beam formation is the bottleneck of collecting large data sets of small bio-particle diffraction patterns and injection schemes have to be modified accordingly [34]. The geometry of the AFL100 is fixed, typically such that it can deliver particle-beams for a broad size range. The remaining parameter for tunability of the particle-beam's focus size during an experiment is the inlet pressure before the ALS [80]. To circumvent the increase of inlet pressure to generate a smaller particle-beam focus and thus an increase of pressure in the experimental chamber, we designed and used a new particle injector with variable geometry, as shown in Figure 4.1, i. e., the inner tube diameter and the aperture diameter can be changed [45, 46] to produce the highest particle-beam density for a given particle size. In addition, the speed of the particles is important in SPI experiments. It should be as slow as possible to increase the particle-beam density and thus hit rate, but with increasing repetition rates at XFEL facilities the particle speed has to be sufficiently fast to avoid interaction of NPs with two x-ray pulses. For the full repetition rate of 4.5 MHz at EuXFEL [17] and an x-ray focus size of 2 µm, the particle speed has to exceed 10 m/s to enter the interaction region without interacting with the previous pulse, which can damage or scatter off the sample already.

Here, we present the geometry optimization for aerosolized spherical gold nanoparticles (AuNPs) of 50 nm diameter at typical inlet conditions for SPI experiments, based on the generated particle-beam properties. The numerical simulation infrastructure used is presented elsewhere [46, 86]. To validate our simulation results, we compare them with experimental data for both AuNPs and sucrose spheres. AuNPs, when synthesized and prepared well, show a narrow size distribution similar to bio-particles and are therefore good benchmark samples for sizing and focusing experiments. AuNPs have a high scattering power that results in high detection efficiencies both in in-laboratory detection methods [55, 59] and in x-ray diffractive imaging, making it a useful sample for benchmarking data analysis and structure determination methods [32]. Furthermore, AuNPs exhibit distinct physical and chemical properties with potential applications ranging from quantum electronics to biomedicine and potential drug delivery systems [96, 97]. Sucrose particles are often used at XFEL facilities for alignment in commissioning and startup experiments [31, 61], as the number density of the generated sucrose spheres is high and the particle beam can be observed easily while aligning the injector to the x-ray beam. Most importantly, the mass density of sucrose NPs, and thus their focusing behavior, is comparable to biological matter, rendering them a good prototypical benchmark system for bio-nanoparticles.

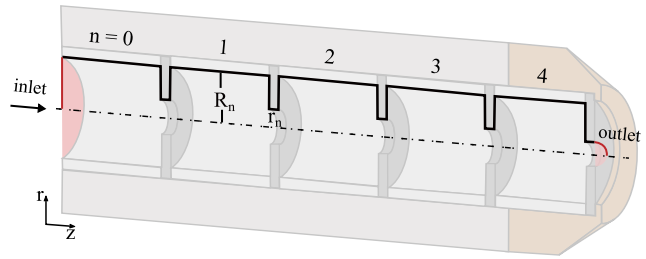

Figure 4.1: Schematic of the ALS geometry, which is cylindrically symmetric about the dashed line. Carrier gas flows from left to right. The black solid line is the 2D geometry used for the simulations, consisting of five aperture and tube pieces. The inner radius (R_n) of the tube as well as the lens aperture radius (r_n) can be changed individually [45]; see text for details.

4.2 Methods

4.2.1 Geometry optimization

Simulations of the ALS were performed as follows: First, we calculated the flow field of the carrier gas inside a given 2D cylindrically symmetric geometry using a finite-element solver for the Navier-Stokes equations [82]. The flow field was calculated within the ALS geometry and extended after the exit with a quarter-circle with the radius of the last aperture serving as gas-expansion region of the vacuum chamber as shown in Figure 4.1. The carrier gas was assumed to be nitrogen, as the particles were aerosolized using electrospray ionization (ESI), where the used gas mixture consists of $\approx$ 90 % nitrogen and $\approx$ 10 % CO_2. As boundary conditions for the flow field we used mass-flow conservation of 13 mg/min as inlet condition and a pressure of 10^{-4} mbar at the end of the flow field along the semi-circle. These values were experimentally used in a previous SPI experiment [45]. The limit of the mass-flow inlet is given by the pressure limits in the interaction chamber of SPI endstations, which typically require $p < 10^{-5} \ldots 10^{-4}$ mbar depending on the gas type. Additional flow field calculations were performed using the inlet pressure as a boundary condition. Second, the trajectories of 100,000 particles for a given flow field were calculated with a homebuilt Python particle-tracing code [46]; see also the meanwhile publicly available code [86]. This particle-tracing code assumes spherical particles. As most small bio-particles are non-spherical, future particle-tracing codes will have to take the particle shape into account [98]. Particles were introduced into the flow field with a uniform radial distribution covering the diameter of the first tube piece. We assumed the particles' velocity to be equal to the flow field values. We simulated trajectories of 50 nm diameter spherical particles with a density of 19.32 g/cm^3, corresponding to the bulk density of gold. Transmitted particles were propagated further with their terminal speeds at the border of the flow field. Then, we determined the width of the resulting particle beam depending on the distance from the ALS exit, i. e., the last aperture. Beam widths d_{70} were specified as the diameter where 70 % of the particles were in; d_{70} is a useful and robust metric as it is independent of the actual beam shape. Nevertheless, outside of the ALS all simulated particle beams showed a peak-like radial distribution with the maximum of the particle density in the center ($r = 0$ mm).

The ALS consists of $n = 5$ aperture/tube pieces stacked onto another, see Figure 4.1. The lens aperture radius r_n and the inner tube radius R_n can easily be adjusted. In our ALS, the aperture radius can be chosen from 0.75 mm to 5 mm in 0.25 mm steps. The lens apertures are interchangeable. The inner tube diameter could be chosen from parts with radius $2, 3, 4, 5, 6, 7.5, 8, 10$ mm, which were available in stock; in principle, any size would be possible. The inner diameter of the tubes is

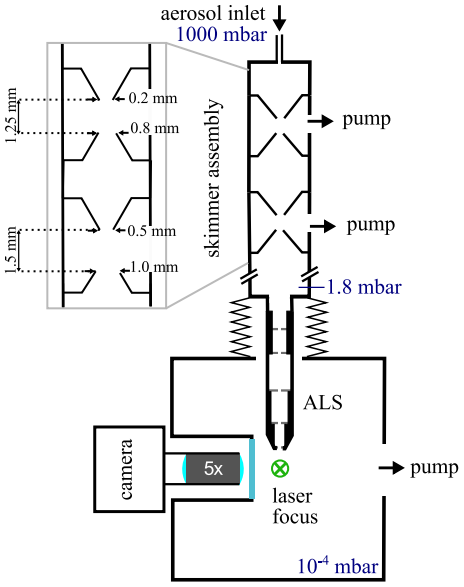

Figure 4.2: Schematic of the experimental setup for the characterization of nanoparticle beams. The aerosol passed a skimmer assembly to remove most of the carrier gas and the particles were focused using an ALS and entered the main vacuum chamber, where the particle beam was crossed by a laser beam. The light scattered off the particles was collected using a camera-based microscope system [55, 59].

adjusted by adding an additional tube into the standard 10 mm diameter pieces. The length of the tubes would be possible optimization parameter, which was fixed in the current study to avoid the added dimensions and complexity in the fit.

As the variety corresponds to more than 7×10^{10} combinations we approached the optimization as follows: Our optimization procedure was performed iteratively from the exit to the entrance of the ALS, as the last aperture radius (r_4) largely determines the focus position and size of the particle beam [99]. We started the optimization in the last piece of the ALS, r_4 and R_4. The particles were introduced into the flow field with a uniform radial distribution covering $r_{\text{initital}} = 0.02$ mm, mimicking that the lenses before already prefocused the particle beam. The initial particle velocity was set equal to the flow fields speed. The best r_4 and R_4 combination fulfills the following condition: The transmission was > 90 %, the focus was at $z > 4$ mm to suppress background scattering from the housing of the ALS, and it resulted in the smallest beam diameter. With this optimized r_4 and R_4 combination we then optimized r_3 and R_3 for the same requirements of the particle beam, and this was subsequently iterated for all lenses with increasing initial radial distribution of the particles, i. e., 0.02 mm for piece 4 and 3, 0.5 mm for piece 2, 1 mm for piece 1, and the whole radius of the lens filled before the first aperture. This optimization procedure reduces the efforts to 160 combinations per lens and < 1000 overall.

In addition, we performed simulations using the "lens calculator" [72] with similar input values for particle and flow specifications to compare the result to our optimized geometry. Details on these simulations are given in the supplementary information.

4.2.2 Experimental setup

We measured the particle-beam evolution of AuNPs from the optimized ALS geometry. The schematic of our experimental setup is shown in Figure 4.2. It consists of four main parts: an aerosolization chamber, a differentially pumped transport tube, the ALS system for particle-beam formation, and the detection region for visualization of the particle beam. To generate isolated test

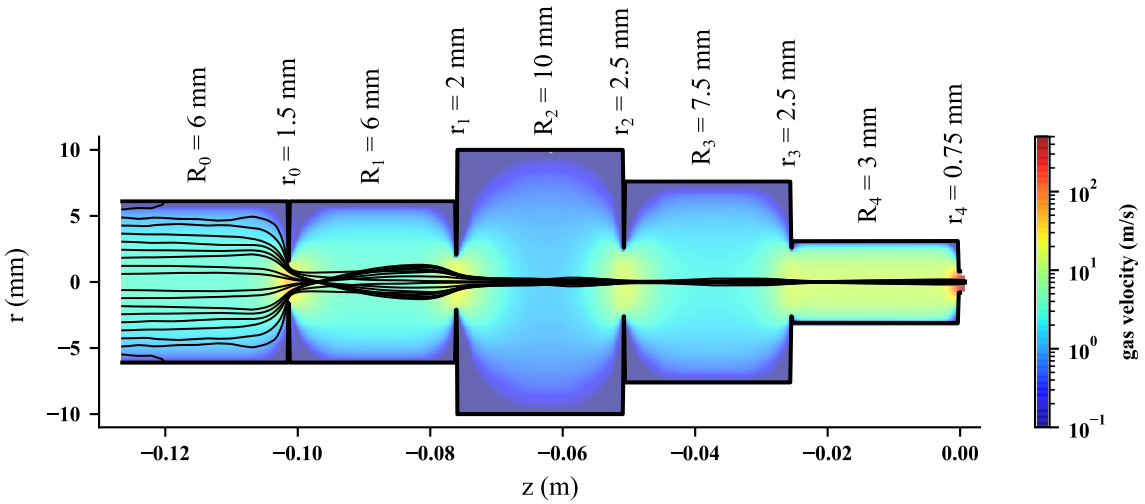

Figure 4.3: Optimized ALS geometry. Tube and aperture radii are specified above the device and the corresponding nitrogen-gas flow-field for the injection of 50 nm AuNPs at 13 mg/min mass flow is depicted in false color. Representative (calculated) particle trajectories are shown by black lines, with gas and particle flow direction from left to right. A clear focusing effect of the different parts of the ALS can be observed through the radial narrowing of the set of particle trajectories.

particles from the liquid sample, we injected spherical AuNPs with a diameter of (27 ± 2.25) nm in 5 mM ammonium acetate (AmAc) with a concentration of 10^{11} particles/ml and a 2 % sucrose solution in 20 mM AmAc using a commercial electrospray (TSI Advanced Electrospray 3482). The aerosolized nanoparticles passed through a differentially pumped skimmer assembly for pressure reduction. The particles were focused into the detection chamber using the ALS. The pressure above the entrance of the the ALS was 1.8 mbar (Pfeiffer Vacuum CMR 361). In the main chamber, the pressure was kept at 2.5×10^{-4} mbar. The ALS is mounted on a motorized xyz-manipulator to perform height scans and measure the particle-beam evolution.

Particles were detected using a side-view illumination scheme [59]. A Nd:YAG laser (Innolas SpitLight, 532 nm, pulse duration 11.5 ns, pulse energy up to 240 mJ at 532 nm, 20 Hz repetition rate) was focused into the center of the vacuum chamber intersecting the particle beam. The light scattered off the particles was collected using a camera-based microscope system [55, 59] consisting of a long working-distance objective (Edmund Optics, 5× magnification, numerical aperture $N_a = 0.14$, working distance $d = 34$ mm, depth of field 14 µm) and a high-efficiency sCMOS camera (Photometrics PrimeB95, quantum efficiency 0.95 at 532 nm, 1200×1200 pixels). This microscope yields a nominal resolution of 0.54 pixel/µm. Images were collected with a 1 ms exposure time synchronized to the laser at 20 Hz such that every frame covered one laser pulse. For every distance of the ALS and the laser, we recorded 10000 images for the AuNP sample and 2000 images for the sucrose sample. We determined the positions of the particles by analyzing the images using a centroiding algorithm based on Hessian blob-finding [81]. The particles' positions were converted into a 2D histogram, see supporting information for details. The width of the particle beam is determined from the projection of the particle beam onto the laser propagation axis. The beam diameter is shown as d_{70}.

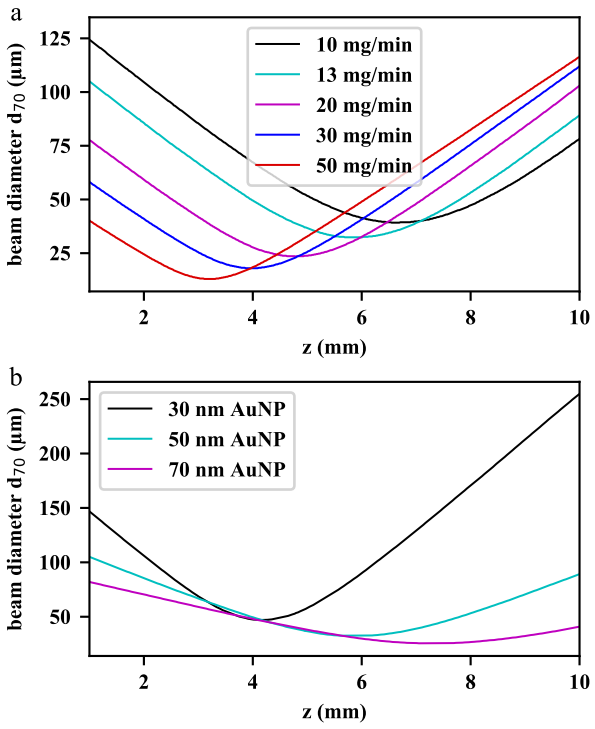

Figure 4.4: (a) Particle-beam evolution curves of the optimized injector for 50 nm AuNPs at different gas-mass flows. The width of the particle beam was determined as d_{70}. With increasing mass flow and thus pressure before the ALS, the particle-beam focus becomes harder, i. e., it moves closer to the ALS exit and gets smaller. (b) Particle-beam evolution curve of the optimized injector for different AuNP sizes at 13 mg/min mass flow. With increasing particle size, the particle-beam focus decreases and moves further away from the ALS. The convergence increases with decreasing particle size.

4.3 Results

4.3.1 Optimization and simulation results

The optimization process resulted in one final geometry which produced a particle beam to our specifications. The resulting optimized-lens-stack geometry is shown in Figure 4.3. From entrance to exit, the lens-tube and aperture radii are first increasing, then decreasing. The smallest lens tube radius and aperture radius are obtained for the last lens piece. Values are given next to the geometry. The velocity-flow field for 13 mg/min mass flow and particle trajectories for 50 nm AuNPs at different inlet positions (black solid lines) are shown in Figure 4.3, demonstrating a clear focusing effect of the ALS.

For this optimized injector we calculated the Stokes numbers for all the apertures and tubes and they are very close to the optimal Stokes number for the pressure range we are working in, see Supplementary information Table 2 for details.

For this ALS geometry, the 50 nm AuNP beam focused at a distance of 5.8 mm from the ALS exit with a particle-beam width of of 33 µm (d_{70}). The particle-beam evolution for 13 mg/min mass flow is shown in Figure 4.4 a as the cyan curve. The particle-beam evolution is shown as the beam width (d_{70}) depending on the distance z from the ALS exit. We simulated the focusing behavior for different mass flow conditions between 10 and 50 mg/min. With increasing mass flow, the focus shifted closer to the exit of the ALS and the focus size decreased. At 50 mg/min mass flow, the particle-beam focus size decreased to 13 µm at a distance of 3.2 mm. Similar behavior has been shown experimentally for the “Uppsala-injector” [80]. Therefore, working at higher mass flow is

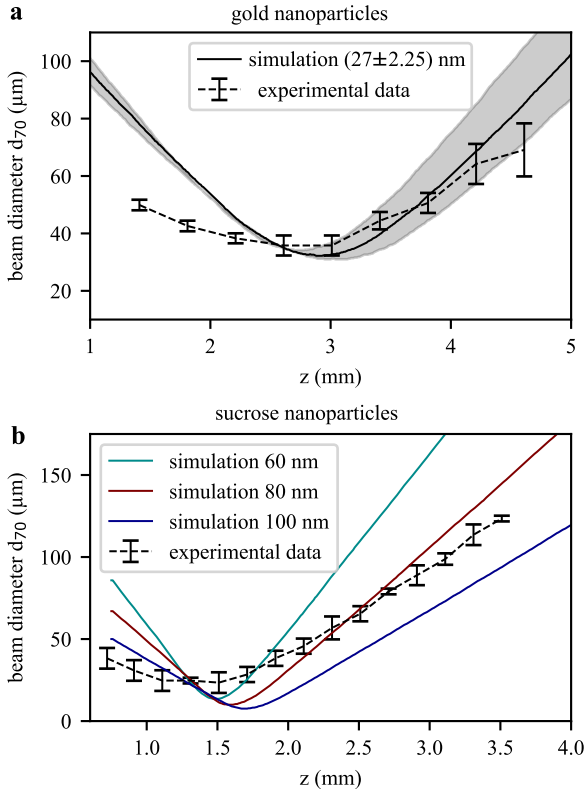

Figure 4.5: (a) Experimental particle-beam size evolution for (27±2.25) nm AuNPs (black dashed line). Simulated beam evolution is shown for 27 nm (black solid line) with the spread of the beam diameter due to the size distribution of ±2.25 nm (grey area). (b) Experimental particle-beam size evolution for sucrose spheres (black). The experimental data agrees reasonably well with a simulated particle size of 80 nm (dark red).

desired, but it will increase the amount of gas introduced into the interaction chamber and result in a higher pressure and thus a higher gas-scattering background in diffractive imaging experiments.

At 13 mg/min mass flow the AuNPs exiting from the optimized ALS had a mean velocity of 29 m/s. Mean velocities and beam diameter values for different flow conditions are given in the supporting information. The behavior of the ALS optimized for 50 nm AuNPs was compared to smaller and larger diameters of the AuNPs as shown in Figure 4.4 b. For smaller AuNPs the focus moved closer to the ALS and was larger, whereas bigger particles were focused further away and showed a smaller focus size. An interesting feature observed was the change of the convergence depending on the particle size: The smaller the particles were, the larger the convergence became. A precise positioning for small particles becomes necessary to meet the particle-beam focus. This change of the convergence is due to the larger momentum of larger particles interacting with the gas flow field.

The optimized geometry obtained using the "lens calculator" [72] is shown in Figure S3 in the supplementary information. All aperture and tube radii were larger than in our geometry and this ALS produced a particle-beam width of 817 µm at 5 mm, i.e., it resulted in a much larger particle beam with correspondingly strongly reduced density compared to our fully optimized geometry.

4.3.2 Experimental results

We measured particle-beam evolution curves of AuNPs and sucrose particles. The AuNP data with standard errors is shown in Figure 4.5 a as beam diameter (d_{70}) depending on the distance from the injector exit, along with simulations for the particle size of (27 ± 2.25) nm using the experimentally

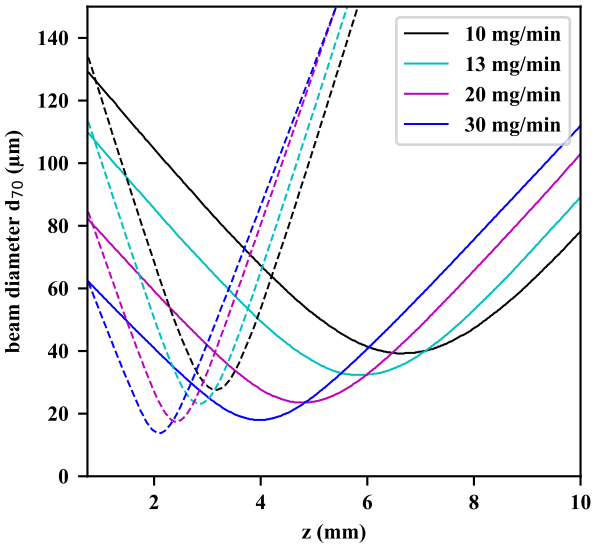

Figure 4.6: Simulated particle-beam evolution curves of 50 nm AuNPs exiting from the "Uppsala-injector" (dashed lines) for different mass flow conditions in comparison to the corresponding focusing curves from our optimized injector (solid lines).

measured inlet pressure of 1.8 mbar above the ALS. The experimental and simulated particle-beam diameters agree well, especially at and after the focus of the particle beam. Some deviations are observed before the focus, where the simulation overestimates the beam diameter, e. g., by a factor of ~ 1.5 at $z = 1.4$ mm. However, the most relevant parameters for SPI experiments, the focus position and focus size, are in excellent agreement between experiment and simulation. The same experiment is repeated for a 2 % sucrose solution to generate spherical sucrose particles in the electrospray process with a broad size distribution around 80 nm, shown in the supporting information. The sucrose-particle-beam evolution is shown in Figure 4.5 b with standard errors (black) and compared to simulations for different sizes of sucrose spheres ($\rho = 1.59$ g/cm^3). Overall, the experimental data is described well by the simulation for 80 nm sucrose spheres. Similar to the AuNP data, the simulation agrees well with our data after the focus, although before the focus the simulation deviates by a factor of ~ 1.6 at $z = 0.8$ mm. This mismatch is partly due to the broad experimental size distribution, i. e., the experimental data does not correspond to a single particle-size simulation.

4.3.3 "Uppsala-injector" simulation

The "Uppsala-injector" (AFL100) was introduced before and used in various experiments at XFELs [31, 41, 42, 61]. We simulated its focusing of 50 nm AuNPs and compared it to our optimized ALS.

The beam evolution curves for 50 nm AuNPs at different mass flow conditions for this injector are shown in Figure 4.6 (dashed lines), along with the focusing curves for our optimized injector (solid lines). The simulated transmission of 50 nm AuNPs through both injectors was above 90 %, i. e., at 13 mg/min mass flow the transmission was 91.9 % for the AFL100 and 93.4 % for our optimized injector. At the same mass flow the AFL100 showed slightly smaller mean velocities of the exiting particles than our optimized injector. As an example, at 13 mg/min mass flow, 50 nm AuNPs exiting the "Uppsala-injector" showed a mean velocity of 27 m/s. In comparison, particles in our injector reached a velocity of 29 m/s. A detailed list of velocities depending on mass flow is shown in the supporting information.

4.4 Discussion

Our simulations show that the focus size is comparable for both injectors, but the difference is in the focus position and the convergence. Our injector focuses the particles further downstream and the focusing is not as hard as for the AFL100. Generating a focused particle beam further away from the injector exit has the advantage of a lower background from the nitrogen and CO_2 gas. Light gas diverges fast from the exit of the ALS into the vacuum chamber.

The focus position of the AFL100 is closer to the injector exit and can cause problems when using smaller particles and particles with smaller density, such as bio-particles: The smaller and lighter the particles the closer the focus position. As an example, simulations for 10 nm AuNPs at 13 mg/min nitrogen mass flow for the AFL100 showed that the focus position moves very close to the ALS exit, below $z = 1.5$ mm, and the transmission is reduced to 59 %. Our 50 nm-optimized injector still shows a transmission of 79 % for those particles and a focus position $> z = 2$ mm, see the supporting information for details. The same behavior holds for the particle density: The lower the particle density (biomolecules), the closer the particle-beam focus becomes. For isolated proteins, it is almost impossible to focus the particle beam with these injectors. In this case, an appropriate geometry optimization could result in a geometry that focused the particle beam further away from the injector exit. In addition, the particle transmission for a 10 nm bio-particle would decrease due to lower density compared to the density of AuNP, which is around 20 times larger. Lower particle density increases Brownian motion for the same size and therefore, decreases particle transmission though the ALS for bio-particles. This could be mitigated by lowering the temperature [54], if compatible with the envisioned study.

4.5 Conclusion

We presented an optimization procedure of an ALS for 50 nm AuNPs using our previously developed computer-simulation framework for ALS injectors [46, 86] including the results of this optimization. We experimentally benchmarked the optimized geometry for beams of spherical gold and sucrose nanoparticles. Both particle-beam-evolution curves are in good agreement with the simulations. This validates our simulation framework, which can be used to get further insight into the fluid-dynamics focusing process and to develop optimized particle injectors for different sizes and materials, as well as for different experimental conditions, such as inlet pressure and gas type.

We compared our optimized injector to the widely used AFL100 “Uppsala-injector” for 50 nm AuNPs. Both injectors create a focused particle beam for different inlet mass flow conditions, and the main difference is observed in the particle-beam focus position, which for our optimized injector is further downstream, which reduces the carrier gas background at the focus and will be greatly beneficial for x-ray diffractive imaging, especially of small bio-particles that exhibit only small scattering signals.

Our variable injector geometry allows us to vary the particle-beam focus independent from the inlet pressure by varying the geometry and thus keeping the pressure after the injector, i. e., in the x-ray interaction region, constant. Generating high-quality particle beams of nanoparticles does not only allow for structure determination by an increased number of collected diffraction patterns, but in addition it open the field of time-resolved imaging of nanoparticle dynamics in future pump-probe-type experiments at XFELs.

Chapter 5

Small nanoparticle beams from aerodynamic lens stacks[1]

High-resolution imaging of isolated nanoparticles and proteins can be achieved using ultra-bright femtosecond x-ray pulses generated from x-ray free-electron lasers. Current bottleneck in imaging proteins and small nanoparticles is sample injection. To deliver focused or collimated nanoparticle beams for single-particle diffractive imaging, aerodynamic lens stack injectors are used. However, extending the use of aerodynamic lens stack injectors to particle sizes below 40 nm has been limited by in-lab particle-beam detection methods and also by the limited understanding of the particle-beam formation for small nanoparticles. We present experimental and simulated particle-beam profiles for polystyrene spheres down to 25 nm diameter. We observe an unexpected focus-shift away from the injector exit with increasing pressure. Using simulated phase-space distributions, we explain the opposing focus shift for large (>40 nm) and small (<40 nm) nanoparticles. Furthermore, we extend our simulations to 10 nm protein-like nanoparticles, showing the particle-beam evolution curves with increasing injector pressure. Our results highlight the use of extended flow-fields outside the aerodynamic lens stack in the simulations and improves understanding of the particle-beam formation from aerodynamic lens stack injectors.

5.1 Introduction

Studying the structure and dynamics of isolated (bio-) nanoparticles without the need for crystallization opens the door to a wide range of structural imaging. Imaging of isolated particles with x-ray radiation is referred to as single-particle x-ray diffractive imaging (SPI). Aerodynamic lens stack (ALS) injectors are used at x-ray free-electron-laser (XFEL) facilities to provide focused or collimated nanoparticle beams for SPI experiments [28, 32, 41, 42]. ALS injectors consist of a set of orifices that manipulate the aerosol particle trajectories, resulting in a particle-beam formation [71, 87, 94]. With the computational prediction of diffraction-before-destruction, the concept of SPI experiments and structure determination of isolated (biological) particles, such as proteins, and studying their dynamics upon excitation became reality [7, 25, 26]. Recent SPI experiments included imaging of gold nanostructures [32], sucrose nanoparticles [31], Mimivirus [28], Melbourne virus [29] or Coliphage PR772 virus [30].

On the way toward the imaging of smaller nanoparticles, sample injection and particle-beam formation for small (<40 nm) particles is a major bottleneck [34].

[1] This chapter will be submitted to *J. Phys. Chem. C* for publication [57]. I performed the simulations and analyzed the simulated data. I recorded the data, analyzed the data and prepared the figures for the manuscript. I wrote the first draft and updated the manuscript in discussion with all authors.

ALS injectors were successfully used for even larger (>100 nm) nanoparticles and recent studies showed a decrease in performance, i. e., transmission and particle-beam focus size and position with decreasing particle size [34, 56, 80]. Continuous effort was made for improvements on the injection system, e. g. by changing the aerosolization method [61], setting up simulations for the particle-trajectories through the ALS system [46, 86], developing a fast-exchange ALS injector [45], optimizing the ALS geometry for specific particle species [56], and laboratory-based characterization methods for the particle-beams, determining the longitudinal or transverse particle-beam profile, determine the particles' speed and gas background [55, 80, 88]. Laboratory-based characterization of small nanoparticle beams using optical scattering is mainly limited by low optical detection signal. The number of scattered photons depends linearly on the number of incoming photons, but inversely to the power of six on the particle diameter [79]. Therefore, high-power lasers and a clean background are needed for optical-light-scattering detection of such small nanoparticles.

Past experimental studies on 70–200 nm diameter polystyrene (PS) spheres showed both, a movement of the particle-beam focus toward the injector exit and a decrease in focus size, with increasing injector pressure [80]. Similar behavior was observed in simulations on gold nanoparticles [56]. The same studies showed a movement of the particle-beam focus toward the injector exit and an increasing particle-beam focus size with decreasing particle diameter. Extrapolating the behavior toward single proteins (d<10 nm) or even larger protein complexes (d<30 nm) painted a dark picture on the future of SPI using ALS injectors. These predictions suggested that any reasonable-size focus of such particle beams would move too close to the ALS injector tip, strongly increasing the likelihood of unwanted background scattering on the already increasingly weaker signals.

Here, we present experimental results and simulations on particle beams from polystyrene spheres down to 25 nm diameter. We disentangled the dependence of the particle-beam width evolution on the injector pressure for 69, 42 and 25 nm PS spheres. In contrast to the larger PS spheres, we observed a shift of the particle-beam focus position away from the injector exit with increasing pressure for 25 nm. Simulations supported these measurements and we could explain the effect through phase-space distributions and the extension of the carrier-gas flow field outside the injector exit in the simulations. Additionally, we present particle-beam simulations for 10 nm protein-like nanoparticles and the injector pressure dependence. We observed the same shift of the particle-beam focus position away from the ALS exit with increasing inlet pressure. Our findings clearly show the applicability of ALS injectors even for small single nanoparticles with optimized injector pressure conditions for SPI experiments and improve the understanding of the particle-beam formation from ALS injectors.

5.2 Methods

5.2.1 Experimental setup and data evaluation

The particle-beam evolution, i. e., the beam diameter depending on the distance from the ALS injector, of aerosolized nanoparticles were measured using a setup described elsewhere [56]. PS were aerosolized from solution using an electrospray (TSI 3482). Excess nitrogen and CO_2 gas were removed using a double-skimmer assembly and particles were focused using an ALS [45]. Gas pressures in the injector were PS size dependent and in the range of 0.2. . . 2.4 mbar. Individual nanoparticles were imaged using a camera-based microscope to record a longitudinal particle-beam profile at different distances from the ALS exit. Improvements on the setup included a post-sample aperture to reduce stray light from the metallic parts, e. g. the ALS, inside the vacuum chamber, adjustable pumping in both skimmer stages to control the injector pressure and a modified injector

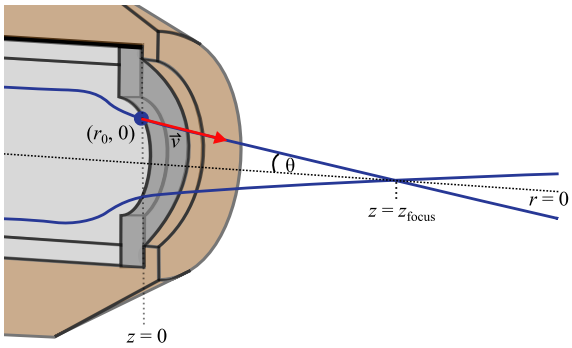

Figure 5.1: Determining the particle-beam focus position, z_{focus}, depending on the particle coordinates at the ALS exit ($z = 0$). Assuming no particle-field interaction, the focus position is only depending on the angle of the velocity vector at $z = 0$.

exit, which allowed for measurements of the particle-beam width at 1 mm injector distance. All modifications are described in detail in the supplementary material, see Figure S1. Three different PS samples with sizes of (25±4) nm (Thermo-Fischer), (42±0.5) nm (Polysciences) and (69±10) nm (Polysciences) with a number concentration of $2.7 \cdot 10^{13}$ particles/ml (25 nm), $1.5 \cdot 10^{12}$ particles/ml (42 nm) and $2.9 \cdot 10^{11}$ particles/ml (69 nm). Liquid flow rates were 400 nl/min, 400 nl/min and 650 nl/min, respectively. We collected a total number of 30,000 (25) and 15,000 (42 and 69 nm) camera frames per distance from the injector.

From the camera frames the particle positions were obtained in the plane determined by the particle beam direction z and the laser beam direction x. The resulting two-dimensional (2D) histogram of particle positions was projected onto the laser propagation axis and fitted by a Gaussian distribution function. All measured 1D particle beam distributions had Gaussian-like shapes, see supplementary material, Figure S2. From the fit the width of the particle beam was determined as full-width at half-maximum (FWHM) depending on the distance from the injector. The focus position of the particle beam was taken from a Gaussian beam propagation function $w(z)$ fit to the experimental data FWHM(z). $w(z)$ is defined as

$$w(z) = w_0 \sqrt{1 + \left(\frac{z - z_0}{z_R} \right)^2} \tag{5.1}$$

with the FWHM of the particle beam w, the beam waist w_0, the distance from the injector z, the focus position z_0, and the Rayleigh length z_R. A Gaussian beam propagation function has shown good agreement with the particle-beam evolution [80].

5.2.2 Simulations and simulated data evaluation

Particle-beam simulations were performed using the software package CMInject [86]. For every pressure and size, 10^4 particles were simulated with an initial velocity of $\vec{v}_{\text{init}} = (0, 10)$ m/s and an initial Gaussian transverse position distribution centered around $r = 0$ with a FWHM of 2.355 mm. For simulations of polystyrene spheres the particle density was set to 1050 kg/m^3 and the particle diameters were set to 25, 42 and 69 nm. For simulations of protein-like particles, the particle density was set to 1400 kg/m^3 and the particle diameter was set to 10 nm, corresponding to larger proteins. In all calculations, Brownian motion was included. The CMInject detector feature, with detectors placed at various different distances from the injector exit, was used for evaluation of the particle-trajectory data. The 2D cylindrically symmetric flow field of the nitrogen gas was calculated using a finite-element solver for the Navier-Stokes equations [82]. Aperture and tube diameters were the same as in earlier work [56], but included the modified tip in the flow field

geometry, see section 1 in the supplementary material. The flow field was extended after the last aperture with a 5 mm long and 2 mm wide cone at the end of the flow field. Pressure was used as inlet condition and flow fields were calculated for inlet pressures from 0.2 . . . 2.5 mbar in 0.1 mbar steps.

The results of the simulations at different detectors were a set of coordinates (r, z, v_r, v_z) at different z-distances for each individual particle, with their radial position r, longitudinal position z, with $z > 0$ outside the ALS and $z < 0$ inside the ALS, the radial velocity v_r and the axial velocity v_z.

To determine the focus position of the simulated particle beam two different approaches were used: Method 1 used the particle coordinates at the ALS exit ($z = 0$): $r(z = 0) = r_0, z = 0, v_r, v_z$. In a non-interacting approximation, the particles will propagate outside the ALS with unchanged v_r and v_z. The particle position was calculated according to Figure 5.1. If one particle is considered, the focus position is equal to the z position the particle crosses the center line, which is determined by the angle of $\vec{v}$ with the center line. The focus position can be expressed as

$$z_{\text{focus}} = \frac{r_0 \cdot v_z}{v_r}. \tag{5.2}$$

For multiple particles, the distribution for z_{focus} showed a Gaussian distribution and the focus position was determined as the center of the Gaussian fit.

Method 2 included all detectors placed in the extended flow field after the ALS exit and up to 10 mm outside the ALS, thus encluding particle-gas interaction. At each detector, the particle-beam width as FWHM of the the Gaussian beam profile was determined. A Gaussian beam evolution function to the simulated data FWHM(z) was fitted similar to the experimental data evaluation. The focus position is z_0 of the Gaussian beam propagation function fit.

5.3 Results

5.3.1 Experimental results

Particle-beam evolution curves for three PS sizes at different injector pressures were measured. On average, the particle hit rates were 0.12 . . . 0.49 particles/frame for 69 nm, 0.07 . . . 0.17 particles/frame for 42 nm and 0.021 . . . 0.024 particles/frame for the 25 nm PS sample, depending on beam diameter and injector pressure. For 69 and 42 nm the detection rates were higher at lower injector pressure, whereas higher detection rates for the smaller 25 nm sample were observed at higher injector pressure. The 1D particle-beam profiles showed a Gaussian distribution, see supplementary material, Figure S2. fThe particle-beam evolution curves, i. e., the FWHM of the Gaussian distribution determined by a Gaussian fit depending on the distance from the injector for all three particle sizes at high (red) and low (black) injector pressures are shown in Figure 5.2. The error estimates shown on the experimental data correspond to one standard deviation (1σ) and the dashed line is a fit using a Gaussian beam propagation function, (5.1). Figure 5.2 a shows the results for 69 nm. At low injector pressure (0.2 mbar), the particle-beam focus was determined at $z_0 = 3.0$ mm with a FWHM of $w_0 = 68$ µm. At 1.8 mbar injector pressure, the focus position moved closer to the injector exit, $z_0 = 1.44$ mm and the focus width decreased to $w_0 = 15$ µm. Similar behavior was observed for 42 nm PS particles as shown in Figure 5.2 b: Increasing the injector pressure resulted in a smaller particle-beam width and a shift of the particle-beam focus toward the injector exit.

Figure 5.2 c shows the results for the particle-beam width when injecting 25 nm PS particles. Here, we observed a quite different behavior. At low pressure (0.55 mbar), the particle-beam focus

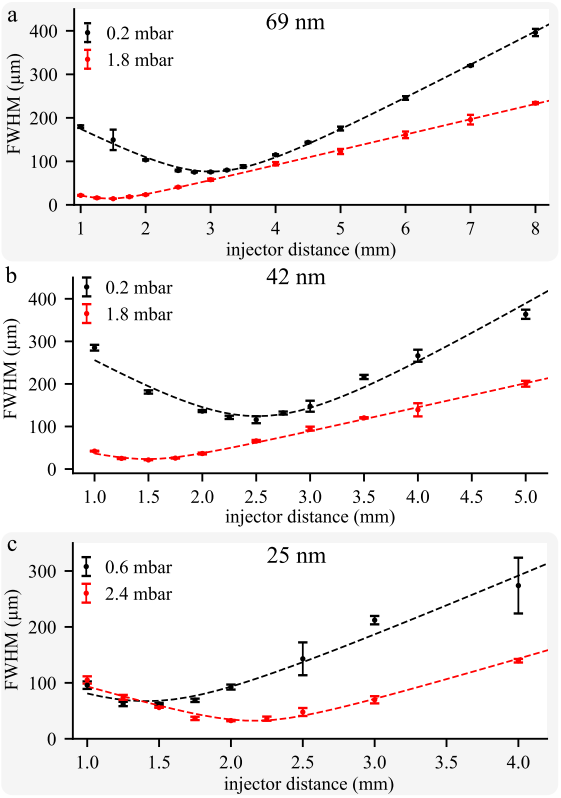

Figure 5.2: Measured particle-beam evolution curves for (a) 69 nm, (b) 42 nm and (c) 25 nm PS spheres for low (black) and high (red) injector pressures. Experimental values are given with standard deviation. Dashed lines correspond to a Gaussian beam evolution fit.

was observed at $z_0 = 1.41$ mm with a width of $w_0 = 67$ µm and at high injector pressure (2.4 mbar) the focus size decreased to $w_0 = 32$ µm at a distance of $z_0 = 2.16$ mm. The particle-beam focus moved further away from the injector exit with increasing pressure.

For all particle sizes the particle-beam width decreased with increasing injector pressure. Additionally, we measured the particle-beam evolution for intermediate injector pressures and determined the focus position and focus width. All beam evolutions are shown in the supplementary material, Figure S3 and the values are shown in Table 5.1. For comparison, we added the simulated values for the focus sizes and widths. The values for the focus widths for 69 and 42 nm PS particles agree nicely. For higher pressures we measured smaller particle-beam widths for 25 nm than simulated. At 2.4 mbar injector pressure we measured 32(4) µm and simulated 54(1) µm. However, the same trends are observed both in the experiment and the simulations: from 1.5 mbar to higher pressure values, the focus width stayed constant. The measured focus position deviates from the simulated values, but we observed the same trend: The simulations showed a shift of the focus position further away from the injector exit with increasing pressure for 25 nm PS spheres.

5.3.2 Simulation results

We observed the shift in focus position further away from the injector exit for 25 nm PS spheres with increasing injector pressure both in experiment and in simulations. All simulated particle-beam evolution curves are shown in the supplementary information, Figure S5. To describe the shift we took a closer look into the simulations and in particular the phase-space distributions.

The focus position is determined by the velocity vector $\vec{v} = (v_r, v_z)$ and the transverse position r of the particle. In a simple picture without any interaction between the gas flow field and the particles outside the injector, this vector determines the focus position and more general, its angle

particle size (nm)	p_{in} (mbar)	$w_{0,\text{exp}}$ (µm)	$w_{0,\text{sim}}$ (µm)	$z_{0,\text{exp}}$ (mm)	$z_{0,\text{sim}}$ (mm)
69	0.2	77(2)	68(1)	3.00(3)	2.41(1)
	0.6*	31(3)	26(1)	1.97(7)	1.76(1)
	1.8	15(1)	14(1)	1.44(3)	1.55(1)
42	0.2	124(9)	106(2)	2.51(7)	1.93(1)
	0.6*	40(4)	41(2)	1.72(5)	1.54(1)
	1.8	23(3)	25(2)	1.49(5)	1.66(2)
25	0.6*	67(9)	72(7)	1.41(14)	1.54(4)
	1.5	32(5)	49(1)	1.58(5)	1.81(1)
	2.0	33(3)	51(2)	1.83(3)	2.23(2)
	2.4	32(4)	54(1)	2.16(4)	2.67(2)

* exp. pressure 0.55 mbar

Table 5.1: Experimental and simulated values of the focus size w_0 and the focus position w_0 for different particle sizes and injector pressures. Errors are given as standard deviation of the Gaussian beam evolution fit to the data points. While the focus sizes fit quite nicely, the focus position is deviating, one possible reason being the size distribution and detection bias in the experiment.

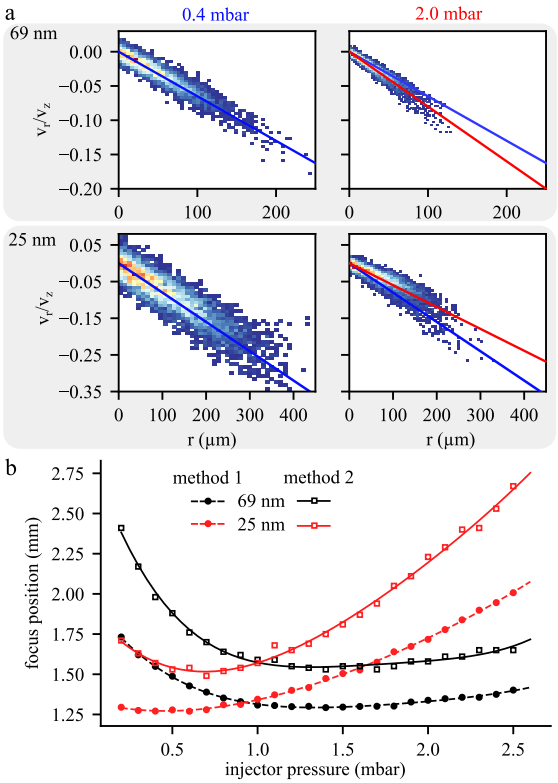

Figure 5.3: (a) Simulated phase-space distributions $v_r/v_z(r)$ at the exit of the ALS ($z = 0$ mm) for 69 nm (upper panel) and 25 nm (lower panel) at 0.4 mbar (left column) and 2.0 mbar (right column) injector pressure. The blue line through the principle axis at 0.4 mbar is shown in the right panel for visual comparison. The line through the principal axis at 2.0 mbar is shown in red. For 69 nm, the absolute value of the ratio increases, corresponding to a "steeper" focusing. For 25 nm, the absolute value of the ratio decreases, corresponding to a "looser" focusing. (b) Simulated focus position for 25 and 69 nm depending on the injector pressure. The focus position was determined using the phase-space values at the exit (method 1) and using the full simulation detectors (method 2). All focus positions determined with method 2 showed larger focusing values compared to method 1, indicating significant gas-particle interaction after the exit of the ALS.

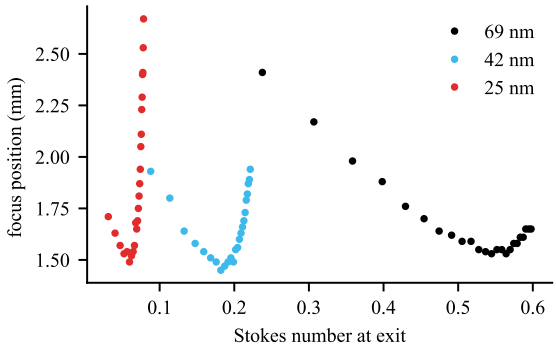

Figure 5.4: Simulated particle-beam focus positions with method 2, taking the particle-gas interaction after the ALS exit into account, depending on the Stokes number.

θ, see Figure 5.1. The angle θ can be expressed through the ratio of the transverse and longitudinal velocity components.

First, we looked at the histogram of the velocity ratios v_r/v_z and its dependence on the transverse coordinate r of the particles at the injector exit, $z = 0$. Figure 5.3 a shows the distributions for 69 (upper row) and 25 nm (lower row) PS spheres at 0.4 (left) and 2.0 mbar (right) injector pressure. All distributions showed a maximum at $(v_r/v_z, r) = (0, 0)$ and positive r had a negative velocity ratio due to negative v_r values. Negative v_r corresponds to a transverse velocity toward the center line $r = 0$ and thus, focusing of the particle beam. v_z was always positive, see supplementary material, Figure S6.

Both distributions changed with increasing injector pressure. For 69 nm, a smaller r space was occupied and the absolute value of the ratio v_r/v_z increased. This results in a larger angle θ, which results in a focus position closer to the injector exit. For better visualization of the change of v_r/v_z, the blue line through the principal axis at 0.4 mbar is shown in the 2.0 mbar distributions, too. The line through the principal axis of the distribution at 2.0 mbar is shown in red. For 25 nm, the situation was the opposite: With increasing injector pressure, the absolute value of the ratio v_r/v_z decreased, which results in a smaller angle θ and, therefore, in a focus position further away from the injector exit. For 25 nm the occupied r space decreases with increasing injector pressure, too. The separate v_r phase-space distributions are shown in the supplementary material, Figure S6. From the distributions $v_r(r)$ at $z = 0$, the focus position shift cannot be derived. The ratio v_r/v_z has to be taken into consideration.

We transferred the change of θ, i. e., the changing ratio of v_r/v_z with changing injector pressure into the focus position using (5.2), shown in Figure 5.3 b. Values for 69 nm, method 1, are shown as black dots and the dashed line is a polynomial fit to guide the eye. With increasing injector pressure, the focus position shifts closer to the injector exit from 0.2 to 1.4 mbar, stays at the same position and starts to move away from the exit from 1.8 mbar on. For 25 nm PS spheres (red dots), we observed a movement away from the ALS with increasing pressure only.

Additionally, we determined the focus position with method 2, taking the particle-gas interaction after the exit and corresponding velocity changes into account. These values are shown in Figure 5.3 b as squares with a solid line. The change of the focus position for the two particle sizes followed the behavior observed with method 1. However, the values are generally larger, i. e., the focus position is further away. We traced this shift back to the longitudinal velocity of the particles. The particles are accelerated in the diverging gas-flow field after the exit of the injector. The highest influence was observed for 25 nm PS spheres and the focus position at 2.5 mbar was the focus position furthest away from the injector observed of the three particle sizes.

The Stokes number, defined in accordance with [72], is a dimensionless parameter that governs

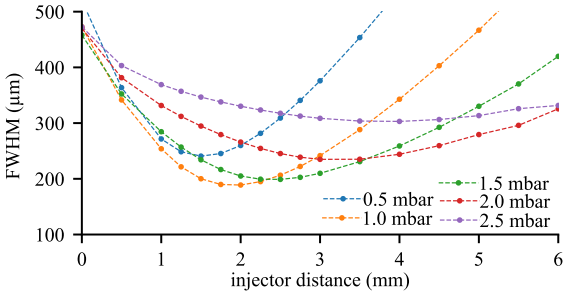

Figure 5.5: Simulated particle-beam evolution curves for spherical 10 nm protein-like nanoparticles at different injector pressures. From 0.5 to 1.0 mbar, the particle-beam focus size decreases. With higher pressures, the focus size increases. With increasing injector pressure, the particle-beam focus position moves further away from the injector exit.

particle focusing in an ALS. All parameters for the Stokes number calculation could be extracted from the flow field calculations. Figure 5.4 shows the simulated particle-beam focus position determined with method 2 for the three particle sizes depending on the Stokes number. In all used inlet pressure cases, the Stokes number is smaller than 1. For each particle size, the particle-beam focus position depending on the Stokes number follows the same behavior: With increasing Stokes number, the focus position decreases until a size-dependent critical Stokes number is reached and the focus position starts increasing with increasing Stokes number. To our knowledge, this behavior has not been shown before, as typical publications define the particle diameter at a fixed distance rather than following the complete particle-beam evolution [71]. For higher Stokes numbers, only a focus position shift towards the exit has been shown experimentally with increasing Stokes number ($0.8<St<2.1$) [100] and using calculations in a hyperbolic nozzle ($St>2.5$) [99].

In addition to PS, we simulated the particle beam for spherical 10 nm protein-like nanoparticles with a density of $\rho = 1400$ kg/m^3. The particle-beam evolution for pressures from $0.5 \ldots 2.5$ mbar in 0.5 mbar steps is shown in Figure 5.5 as FWHM of the particle beam depending on the injector distance. All particle beams showed focusing behavior. The focus position moved further away from the injector exit with increasing injector pressure. At 0.5 mbar, the focus position was at 1.5 mm, at 2.5 mbar, the focus position was at 4 mm. From 0.5 mbar to 1.0 mbar, the focus size decreased from 240 µm to 189 µm. In contrast to the simulations shown above, the focus size started to increase with injector pressures above 1.0 mbar, resulting in a particle-beam focus size of 300 µm at 2.5 mbar injector pressure. The shift of the particle-beam focus position can again be described by the ratio of transverse and longitudinal velocity v_r/v_z at the injector exit. The increase of the particle-beam focus size with increasing pressure from 1.0 mbar on was a result of a similar beam-width at the exit of the ALS: The same particle-beam radial distribution was focused with different velocity ratios, resulting in a looser focusing for smaller absolute v_r/v_z-ratios at higher pressures.

5.4 Discussion

Upon injector pressure increase, the particle-beam focus position is shifting. For larger NPs, the focus position shifts closer to the ALS exit at higher injector pressure, for smaller NPs, the focus position shifts further away. This behavior was observed both, in experiment and trajectory simulations. We described this opposing shift using the transverse/longitudinal velocity ratio of the NPs without the need for calculating Stokes numbers.

As a consequence, smaller beam diameters for smaller NPs can be achieved further away from the ALS exit at higher injector pressures, which reduces background scattering of the ALS housing

and shadowing of the ALS on the scattering detector. A higher injector pressure will result in more gas in the interaction chamber and gas density measurements or simulations have to show how much the background scattering from the gas will increase, while the hit rate due to better particle-beam focusing increases, too. Those two factors have to be considered when using the observed focus-shift effect for SPI experiments in the future.

The shown protein-like particle-beam evolution curves show a shift of the focus position with increasing injector pressure, too, but the focus size is increasing, in contrast to the 25 nm PS results. These simulations show the importance of parameter optimization (geometry and injector pressure) for each particle size and species.

The focus-shift effect observed here is a result of the used ALS and exit geometry, which increases the longitudinal velocity of smaller NPs more than the transverse velocity. A redesign of the exit aperture may result in different acceleration components so that the particle beam can be shaped upon specifications.

In general, room-temperature particle-beam generation is limited by Brownian motion, which is reduced with temperature. Therefore, generating a cryogenically-cooled particle beam should be preferred for those protein-like particles [54].

5.5 Conclusion

We presented the unexpected experimental results and simulations for particle-beam evolution curves of 69, 42 and 25 nm PS spheres. Both in simulation and experiment, we observed the particle-beam focus shift away from the ALS injector exit with increasing injector pressure for 25 nm PS spheres. The larger 69 nm PS spheres showed the expected shift of the particle-beam focus position toward the ALS exit with increasing injector pressure.

We described the focus shift using the velocity components at the exit of the ALS, which determines the focus position. We found the reason for small nanoparticles to focus further away: The longitudinal velocity increases much faster compared to the transverse velocity, resulting in a focus position further away. We highlighted the importance of an extended flow field after the ALS exit in the simulations up to 5 mm to include the acceleration of the particles after the ALS exit, which had a significant influence on the particle-beam focus position.

Furthermore, simulations for a 10 nm protein-like nanoparticle including the injector pressure dependency of the particle beam and extending the understanding of the focusing mechanisms of the ALS injector predicted a similar shift of the focus position away from the ALS injector, but showed an increase in focus width, underlining the importance of detailed particle-beam measurements and simulations prior to SPI experiments. Even though particle-beam formation for protein-like nanoparticles was demonstrated, the particle-beam focus width is rather large due to Brownian motion. Reducing the temperature will decrease this effect and improve particle-beam formation.

Our results improve the understanding of particle-beam formation for small nanoparticles from ALS injectors based on velocity components and phase-space distributions rather than Stokes numbers and show the possibility to use room-temperature particle-beam injectors for SPI experiments on smaller particles.

Chapter 6

Aerodynamic-lens stack injector with cryogenic cooling: [1]

Generating particle beams for single-particle x-ray diffractive imaging (SPI) experiments improves with lower nanoparticle temperature, especially for small particles where the Brownian motion is comparable to the drag force in a carrier gas flow field at room temperature. This work combines the previously published work on generating shock-frozen nanoparticles with diameters >200 nm with the work and knowledge of room temperature aerodynamic lens focusing: We designed and set up a *cryogenic buffer-gas-cell-aerodynamic-lens-stack* (BGC-ALS). We present the geometry, the setup changes to inject nanoparticles with diameters <100 nm, the accompanying particle beam simulations and measurements, including the challenges of operating the setup at cryogenic temperatures using electrospray ionization for aerosolization and propose future developments to come one step closer to the generation of pure beams of single proteins for SPI experiments and structure determination of isolated bioparticles.

6.1 Introduction

Retrieving the structure of isolated nanoparticles directly in gas phase is possible using single-particle x-ray diffractive imaging (SPI) with the intense and ultrashort pulses generated from x-ray free-electron laser (XFEL) facilities [3, 7, 25]. Due to *diffraction-before-destruction* a diffraction pattern can be recorded before the particle is destroyed by the deposited energy of the x-ray pulse [7]. Because particles are destroyed by the x-ray pulse, they need to be replaced constantly, requiring reliable sample delivery methods. In recent years, several successful experiments have been performed, showing the development in experiment and data analysis on the way toward the imaging of small bionanoparticles, such as proteins [34]. The experimental development reaches from sample delivery with the use of electrospray ionization (ESI) for aerosolization [61], improving the target-free aerosol injection setup with the use of (geometry optimized) aerodynamic lens stacks (ALS) [41, 45, 56, 70], and better optical detection of the nanoparticles for characterization in the laboratory [55, 80], to facility improvements such as x-ray beam focusing, and characterization, higher pulse energies, higher repetition rates and the corresponding fast read out detectors. However, the hit rate in these experiments is rather low: Depending on the used nanoparticles, a hit rate <1 % is to be expected. In this context, hit rate is understood as the percentage of detector images

[1] This chapter will be submitted to *Review of Scientific Instruments* for publication [58]. I performed the trajectory calculations and analyzed the simulated data. I contributed to the experimental implementation, recorded the data, analyzed the data and prepared the figures for the manuscript, wrote the first draft and updated the manuscript in discussion with all authors.

containing a sample of interest hit that is used for data analysis. In data analysis, new developments in classification of the diffraction patterns and noise reduction improve the retrieval of structural information [47, 101]. Improving the resolution of the retrieved structure from the experimental point of view lies in an increased purity of the sample asides a higher hit rate. The less impurities are present, the better the resolution. Impurities are structure related, such as clusters or spatial conformers, but also charge states may influence the structure of especially smaller nanoparticles and are considered impurities [102]. Recently, the charge-state distribution of nanoparticles from a gas-dynamic virtual nozzle was published, revealing high charge-states are present in the interaction region [103]. Separating conformers has been demonstrated for small molecules repeatedly and efforts are made to employ similar techniques to larger samples, such as dipeptides [60]. However, for small molecules the starting point is a cold molecular beam and achieving this for protein-like and -sized nanoparticles is one idea of improving sample injection for SPI experiments. Previously, generating a beam of shock-frozen nanoparticles has been demonstrated using a cryogenic buffer-gas cell (BGC) on large nanoparticles (diameters >200 nm) [54]. Aerosolized polystyrene spheres (PS) and virus capsids were injected into a cryogenically-cooled BGC filled with 4 K helium gas. After thermalization, the particles exit the BGC through an aperture into vacuum forming a particle beam. The detected particle beams are considered to be a good starting point for further control. Calculated cooling rates of $>10^6$ K/s for particle sizes below 50 nm were reported in the BGC, sufficiently fast to outrun structural changes during cooling and creating shock-frozen nanoparticles, exceeding the cooling rates typically used in cryo-electron microscopy (CEM) [75, 76].

This work focuses on the improvement of the setup toward the generation of particle beams of smaller nanoparticles via an ALS coupled to the BGC to generate particle beams with smaller beam diameters for higher particle-beam densities: a *cryogenic buffer-gas-cell-aerodyanmic-lens-stack* (BGC-ALS). Further experimental improvements were incorporated for the injection of smaller nanoparticles, such as coupling an ESI generator and modifying the injection part into the BGC. Accompanying the experimental work, three dimensional (3D) carrier gas flow fields of the BGC-ALS were calculated and particle trajectory simulations have been performed to understand the particle-beam formation and behavior of the particles inside the BGC-ALS.

6.2 Methods

6.2.1 Simulation setup

The overall BGC-ALS setup consists of an aerosolization part, a differential pumping stage, a transport part (source) into the BGC, the BGC-ALS itself and the particle detection. The simulation of the particle beam generated from the BGC-ALS is performed in four steps: First, the 2D cylindrically symmetric flow field of the carrier gas in the source is calculated using a finite-element solver for the Navier-Stokes equations [82]. The geometries of the used cylindrically symmetric sources are shown in Figure 6.1 a. As carrier gas, nitrogen at room-temperature is used with an initial pressure condition similar to the experimental values of 0.5 and 0.6 mbar. Second, the particle trajectories are calculated using CMInject [86]. As particles, we assume spherical particles with a diameter of 88 nm and a density of 1050 kg/m^3. Third, the 3D flow field of helium inside the BGC-ALS geometry is calculated. The geometry is shown in Figure 6.1 b as a central slice through the 3D structure. The flow field is calculated using OpenFOAM [83], a finite-volume solver for the Navier-Stokes equations, with the advantage of open-source availability and better solvers for compressible flow. The 3D flow field is calculated for different inlet helium flow values ranging from 5 to 25 ml$_n$/min at a temperature of 4 K. Fourth and last, the 3D particle trajectories for 88 nm PS inside the BGC-ALS are calculated using CMInject again. As input parameters

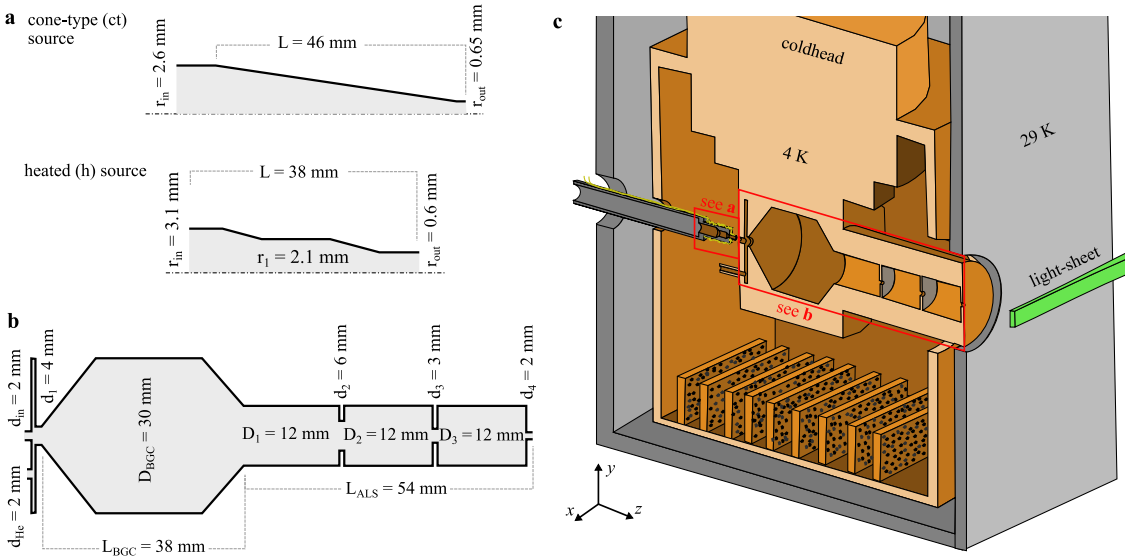

Figure 6.1: a.) Dimensions of the two used source geometries: the cone-type (ct) source and the heated (h) source. The ct source is made from a standard pipette-tip and the h source is made from copper, wrapped with a heating wire. b.) Dimensions of the BGC-ALS geometry shown on a 2D central cut in yz-plane. The BGC inlet and main part is similar to the geometry used in [54], the connection part has been modified. c.) Setup sketch of the inner setup parts. Depicted are the cryogenically cooled setup parts: An outer aluminum shield, cooled to 29 K and an inner copper shield at 4 K containing the BGC-ALS. The source is not connected to the coldhead, thus not cold. The generated aerosol passes a differential pumping stage (not shown here) before entering a transport tube and being injected into the BGC with a source. Here, the h source is shown. Particles follow the BGC flow field into the ALS section and exit the ALS. The particles are detected using a light-sheet imaging method.

for the particles' position and the velocity, the values from the source simulation are used. The interaction of the gas and the particles is modeled with the microscopic drag force [84].

The detector feature in CMInject is used to track the particles through the BGC-ALS. In 1 mm z-steps, detectors are placed. The result is a set of coordinates for each particle at the detector distance z_D: (x, y, z_D, v_x, v_y, v_z) with x, y and z_D the particles spatial positions and v_x, v_y and v_z the particles velocity components. To determine the particle-beam width, a 2D histogram in x and y of the particles position at each detector distance z_D is generated and a 2D Gaussian fit is used to determine the beam diameter as the mean of the minor and the major full-width at half maximum (FWHM).

The simulations of the particle trajectories are used to calculate the particle temperature and the cooling rate according to the previously developed microscopic drag force model [84].

6.2.2 Experimental setup

The experimental setup used in a previous publication [54] was improved with the following: an electrospray aerosolization source, an additional differential pumping stage, new sources for inserting NPs into the BGC and an ALS. The cryogenic part of the setup is shown in Figure 6.1 c in a cut representation. First, NPs are aerosolized via ESI using a commercial electrospray (TSI Advanced Electrospray 3482). Here, 88 nm polystyrene (PS) spheres (Alfa Aesar) in 20 mM AmAc are used with a concentration of 1.8×10^{11} particles/mL. The liquid flow rate is 230 nl/min. The generated aerosol is passing a differential pumping section with two pumping stages to remove excess gas and enter a transport tube. The pressure is reduced from nearly atmosphere in the electrospray device

to $0.5 - 0.6$ mbar source pressure. At the end of the transport tube, a modified injection source is used to inject the particles into vacuum at $3 - 4$ mm distance to the entrance of the BGC. For this experiment, two different types of sources were used: a cone-type (ct) source consisting of a standard plastic pipette tip attached to the transport tube and a heated (h) source made from copper, see Figure 6.1 a. The h source is wrapped with heating wire and kept at 49 ℃. Both source types are generating a diverging particle beam that allows a large fraction of the NPs to enter the BGC. The cryocooler consists of two cooling stages, cooled to base temperatures of 29.5 and 4.05 K, respectively. For additional higher temperature experiments, the base temperatures are 56 and 80 K, by balancing heating and cooling of the setup. The BGC-ALS is attached to the second stage of the cryocooler, see Figure 6.1 c. Pre-cooled helium gas is introduced into the cell from the entrance side of the NPs below the particles. Inside the BGC, the particles are introduced into the cold helium gas field. The particles follow the flow field through the BGC and the ALS and exit the ALS into vacuum through a 2 mm exit aperture. The chamber pressure is typically held between 8×10^{-6} and 4×10^{-5} mbar depending on the amount of helium introduced into the BGC. For the BGC-ALS geometry and dimensions, see Figure 6.1 b. The first part of the BGC geometry is taken from the previously existing BGC setup [54]. The ALS aperture and tube dimensions were adapted from room-temperature ALS injectors and varied in preliminary particle trajectory calculations to find a particle forming geometry. Within the ALS, the tubes and apertures can be changed individually, creating a variety of different ALS combinations. The NPs are detected via particle-localization microscopy using a light-sheet imaging method [55]. In short, NPs pass the focus of a cylindrical lens of a beam from a continuous wave laser system (Coherent Verdi V, max. 5 W, 532 nm) operated at 4 W laser power. The scattered light off the particles in the laser focus is detected using a camera-based microscope system. The recorded images are analyzed to determine the particle blob position and intensity. A histogram of the particle positions results in the transverse particle-beam profile. The beam diameter is determined from a 2D Gaussian fit on the transverse beam profile and taken as the average of major and minor FWHM of the fit. To ensure unblocked apertures of the BGC-ALS, light passing the BGC-ALS is detected on the particle-detection camera. If one of the apertures is blocked, no light is observed.

6.3 Results

6.3.1 Simulations

We calculated the 3D carrier gas flow fields for different helium flow conditions ranging from 5 to 25 $\mathrm{ml_n/min}$. The central slices through the 3D flow fields are shown in Figure 6.2 a for 5 $\mathrm{ml_n/min}$ and in Figure 6.2 b for 25 $\mathrm{ml_n/min}$ helium flow rates. The flow direction is from left to right. The black arrow indicates the entrance of the helium. The colormap shows the speed of the gas and is kept the same for both flow values, including the contour line values. The gas is exiting through both, the particle entrance and the ALS exit. Inside the larger volume of the BGC, the speed is reducing and increasing again in the ALS part toward the exit in both helium flow cases. While the flow field in the ALS part looks quite symmetric, the transition from the disk to the cell at 25 $\mathrm{ml_n/min}$ shows an asymmetry upwards (positive y).

Figure 6.2 c shows the simulated beam diameter (mean of major and minor diameter of the 2D Gauss fit) through the BGC-ALS for different helium flow values. The dotted gray line indicates the exit of the ALS at $z = 9.5$ cm. The input parameters are taken from the ct source simulations. These input parameters are equal for all helium flow values. For 5 and 10 $\mathrm{ml_n/min}$ helium flow (black and purple), the beam diameter is almost similar with only differences close to the exit and outside the ALS. At higher helium flow (orange), the beam is more diverging inside the BGC part.

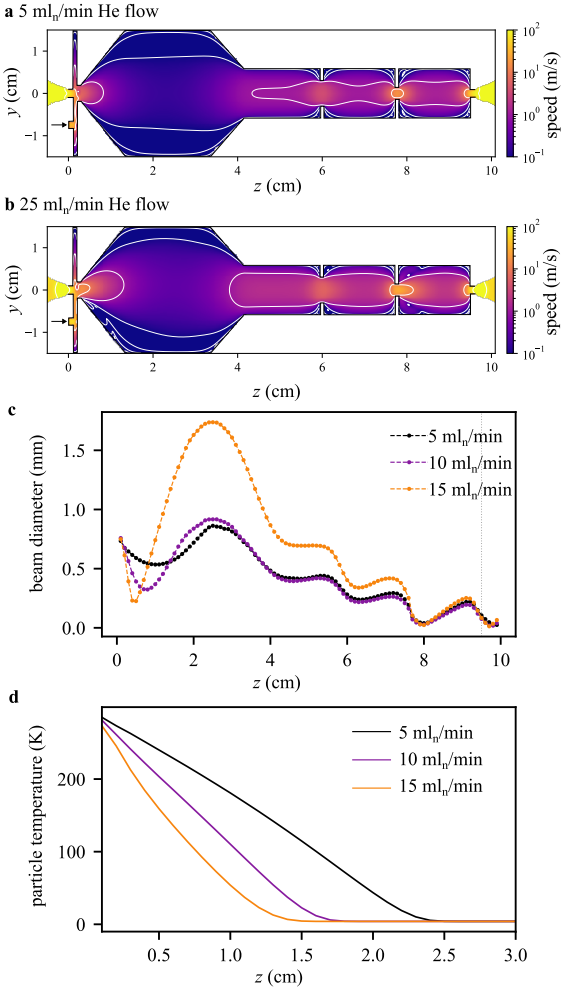

Figure 6.2: Central slice of the calculated 3D helium gas flow field inside the BGC-ALS for a.) 5 ml_n/min and b.) 25 ml_n/min helium flow rate. The gas inlet is indicated by an arrow below the particle inlet. The flow field shows an asymmetry at the entrance of the BGC which is more pronounced at higher gas flow inlet values. For comparison between a. and b., the same color map and contour lines (white) are chosen c.) Simulated 88 nm PS particle-beam diameter through the BGC-ALS geometry at different helium flow rates. The gray dotted line marks the exit of the ALS at $z = 9.5$ cm. d.) Particle temperature of 88 nm PS inside the BGC-ALS at different helium flow rates. At low helium flow, the particles temperature reaches 4 K within the first 2.5 cm of the cold helium flow field. At higher flow values, the temperature is reached earlier.

The beam diameter is increasing to >1.7 mm. The beam diameter outside the ALS is smallest at 15 ml_n/min at 2 mm outside the ALS with a diameter of 13 µm.

Here, only the beam diameter for helium flow values up to 15 ml_n/min are shown. For higher input helium flow values, simulations show a drastic and sudden decrease in particle transmission: The particles from the source do not have enough speed to overcome the pressure barrier created from the gas exiting the particle entrance.

The temperature of the particles is directly taken from the CMInject output and shown as a function of z in Figure 6.2 d. For 5 ml_n/min, 88 nm PS is thermalized while still being inside the BGC. At higher helium flow rates, this temperature is reached earlier. At 15 ml_n/min, the cooling rate is $2.2 \cdot 10^3$ K/s.

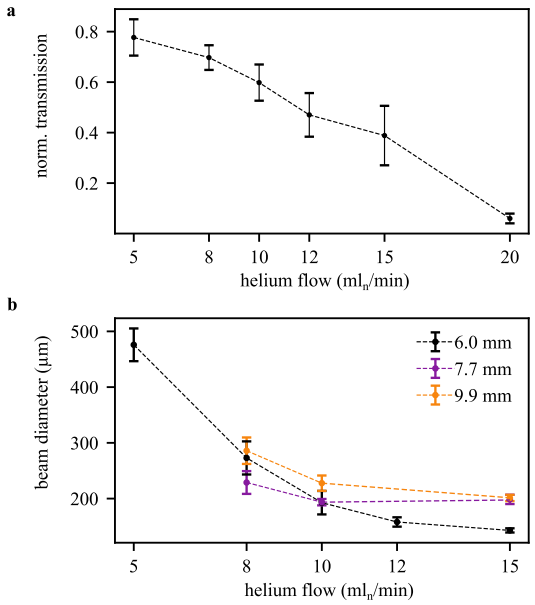

Figure 6.3: a.) Particle transmission depending on the helium flow inside the BGC for 88 nm PS using the ct source. b.) Particle-beam diameter depending on the helium flow at different detection distances. In general, a higher helium flow results in a smaller particle beam at the detection distances used.

6.3.2 Experimental results

First experiments were performed at 4 K cell temperature using the ct source for injection. With heating and cooling the cell in between measurements to avoid deposition of the injection gas on the apertures, we measured the transmission of the particles depending on the helium flow inside the BGC. For each scan, we normalized the measured number of particles to the maximum. The mean normalized transmission with standard errors is shown in Figure 6.3 a. The highest transmission is measured at 5 ml_n/min helium flow and decreasing with increasing flow. The transmission is close to zero at 20 ml_n/min helium flow, agreeing with our simulations.

The particle-beam diameter was measured depending on the helium flow at different detection distances. The result is shown in Figure 6.3 b. The values are given with standard errors. With increasing helium flow, the beam diameter decreases. The smallest beam diameter we measured is at a detection distance of $z = 6$ mm with 143 µm at 15 ml_n/min helium flow. By increasing the helium flow from 5 to 15 ml_n/min and detecting the particle beam at a fixed distance of 6 mm, the beam diameter decreased by a factor of 3.3 from 476 µm to 143 µm, see black curve.

During the injection of particles from the source into the BGC, the aerosolization gas (nitrogen and CO_2) is injected into the cold cell, too. We recorded the number of particles after the ALS depending on the injection time using the h source at 4 K cell temperature and a source pressure of 0.6 mbar with a helium flow rate of 10 ml_n/min in the BGC. The source was positioned 3 mm outside the BGC entrance. The time-dependent number of particles per frame is shown in Figure 6.4 a. Up to 45 min, the number of detected particles is constant at ≈ 0.02 particles/frame. Then, a drop is observed and no particles are detected after 55 mins. The data is approximated by a sigmoidal distribution (orange line). Experimental time at 4 K and these parameters is therefore limited to $45 - 50$ mins. Using a lower source pressure of 0.5 mbar increased the experimental time to $90 - 100$ mins. To understand the cause of the drop in the number of particles, we observed the pressure increase in the vacuum system while warming the cell. Figure 6.4 b shows the typical pressure increase in the pre-vacuum line when warming the cell after measurements. The cell temperature depending on the time after starting to heat the cell is shown in orange for both first

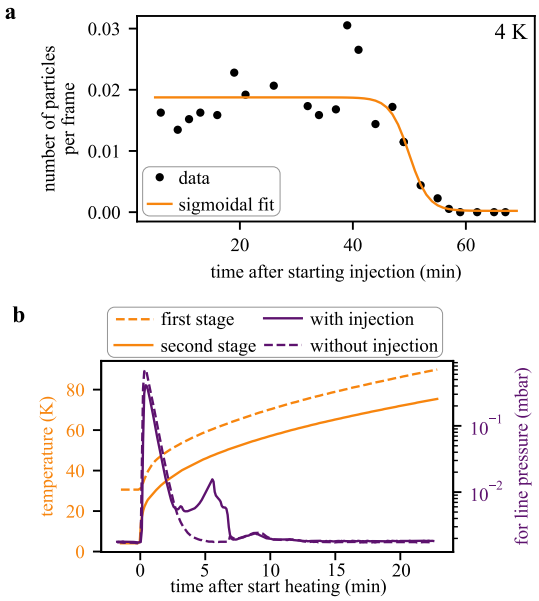

Figure 6.4: a.) Number of particles detected per frame depending on the time. The cell temperature was 4 K, the helium flow 10 ml_n/min and the source pressure using the h source 0.6 mbar. After 45 min the number of particles is decreasing and after 55 min no particles are detected (black dots). A sigmoidal fit was used to guide the eye (orange line). b.) Pressure profile during warm-up of the cell. The orange lines show the temperature increase in the first (dashed orange line) and second stage (solid orange line), the purple lines show the pressure reading in the pre-vacuum lines. Two cases are shown: warming the cell without previous injection (dashed line) and warming the cell after injection and blocking the cell as shown in a.) (solid line).

(dashed line) and second stage (solid line). The purple lines show the pressure increase for two cases: after heating without any injection (dashed line) and after injection (solid line). In both cases, helium was present at 10 ml_n/min in the BGC. Both pressure curves show an initial peak within the first two minutes, corresponding to a cell temperature of 4 . . . 40 K. The second peak is only visible after injection and shows up at 55 . . . 65 K cell temperature, pointing toward nitrogen release. A third smaller peak is present in both cases. After 10 min and at temperatures above 70 K up to 100 K no further pressure increase is visible. The drop in the number of particles and the pressure release at cell temperatures of $55 - 65$ K after injection indicates a blockage of the BGC apertures (entrance and first aperture) with nitrogen that freezes at low temperatures. Increasing experimental time and avoiding a blockage or even a partial blockage that may influence the flow conditions inside the BGC-ALS is of high priority. An easy solution was operating the cell at higher temperatures above the nitrogen freezing point. We operated the second stage cell at 80 K and were able to perform experiments for >8 hours. In an alternative approach, we tried breaking the thin ice layer at the entrance of the BGC with the tip of the h source, which has a smaller outer diameter than the BGC entrance, which was one of the reasons we moved from the ct source to the h source. This did not work reliably and left small fragments on the sides of the apertures. We monitored this with a microscope pointing into the ALS from the position of the particle detection camera.

In addition to experiments at 4 K cell temperature and to avoid short experimental time, higher temperature experiments were performed. We measured the transverse particle-beam profile for the h source and the same detection parameters at the two cell temperatures of 4 and 80 K. The transverse beam profiles are shown in Figure 6.5. Figure 6.5 a shows the beam at 4 K. The beam diameter is 198 µm. The beam profile at 80 K cell temperature is shown in Figure 6.5 b. The beam

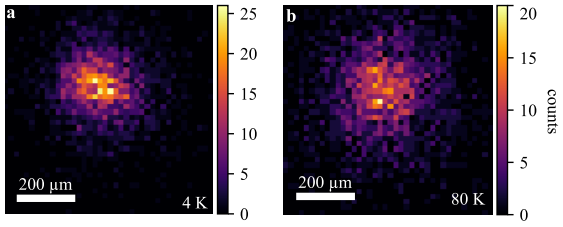

Figure 6.5: a.) Transverse particle-beam profile at 4 K cell temperature at 0.6 mbar source pressure using the h source at 49 °C with 3 mm distance to the BGC and 10 ml_n/min helium flow, detected 9 mm after the ALS exit. b.) Transverse particle-beam profile at 80 K cell temperature at the same experimental conditions as in a.).

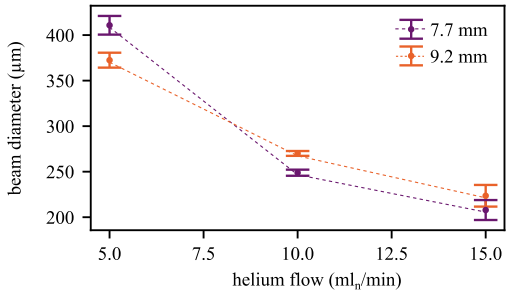

Figure 6.6: Particle-beam diameter depending on the Helium flow inside the BGC for two different detection distances. The h source was used and the cell temperature was 80 K.

diameter is 1.35 times larger compared to the 4 K beam with a diameter of 267 µm. Nevertheless, at 80 K cell temperature, generating a particle beam is possible.

We measured the particle-beam profile at higher cell temperature at two different distances and three different helium flow values. The h source was placed 3 mm outside the BGC entrance. The result is shown in Figure 6.6. With increasing helium flow, the beam diameter decreases, similar to the results at 4 K. The smallest beam diameter from these measurements is at 15 ml_n/min helium flow and 7.7 mm detection distance with a beam diameter of 208 µm. Detecting the particle beam closer to the ALS exit was not possible, due to stray light from the whole cryo-setup inside the vacuum chamber. At 4 and 80 K the position moved and the laser beam could not be moved closer than 7 mm without hitting any reflective structure inside the chamber.

In all experiments, we observed a transmission decrease at higher helium flow values inside the cell. Therefore, we moved the h source closer to and even into the BGC. We moved the source from 3 mm outside the BGC entrance to 5 mm inside the cell. The particle number and their intensity was recorded for three different injection mixtures: one with the same ESI settings and 88 nm particle concentration as in previous experiments and two mixtures containing only gas. The source pressure was kept constant by adjusting the pumping in the differential pumping stage and the gas mixtures contained 3.3 and 19.5 % CO_2, respectively. The helium flow rate inside the BGC was 10 ml_n/min. The recorded number of particles depending on the source position and the injection mixture is shown in Figure 6.7 a. Outside of the BGC (z<0 mm), we only detected particles when injecting the mixture with actual particles. This number is decreasing when moving the source closer to the BGC entrance. Inside the BGC (z>0) mm we detect lots of particles. Those particles show a large intensity distribution with higher intensity compared to the particle hits outside the BGC. Figure 6.7 b shows the intensity histograms of the detected particles for both inside (dashed) and outside (solid lines) when injecting only gas (orange) and gas plus particles (black). Outside the BGC, the detected particles show a narrow intensity distribution when injecting particles. Inside the BGC on the other hand, the intensity distribution is broad, extending to >10 times the

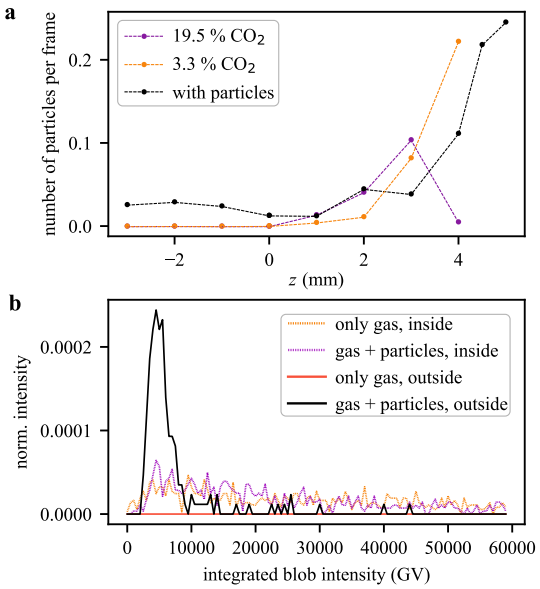

Figure 6.7: a.) Number of particles detected by the algorithm depending on the position of the source for different gas mixtures (19.5 % (purple) and 3.3 % CO_2 (orange)) and with 88 nm PS NPs (black). z-values are given according to the flow field notation: negative z-values correspond to outside the BGC, positive values are inside the BGC. b.) Histograms of the integrated blob intensities for different cases: injecting only gas with 3.3 % CO_2 in the mixture (orange and red lines) and gas+particles (purple and black lines) inside (dashed lines) and outside (solid lines) the BGC.

integrated intensity. The cases of injecting gas and gas plus particles (orange and black dashed lines) are so similar that a statement about detecting 88 nm PS particles cannot be made.

6.4 Discussion

The simulated beam diameters outside the ALS do not match our experimental observations quantitatively. This may be a result from using a laminar flow regime in the flow field calculations. Moving to a more suitable 3D direct simulation Monte Carlo (DSMC) approach may solve this. Current work is focusing on calculating new flow fields. Due to the complexity, it is not included in this mainly experimental publication. However, the qualitative behavior of the particles in the BGC-ALS could be explained.

The cooling rate of $2.2 \cdot 10^3$ K/s is lower than the reported cooling rate in [54] and lower than the critical cooling rate of 10^4 K/s reported in [75] to create amorphous ice. This is due to a much lower helium flow used here. Achieving higher cooling rates to ensure cooling the particles without any geometrical changes will be achieved with higher helium flow rates. Currently, higher flow rate values cannot be used, as the transmission is decreasing drastically for 20 ml_n/min and above. Nevertheless, a full thermalization of the particle and gas temperature was observed inside the BGC.

The particle-beam diameter detected at a cell temperature of 80 K is broader compared to the diameter at 4 K at the same experimental parameters. As the only parameter changed is the temperature, it is safe to assume Brownian motion as source for the broader particle beam at higher temperature. The stochastic force the particles are experiencing is proportional to the square root of the temperature. As the helium gas is not at 4 K, the heat transfer and cooling rate are lower for the high temperature measurements. Nevertheless, working and generating a particle beam at 80 K cell temperature worked well and experimental time was increased to >8 hours.

The most puzzling and for our understanding counter-intuitive results were obtained when moving the source inside the BGC and detecting lots of particles from the background. Without injecting any 88 nm PS, we observed many particles with high intensity. A dependence on the amount of CO_2 in the gas mixture could not be observed. Due to working below the CO_2 freezing point, it is likely we imaged solidified CO_2 flakes, which again underlines the importance of reducing the amount of gas in the ESI process and thus, injecting less of the gas into the cryogenically-cooled setup part. Even when injecting particles, they cannot be distinguished from the background particles, leaving behind a challenge for future experiments.

In general, extending the BGC geometry with an ALS worked well and no cooling capacity problems from the cryostat were observed. Problems arose from the use of ESI as aerosolization method instead of liquid jet breakup aerosolization,, which uses helium. In the current experiment, the use of nitrogen and CO_2 are the major concerns.

6.5 Conclusion

We showed the particle-beam generation of shock-frozen 88 nm PS in a BGC-ALS combination. We measured a particle beam with the diameter of 143 µm at 6 mm distance from the ALS exit at 15 ml_n/min helium flow inside the BGC. Even though the particle-beam width measured is rather broad, changes in the radiation shields or extending the ALS part outside the shield will provide access to the particle-beam focus which provides higher particle density. While using ESI for aerosolization at cryogenic temperatures, we showed the importance of background gas reduction to avoid freezing out of the gas and limiting experimental time. As easy solution, without changing the aerosolization source, working at higher cell temperatures was demonstrated. At 80 K cell temperature, we showed the particle-beam generation, which is considered good enough, but in the future, more time should be spend on working at 4 K by reducing the gas background, e. g. directly in the ESI process. We have shown that -against our understanding- inserting the source into the BGC did not increase the transmission of particles, but raised new problems with background ice particles, even at 80 K cell temperature. In addition, we showed the importance of simulations for understanding the particle trajectories inside the BGC and the importance for future designs.

Our work shows an important step toward generating a cryogenically-cooled particle beam consisting of single proteins, even though we are not there yet. To achieve this, several challenges have to be addressed, such as redesigning the BGC-ALS helium inlet to avoid asymmetries, optimizing the ALS apertures and changing the ALS exit to detect particles close to the exit. Another important step is the change of the flow field simulations. Using DSMC flow field calculations instead of laminar flow regime calculations may provide a better fit of experiment and simulation and will be more meaningful.

All these changes in the BGC-ALS setup will lead to a cold particle beam that may be used for further control, such as spatial separation of spatial conformers or alignment. In combination, these particle beams will increase the resolution of the resolved structure from SPI experiments by using a pure particle beam and reducing blurring of the resolved structures due to impurities. Even now, the particle beam consisting of cryogenically-cooled nanoparticles can be used for SPI experiments, for e. g. temperature dependent structure observations.

Chapter 7

Further improvements on sample injection

Even though the presented experiments were conducted on larger nanoparticles, the one major goal of SPI remains: imaging the structure and dynamics of proteins, i. e., sub-10 nm particles. From the sample injection perspectives, achieving a good hit rate, i. e., generating a particle beam with high particle number density at room-temperature is limited using current injectors and injection parameters. A few problems can still be resolved and future experiments will show how successful these attempts are. Those points will be discussed in the following chapter: the particle-beam generation, the optical detection, the setup geometry and the advantages and applications for cold particle beams.

7.1 Nanoparticle beams of 10 nm particles

The challenges in generating a particle beam consisting of 10 nm particles are mostly governed by the ability of transporting and focusing the particles into a stream of particles to be imaged with an x-ray pulse. The first step, i. e., the aerosolization in this size range is rather straightforward, as discussed in the following. Using ESI, the choice of buffer solution becomes more important, as residues on the particles may influence the structure and imaging quality more than for bigger particles due to the ratio of particle and residue volume. With careful ESI settings, even small bioparticles, such as the non-spherical Bovine serum albumin (BSA) with a diameter of around 8 nm, can be aerosolized using the ESI generator from previous experiments. An example of the aerosol droplet size distribution after spraying BSA is shown in Figure 7.1 a. The successful spraying is shown in the size histogram of the aerosol particles measured with a DMA-CPC device. The size histogram is shown for three different flow rate examples. The BSA monomer has the highest contribution at $d = 8$ nm. The number of particles is decreasing with decreasing flow rate and the peak position stays constant. This shows an already dry particle, i. e., no residue of the buffer solution, at the highest flow rate, which may lead to denaturation and a retuning of the ESI settings to ensure the BSA particles are in their native structure. The peaks at sizes smaller than the dimer correspond to doubly charged BSA monomers, as the DMA sorts the particles according to a mass-to-charge ratio or residues from the buffer solution. At 10 nm, the peak corresponds to a dimer. All diameters given here are the measured aerodynamic diameter.

The bottleneck of focusing small particles at current conditions is illustrated in Figure 7.1 b. Here, trajectories for 100 nm (red) and 10 nm PS (black) particles were calculated in the same flow field and plotted throughout the ALS geometry. The inlet pressure of the nitrogen carrier gas is

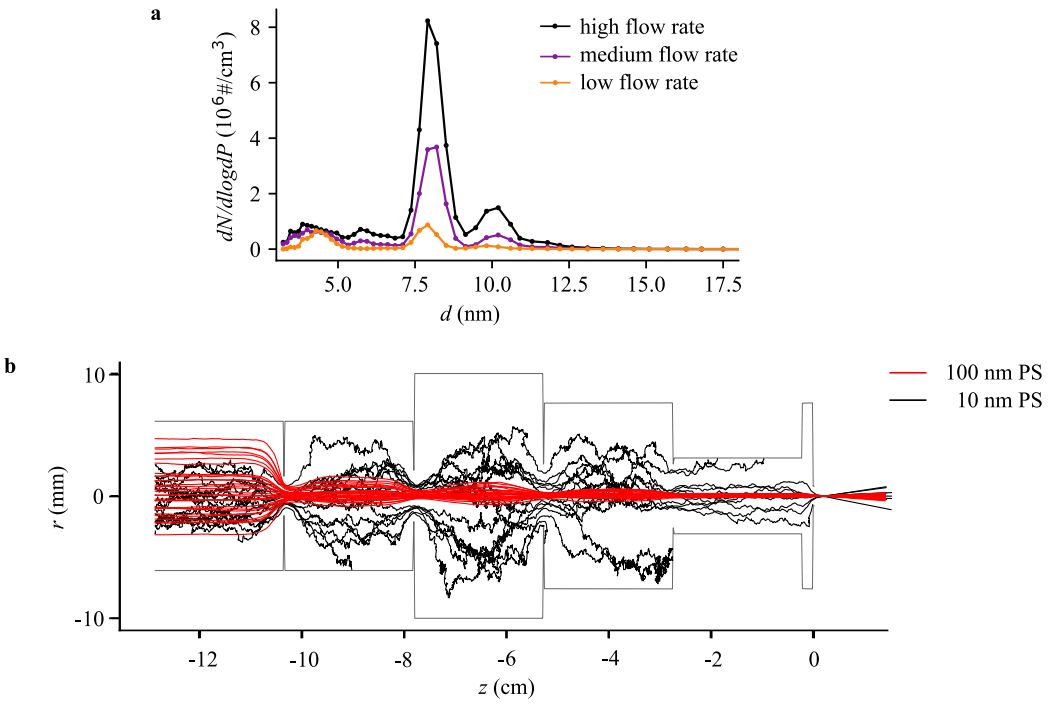

Figure 7.1: a.) Measured aerosol droplet size distribution of electrosprayed non-spherical Bovine serum albumin (BSA). The size histogram was measured with a DMA-CPC device for different liquid flow rates in the ESI process. The peak at 8 nm corresponds to BSA monomer. The number of particles generated decreases with decreasing flow rate (black to orange). In all cases, isolated BSA monomers are generated. b.) Calculated trajectories of 100 nm PS (red) and 10 nm PS (black) particles. For both, 50 particle trajectories were calculated for the nitrogen flow field with 1 mbar inlet pressure and the same initial parameters. The 100 nm trajectories show a good focusing behavior, whereas the 10 nm trajectories are dominated by Brownian motion and most particles do not exit the ALS, but hit the wall.

1.0 mbar, a typical injector pressure used during experiments, and the particles' initial parameters, such as particle position and velocity were the same for both sample sizes. Of course, to focus and transport smaller particles, the injector parameters should be adjusted. This discussion on the same flow field and particle parameters is used to demonstrate the challenge faced if no changes were to me made. While the 100 nm particles are focused in the flow field and exit the geometry without transmission loss, the 10 nm particles are moving around due to Brownian motion. The drag force is smaller than the Brownian motion, resulting in wiggles and particle loss at the walls. Inside the ALS geometry, the particle radial (r) distribution is larger than in the beginning, showing that this is not an ideal ALS geometry to generate a particle beam consisting of 10 nm particles, in addition to the particle loss at the walls. To be able to generate particle beams consisting of 10 nm particles or smaller, other ways of focusing have to be considered. A geometry optimization of the existing injectors may improve the particle transport, but a change of flow regime may be needed to achieve the required particle-gas interaction to focus 10 nm particles. As the drag force is proportional to the velocity difference of the particles and the gas, one solution may be to increase the gas velocity. As the pressure should not increase, smaller geometries may become necessary to reduce particle loss. The currently used ALS injector is not suited for generating a particle beam from 10 nm particles, but following the presented geometry optimization procedure and taking Brownian motion effects into consideration can increase the efficiency of sample injection.

In order to reduce Brownian motion and accelerate the carrier gas flow velocity, other geometries should be considered. Moving away from a simple box-type geometry of the individual pieces to a

rounded geometry guides the particles more smoothly through the geometry [104].

Another approach is the reduction of Brownian motion via cooling. Brownian motion is temperature dependent and reducing the temperature from room temperature to, e. g. 4 K may reduce it enough to focus the particles.

A fourth option may be a change in particle transport. The particles of interest may be covered in a non-evaporative shell that is transparent to the used x-ray photon energy. This way, the particles can be transported efficiently into the x-ray focus and are imaged in a shell that does not significantly contribute to the diffraction pattern. Of course, the shell material should not influence the particles geometry, dynamic properties or decrease the damage threshold [35].

It has been shown computationally, that the structure of a bioparticle can be extracted from the diffraction pattern of a bioparticle-gold complex from the diffraction patters of the combined and bare gold pattern with additional effort in the reconstruction algorithm. Due to the high scattering cross section of gold, a modulation caused by the bioparticle is visible and can be used for structure determination [105]. Again, this is only possible if the bioparticle structure is not much affected by the binding to a gold particle. In combination with AuNPs, bioparticles, e. g., BSA may experience time-dependent conformational changes [106].

7.2 Nanoparticle-beam detection

Within this thesis, the particle beam was characterized using optical scattering. The particles were illuminated with a green laser (CW or pulsed) and the scattering off the particles was detected using a camera-based microscope system. The problem with this method is the detection of small NPs. The scattering intensity is proportional to the sixth power of the particle diameter and is the critical parameter in detecting the particles. We have shown the particle detection down to 25 nm PS sizes with optical scattering, see chapter 5, but smaller particles vanished in the background of the camera images, even after careful background reduction. Other ways of detecting the particles position outside of an injector have to be investigated.

One example was published recently using ion detection [78]. The particles were ionized by an ultrafast mJ-level laser pulse and through scanning the laser focus, access to the transverse and longitudinal particle-beam profile was achieved. This method is applicable for spherical particles with diameters ranging from 10 . . . 120 nm. For future experiment, extending the ionization of small nanoparticles and proteins with a time-of-flight (ToF) measurement may be considered. Those measurements will even provide information about the fragmentation of the particles and the building blocks by measuring the mass-to-charge ratio of the fragments, as used in native mass spectrometry on small bioparticles, proteins and peptide sequencing [10, 107]. Also, laser-induced breakdown detection (LIBD) has been used to characterize a particle beam consisting of tryptophan nanoparticles with a diameter of 136 nm [77]. In this method, a laser produces a local plasma in the interaction with a single particle. The plasma emission is recorded in a photomultiplier tube.

One further destructive method of imaging the transverse particle-beam profile is using gel-deposition. A microscope slide with gel is positioned in the particle beam and collects the particles. Mounting the microscope slide on a manipulator allows to probe the particle beam at different distances from the injector. It has been demonstrated for large polystyrene nanoparticles (diameter between 500 nm and 2 µm) [59] and for characterizing an aerodynamic lens with deposition of size-selected nanoparticles (50 . . . 250 nm) on a substrate [37]. A challenge for smaller nanoparticles is imaging those on the structure. In that case, more advanced imaging methods on the deposited particles have to be used, e. g. transmission electron microscopy (TEM). Even though it has the disadvantage of needing a TEM facility, it may be a way to determine the particle-beam width for small nanoparticles and in addition confirm the bioparticles are still intact after injection, if the gel,

exposure to air and the time duration is taken into consideration that causes denaturation of the bioparticles.

7.3 SPI setup changes

So far, the proposed changes and challenges were focused on the setup in the laboratory. Changes in the beamline setup geometry may be of even more interest, as this is directly related to the quantity and quality of the recorded diffraction patterns. The main challenge is the signal strength compared to background scattering in current experiments [33]. One factor here is the gas background and scattering of nitrogen and, especially, CO_2 molecules in the interaction region. Those gases originate from the aerosolization process in the ESI. Changing the gas type to helium will decrease the background, but a different gas in the ESI process changes the neutralization, the transport of the particles and the focusing. Those transport and focusing challenges are solvable, as the setup has been used with helium before when using GDVN aerosolization. The neutralization part needs more construction and investigation. One way of determining of the amount of gas exiting the injector besides the flow field calculations can be the imaging via plasma-generation, which was demonstrated in helium exiting a convergent nozzle injector [88].

Often, a higher initial sample concentration may be generated in solution, but these high concentrations are likely to block the capillary in the electrospray. One solution may be the use of multiple nozzles/capillaries with a lower sample concentration and bring the combined generated aerosol with higher number of particles into the skimmer assembly. Depending on the availability of the sample, this may be a way to increase hit rates during the limited time at x-ray facilities. In the past, multiple designs of multiple nozzle use in ESI have been published, but did not find its way into use in SPI experiments yet and general applications so far because of performance problems caused by electrostatic cross-talk [108] or general operation problems due to high space charge that changes the flight direction of the charged aerosol droplets [109].

As shown in the previous subsections, in current ALS injectors, small nanoparticles are lost in the long ALS, see Figure 7.1. Shortening the ALS geometry will increase the transmission, too.

7.4 Pump-probe experiments

So far, the published experimental results of SPI at XFELs were exclusively reporting on static structures. One major interest is the observation of dynamics in a pump-probe scheme. An excitation event is used to trigger a specific dynamic process that leads to a structural change. Often, dynamics are triggered with an optical pump pulse. The probe is a second pulse, recording the structure of the sample, in time-resolved SPI this is an x-ray pulse.

A recent experiment (beamtime proposal number F-20190741, by CMI in collaboration with Holger Lange, *FB Chemie Universität Hamburg* and Kartik Ayyer, *MPSD Hamburg*) conducted at the CAMP endstation [110] of the *Free-electron LASer in Hamburg* (FLASH) in August 2020 used a pump-probe SPI scheme to observe the change in AuNP diameter upon plasmon excitation, so-called breathing dynamics. Until then, this change is AuNP size had only been observed indirectly in a AuNP solution experiment using transient absorption (TA) spectroscopy [111].

The schematic setup to directly image the size change of the AuNP upon plasmon excitation is shown in Figure 7.2. Aerosolized AuNPs with a diameter of $\approx$ 30 nm were injected into the x-ray focus using an aerodynamic lens injector [56]. The plasmon excitation followed after exposure of the AuNPs from a 400 nm pulse. With variable delay between pump and probe, diffraction patterns of the (excited) AuNPs were recorded on a pnCCD. The x-ray probe wavelength was

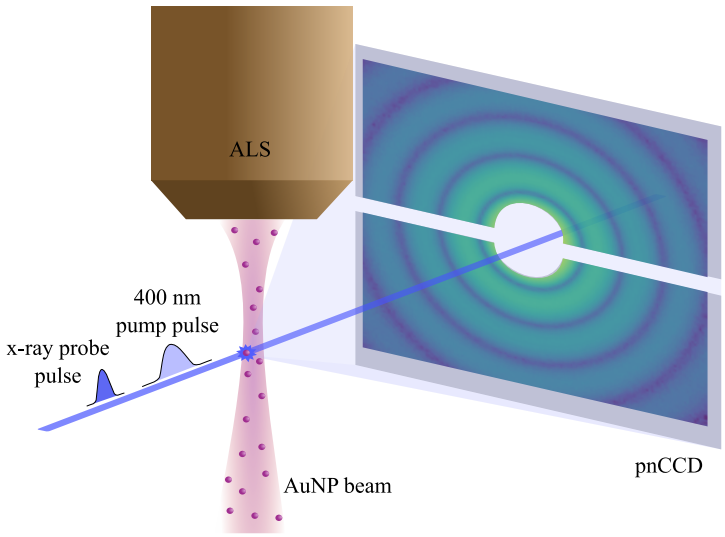

Figure 7.2: Schematic pump-probe setup. Aerosolized spherical gold nanoparticles were injected into the FLASH-x-ray interaction region via an aerodynamic lens. A pump laser pulse with a central wavelength of 400 nm was used to excite the plasmon breathing dynamics of the nanoparticles. The diffraction pattern was recorded on a pnCCD.

4.5 nm. An example of a simulated diffraction pattern is shown on the detector. The simulation of the shown diffraction pattern was performed using *Condor* [112]. For pump-probe delay times of $-2 \ldots 25$ ps, the size of the AuNPs was evaluated from the fringe distance of the diffraction patterns. The increase of the AuNP size leads to a closer spacing of the fringes. The observation of the AuNP size upon excitation yields an immediate particle expansion and pump fluence dependent breathing oscillations.

This experiment showed the successful use of time-resolved SPI and the direct observation of the size change of a AuNP upon plasmon excitation. A publication was submitted [113].

Implementing pump-probe schemes in future experiments will open the field of time-resolved SPI measurements and access to protein dynamics upon optical laser excitation.

7.5 Cold and pure nanoparticle beams

The work on cold cryogenic nanoparticle beams in this thesis was limited to nanoparticles with diameters >88 nm. Decreasing the size of the particles in this setup and detecting a particle beam consisting of small and shock-frozen sub-10 nm particles is the next step. Once this is achieved, more particle-beam manipulation can be used to generate pure and controlled beams for increasing the resolution in SPI experiments. To manipulate the particle beam, knowledge from small molecular beams can be applied, for, e. g., separating spatial conformers or alignment and orientation of the particles.

The spatial separation of spatial conformers has been shown for various neutral molecules and clusters, see, e. g., [48–50] and even for model dipeptides [60]. The spatial separation is a result of spatial deflection in an inhomogeneous electric field, generated by an electrostatic deflector [48]. The spatial deflection is due to the dc-Stark effect [48, 114]. In short, different conformers have different permanent dipole moments and therefore, their interaction with the electric field is different and changing the molecules energy in the field. The force the molecules are experiencing in the electric field is directly proportional to the effective dipole moment μ_{eff}, which is the first derivative of the Stark energy. Molecules with different μ_{eff} follow different trajectories in an inhomogeneous

field and therefore, are spatially separated. The amount of spatial deflection depends on the dipole-moment-to-mass ratio for a given gradient of the electric field, meaning: As long as the effective dipole moment difference of different conformers is large enough, i. e. a large enough difference in the positioning of the atoms in the molecule, separation is theoretically achievable. Applying separation of spatial conformers to larger systems such as proteins and nanoparticles was part of the PhD thesis of my colleague Jannik Lübke [115].

Another principle that can be adapted from small molecules is the alignment of the particles. A recently published model for the polarizability tensor of macromolecules and proteins is the first step to predict alignment of larger particles [116]. Current efforts in our laboratory (by Xuemei Cheng and Lukas Haas) are focused on aligning nanorod structures using adiabatic alignment with room-temperature particles [117]. Alignment, i. e. fixing the molecular axis in space is an idea from small molecules to study, e. g., orientation dependent chemical reactions [118]. Using field-free alignment, it was possible to record a molecular movie of rotational motion of OCS [119]. Applying those alignment techniques to asymmetric nanostructures is under current investigation and development in our group. It will reduce SPI data analysis complexity due to a fixed orientation angle of the investigated particles.

Chapter 8

Conclusion and outlook

The incentive of the work performed in this thesis was the improvement and application of aerosol particle injectors for single-particle diffractive imaging experiments toward imaging smaller nanoparticles and potentially, proteins.

Within this work, important steps toward improving single-particle imaging experiments were reached, ranging from detection methods of the particle beam in the laboratory and optimizing existing aerodynamic-lens stack injectors to improving sample delivery via cooling of the particles using a cryogenic buffer-gas cell. Characterization methods are especially important to reduce beam time preparation and increase on-site efficiency at the FEL facilities.

Overall, this work followed a top-to-bottom approach. The work started with generating room-temperature particle beams consisting of large nanoparticles with diameters above 200 nm, followed by experimental improvements down to smaller nanoparticles with diameters of 25 nm, and generating cryogenically-cooled particle beams consisting of 88 nm nanoparticles. Combining the gained knowledge, improving and developing aerosol particle injectors for SPI experiments is advancing toward efficient aerosol particle-beam injectors for small bioparticles and proteins. The generated particle beams at room temperature and at cryogenic temperature are well-suited for further control of the particle beam and structure determination via single-particle imaging to improve the purity of the particle beams for imaging. The cryogenic particle beams generated do not only have valuable applications and improvements for SPI experiments, but provide a tool for controlled temperature-dependent structural changes on bioparticles.

The optimized setup presented in this thesis was used for one pump-probe experiment on gold-nanoparticle breathing dynamics. This experiment clearly shows the possibility for time-resolved measurements of samples in aerosolized particle beams using x-ray diffractive imaging. However, the ground breaking scientific outcome regarding high-resolution structure determination of small bioparticles resulting directly from the work of this thesis is yet to come. Nevertheless, the work presented in this thesis provides the necessary tools and ideas to do so in the future.

With the proposed improvements especially in background gas scattering reduction and particle-beam generation via cooling, single-particle imaging adds a powerful technique with the potential for temporal measurements to the imaging techniques of bioparticles besides native mass spectrometry, serial femtosecond crystallography and cryo-EM and completes the understanding of biologically relevant processes in nature.

Supplementary material for chapter 4

Gas-flow effects on focusing

We simulated the particle beam for 50 nm AuNP for the optimized injector and the "Uppsala-injector" (AFL100) for different nitrogen gas mass flow. The resulting values for the particle velocity and the focus size are shown in Table 8.1. With increasing nitrogen mass flow, the mean velocity increased and the focus size decreased for both injectors. At the same mass flow, our optimized injector showed slightly larger mean velocities and slightly larger focus sizes, which does not make a significant difference.

Focusing 10 nm AuNPs

A principal and longstanding goal of single particle diffractive imaging is to image a single protein [7]. Toward this goal of smaller nanoparticle sizes, we simulated the focusing of 10 nm AuNP spheres by the AFL100 and our optimized ALS geometry, assuming a mass flow of 13 mg/min. The beam-size evolution is shown in Figure 8.1. We see the same behavior for larger particles: The beam focus size is comparable, 109 µm for the AFL100 and 115 µm for our injector, and also the speed of the particles is similar for the two injectors, 54±7 m/s compared to 56±5 m/s. The main difference occurs in the focus position, i. e., 1.13 mm and 2.13 mm, and the transmission. For the AFL100 only 59 % of the particles are transmitted through the whole ALS, whereas our injector transmission reaches 79 %. The focus position further away from the injector tip strongly reduces the background signal from gas scattering, i. e., in this case from 0.054 mbar to 0.01 mbar. The pressure map is shown in Figure 8.2. It shows the pressure drop after the exit aperture. For these calculations, we calculated the flow field in an extended region shaped as a cone up to 5 mm after the exit. Similar behavior of pressure drop after a convergent nozzle has been shown experimentally [88].

	optimized injector		AFL100	
mass flow (mg/min)	mean velocity (m/s)	focus size (µm)	mean velocity (m/s)	focus size (µm)
5	-	-	18	46.2
10	26	39.2	24	27.6
13	29	32.4	27	23.2
20	35	23.4	33	17.4
30	40	18.0	39	13.8
50	50	13.0	-	-

Table 8.1: Detailed values from 50 nm AuNP simulations for the optimized lens and the "Uppsala-injector" (AFL100) for different mass flow inlet values.

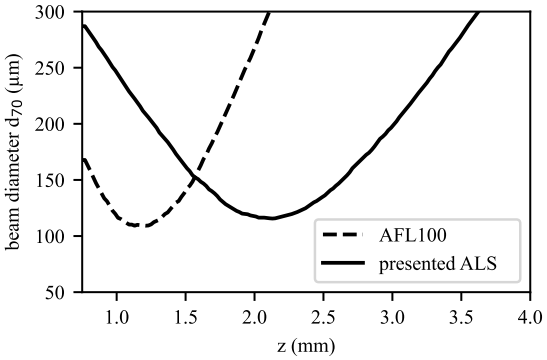

Figure 8.1: Particle beam evolution for 10 nm AuNP spheres at 13 mg/min mass flow for the AFL100 (dashed line) and our 50 nm-AuNP-optimized injector (solid line).

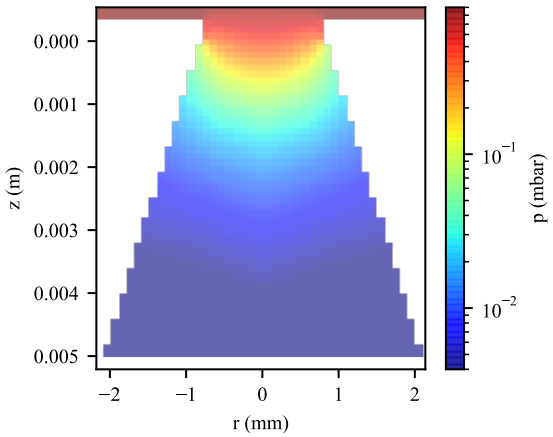

Figure 8.2: Pressure map in an extended region after the ALS exit at 13 mg/min mass flow.

lens piece n	pressure (Pa)	Mach number	Reynolds number	Stokes number
0	102.4	0.12	8.4	1.36
1	98.7	0.07	6.3	0.59
2	97.2	0.05	5.0	0.31
3	96.5	0.05	5.2	0.31
4	94.5	0.65	20.5	11.77

Table 8.2: Mach number, Reynolds number and Stokes numbers at the different lens pieces through the optimized injector. The values of the pressure were taken from the calculated flow fields.

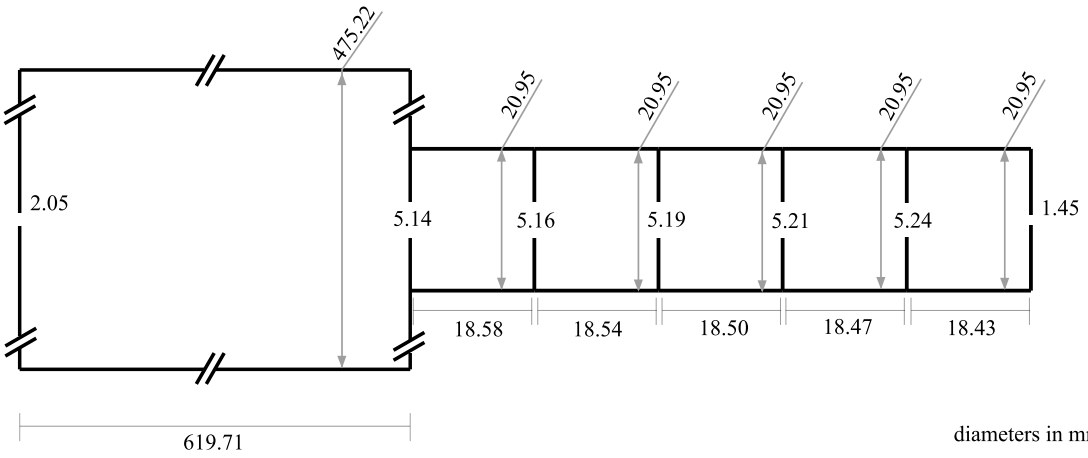

Figure 8.3: Geometry of the aerodynamic lens system as a result of the lens calculator [72]. Particle and gas flow are from left to right. Values are given as diameters in mm.

Optimized Geometry Flow Parameter Discussion

We calculated the Mach-number, Reynolds-number and Stokes number as defined in [72] for 50 nm AuNPs in our optimized geometry. The results are shown in Table 8.2. The Stokes numbers are very close to the optimal Stokes number for the pressure range we are working in. In our geometry, the Stokes number at the first aperture r_0 is larger than the optimal Stokes number (≈ 1), resulting in the crossing of the center line of the particle trajectories [70] (see details in main manuscript). However, the main concern in crossing the center line and the diverging particle-beam is particle loss, which is not observed in our case. All particles that are transmitted until the first aperture are transmitted though the whole lens geometry.

Lens Calculator Results

We used the lens calculator [72] with input parameters of Nitrogen as the carrier gas at room-temperature, 115 Pa pressure before the inlet, so that the pressure in the relaxation chamber was comparable to the pressure in our injector before the first lens (103 Pa). The volumetric flow rate of 0.01 slpm corresponds to 13 mg/min in our optimization and the particle properties were set to a density of 19320 kg/m^3 and a diameter of 50 nm. The geometry from the lens calculator yielded a non-optimal particle-beam for the 50 nm AuNPs with a focus position inside the ALS. The generated particle-beam had a diameter after the exit of 798 µm and of 817 µm at 5 mm distance according to the output of the lens calculator. The geometry is shown in Figure 8.3 with the calculated diameters of the apertures, tubes and the length of the tubes next to it. In contrast to our optimized injector geometry, all tube diameters were equal [70]. The transmission of the

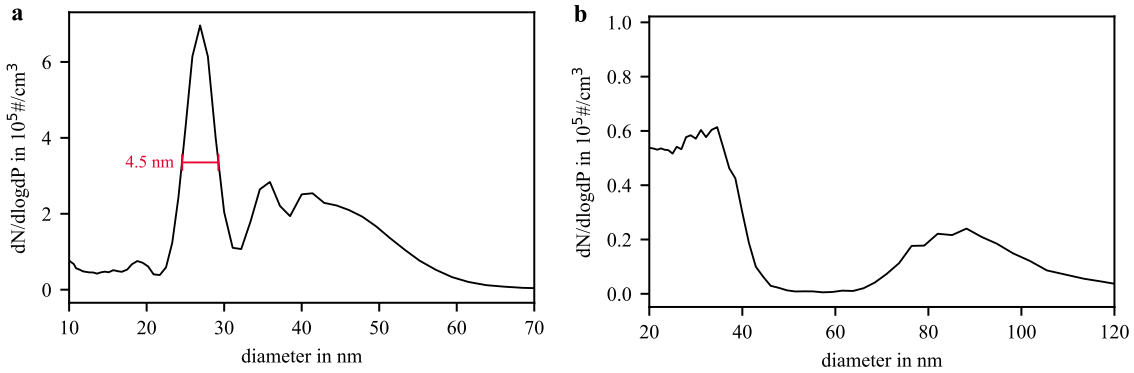

Figure 8.4: DMA-CPC size distributions measured for (a) gold spheres and (b) 2 % sucrose solution. The conditions for the experiment are kept constant from the DMA measurements.

geometry was given with 87 %.

In comparison, our optimized injector showed a higher transmission and a focused particle beam with a focus width of 33 µm.

The lens calculator is a useful tool to calculate the geometry quickly, but cannot be used to optimize the geometry based on the particle-beam properties.

Sample Preparation

AuNPs

Citrate-capped spherical AuNPs (Sigma Aldrich) were ligand-exchanged, purified, and concentrated. As XFEL diffractive imaging is highly sensitive to the size of the particles interacting with the XFEL beam one needs to have highly-pure, salt- and impurity-layer-free target objects delivered to the interaction region. To mimic the XFEL experimental conditions in the lab-based optical-laser imaging, we used highly-concentrated AuNPs in a volatile buffer to get consistent size distributions with different flow-rates upon electrospray aerosolization, which was characterized using ES DMA-CPC (TSI, 3080 and 3786). Commercial samples as well as self-grown unpurified AuNP samples contain unwanted impurities and salts, which would impede the electrospray injection and not giving consistent size distributions with different flow rates. Citrate-capped AuNPs were ligand exchanged with bis(p-sulfonatophenyl)phenylphosphine dihydrate dipotassium salt (BSPP) (Sigma-Aldrich), to avoid aggregation at high concentration and different conditions like repeated centrifugation during the purification [120]. Phosphine coating increases the overall negative charge of the particles and thus increases the stability of particles at a range of buffer conditions.

Briefly, 100 ml of AuNPs were incubated with 40 mg of of BSPP overnight, and then 5 M NaCl was added dropwise to the AuNP dispersion, until the color changed from red to dark blue. The blue dispersion was centrifuged at 1600 rcf for 30 min. The salty supernatant was discarded and the pellet was resuspended in 1 ml 2.5 mM BSPP and 1 ml methanol, centrifuged again (1600 rcf, 30 min), and resuspended in 1 ml 2.5 mM BSPP. The resulting AuNP solution was of burgundy-red color. Then the AuNP were centrifuged (Eppendorf) further 6 times at 2000 rcf for 15 min each, and redispersed in 250 µl Milli-Q water with 2.5 mM ammonium acetate. This process was optimized until the correct AuNP size was obtained for different flow-rates in the ES-DMA consistently as shown in Figure 8.4 a for the ES settings used during the experiment. A broad distribution at larger diameters from 30 to 60 nm was observed and ascribed to dimers generated in the ES process. We experimentally exclude larger (brighter) particle hits in our scattering experiment later.

UV-VIS-spectroscopic characterization (Nanodrop) of AuNPs after ligand exchange did not show

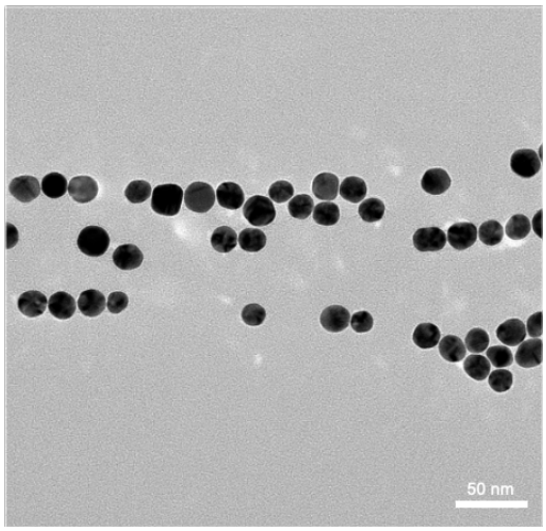

Figure 8.5: TEM image of AuNPs after ligand-exchange in 2.5 mM ammonium acetate. The core-size ranged from 18 to 26 nm with an average of 24 nm. The scale bar is 50 nm.

indication of any aggregation and was consistent with the surface plasmon resonance (SPR) peak before ligand exchange and purification. The TEM analysis indicated the average core diameter of the AuNPs to be 24 nm, providing further indication that the larger particles detected in DMA-CPC were dimers created in the ES process. The mean size was calculated from TEM-based sizing for a sample size of 500 AuNPs, see Figure 8.5.

Sucrose

In addition, a 2 % sucrose solution was used to generate sucrose balls in the electrospray process. The size distribution of the generated sucrose balls is flow rate dependent. A DMA size distribution taken at the same electrospray settings as in the experiment is shown in Figure 8.4 b. We fitted a Gaussian distribution to the second peak. The peak particle size is 88 nm and the size distribution is rather broad with a FWHM of 29 nm. At this flow rate we also generated small sucrose spheres with diameters < 40 nm, see Figure 8.4 b. Decreasing the laser intensity and setting boundaries in the data analysis can be used to neglect those particles. In our experiment, we used similar flow rates as for the DMA measurements.

Data Analysis

The collected light-scattering images were analyzed using a centroiding algorithm based on Hessian Blob-finding [81]. The blob-center positions at $z = 2.61$ mm are shown in a 2D histogram in Figure 8.6 a. Due to an imperfect laser beam profile we detected particles outside the laser focus region, which were removed from the dataset by restricting the analysis to the region of the laser path, i. e., the red box in Figure 8.6 a. In addition to the blob-center position the algorithm provided the integrated intensity of the blob. A resulting intensity distribution is shown in Figure 8.6 b, showing the same shape as the DMA data in Figure 8.4 a. To analyze the focusing of 27 nm AuNPs we restricted our further analysis to particles with an integrated intensity in the red marked region in Figure 8.6 b. The remaining centroids are projected onto the laser propagation axis (x-axis), as shown in Figure 8.6 c. From this distribution, we determine the beam diameter as d_{70}.

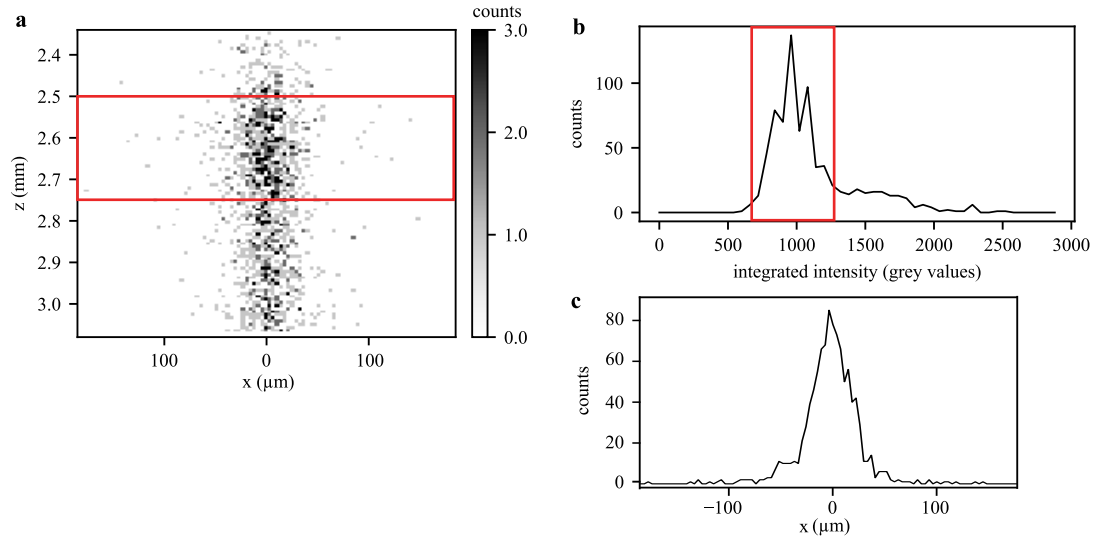

Figure 8.6: (a) 2D histogram of the found particle blob center positions at $z = 2.61$ mm distance from the ALS exit of AuNPs. The red marked region is the actual region of the laser focus, which limits the analysis to particles in this region. (b) Integrated intensity distribution of the particle blobs. It shows the same pattern as the DMA data, see Figure 8.4 a. We limit the analysis to the first peak, corresponding to AuNPs with a diameter of (27±2.25) nm. (c) Projection of the sorted particle positions onto the x-axis. From this distribution, we determine the beam diameter as d_{70}.

Supplementary material for chapter 5

Experiment

Experimental Setup

We used the setup described in [56] with three improvements: adjustable pumping between the skimmers, a post-sample aperture and the modified injector exit.

The setup is shown in Figure 8.7 a and explained in detail in [56]. In short, the setup is divided into three different parts: the aerosolization and transport, the particle-beam formation and the detection of the particle-beam. We used an electrospray (TSI Advanced Electrospray 3482) with capillaries of 40 µm inner diameter and an angle of 30 degrees. The sample flow rate was kept between 400 and 650 nl/min. The excess gas from the aerosolization process was pumped away using a double-skimmer assembly. In contrast to previous publications, we used a smaller first skimmer with a diameter of 0.2 mm. All skimmer diameters and distances are shown in Figure 8.7 a.

The particle-beam was generated from an aerodynamic lens stack (ALS) presented elsewhere [56]. We modified the injector exit for our measurements, see Figure 8.7 b. The modified injector exit allowed us to measure the particle-beam profile as close as 1 mm distance from the last aperture at full laser power. The modification is shown in Figure 8.7 b and was included in all our flow-field calculations. We fixed the last aperture outside the ALS housing with two-component epoxy glue.

To image small nanoparticles, we needed a clean camera background image. Therefore, a post-sample aperture (PSA) was implemented around the inverted camera window flange to avoid diffuse scattering from inside the vacuum chamber into the microscope. The PSA consisted of a black foil covering the window with a circular hole with a diameter of 3 mm.

Experimental Particle-Beam Profiles and Beam Evolution

All measured 1D particle-beam profiles showed a Gaussian distribution. Two examples of 42 nm PS are shown in Figure 8.8. The 1D distribution is a projection of the 2D histogram of the recorded particle centroid positions from the side-view imaging data acquisition. Figure 8.8 shows the distributions at $z = 1.5$ and $z = 4.0$ mm and an injector pressure of 1.8 mbar. At this injector pressure, the focus of the particle-beam was determined at $z = 1.49(5)$ mm and a width (FWHM) of 23(3) µm. The center of the particle-beam changes with distance from the injector due to a slightly misaligned ALS injector in x.

We measured the particle-beam evolution for three particle sizes at different injector pressures. All measured data is shown in Figure 8.9 with standard deviation errors and the corresponding Gaussian beam evolution fit we used to determine the particle-beam focus position and the focus width. All beam evolution fits agree reasonably well with the acquired data.

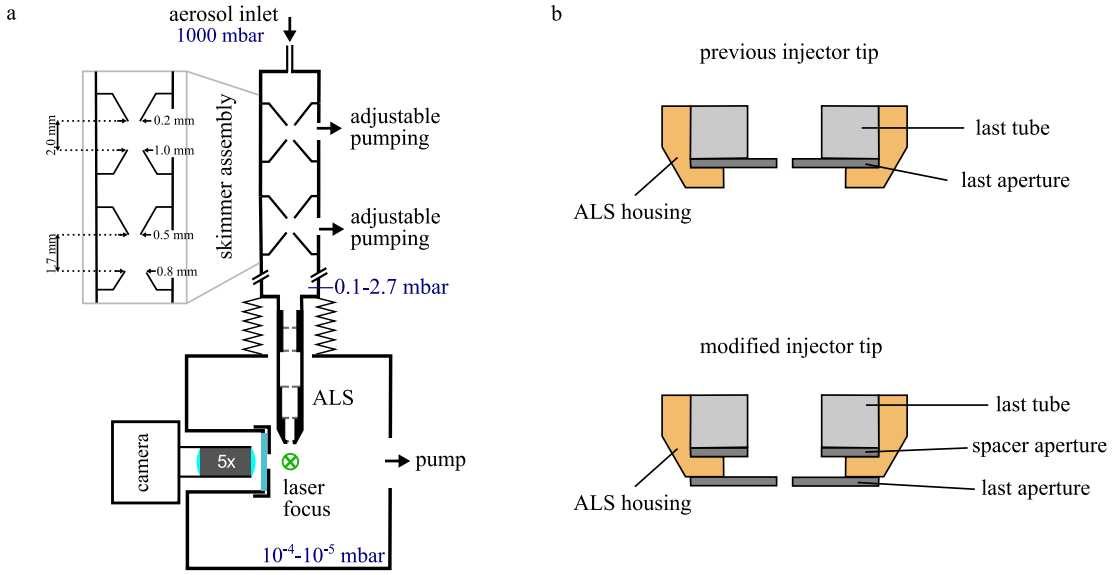

Figure 8.7: Experimental setup modifications. (a) Detailed schematic setup used in the particle-beam evolution measurements. The changes included a different skimmer configuration, adjustable pumping in both skimmer stages, a post-sample aperture to reduce scattering from inside the chamber on the camera images and a modified ALS exit. (b) Modification of the ALS exit. The previous injector tip is shown in the upper part. Accessing close distances from the last aperture was prevented from the ALS housing. The modified injector tip (lower part) allowed to access closer distances to the last aperture. The last aperture was fixed outside the ALS housing. The changed geometry of the exit is included in all simulations.

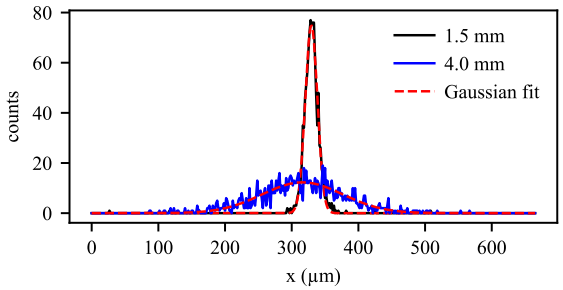

Figure 8.8: Example particle beam projections for 42 nm PS at 1.8 mbar inlet pressure at $z = 1.5$ mm (black) and at $z = 4.0$ mm with the corresponding Gaussian fit (dashed red line) to determine the width of the particle beam.

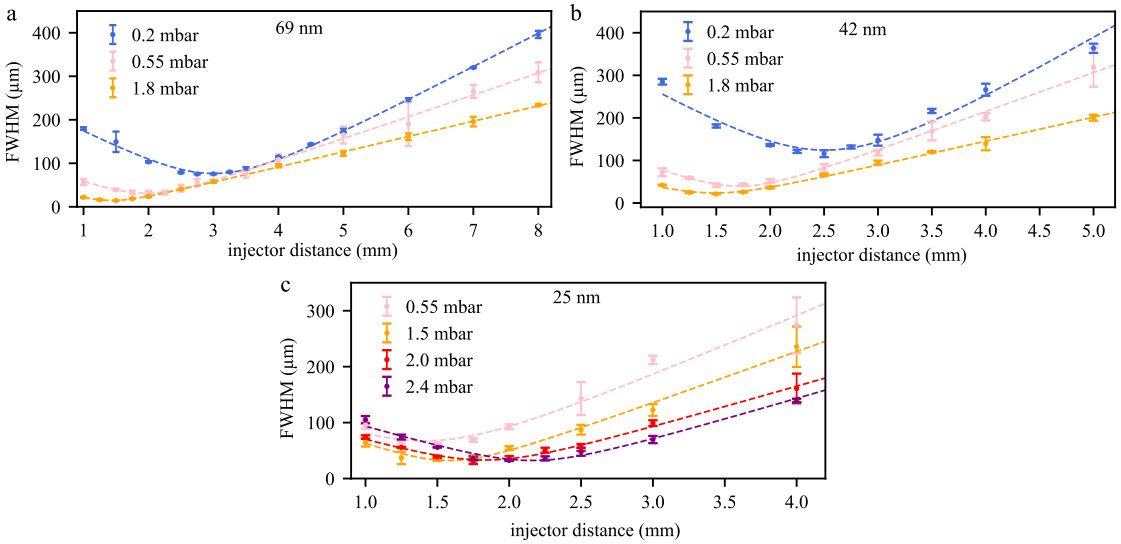

Figure 8.9: Particle beam evolution curves for all three sizes at different injector pressures. The data is shown with standard deviation errors and a Gaussian beam evolution curve fit (dashed lines). (a) Particle beam evolution curves for 69 nm PS spheres at 0.2 (blue), 0.55 (pink) and 1.8 mbar (orange) injector pressure. (b) Particle beam evolution curves for 42 nm PS spheres at 0.2 (blue), 0.55 (pink) and 1.8 mbar (orange) injector pressure. (c) Particle beam evolution curves for 25 nm PS spheres at 0.55 (pink), 1.5 (orange), 2.0 (red) and 2.4 mbar (violet) injector pressure.

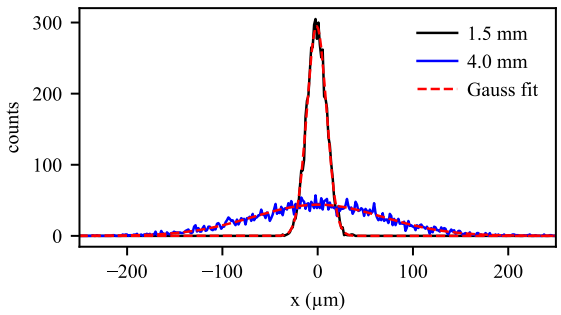

Figure 8.10: Simulated 1D particle-beam profiles for 42 nm PS at 1.8 mbar inlet pressure at $z = 1.5$ mm (black) and at $z = 4.0$ mm with the corresponding Gaussian fit (dashed red line) to determine the width of the particle beam.

Simulation

Simulated Particle-Beam Profiles and Beam Evolution

In our simulations, all particle-beams could be described using a Gaussian distribution. We used a Gaussian distribution as input and the particle-beam remained Gaussian-like throughout the simulations. Examples of 1D particle-beam profiles are shown in Figure 8.10. The example is shown for 42 nm PS spheres at an injector pressure of 1.8 mbar. The beam-profiles are shown as solid lines at 1.5 mm distance (black) and at 4.0 mm distance (blue) from the injector exit. The corresponding Gaussian distributions fits are shown as red dashed lines.

We determined the particle-beam focus position and width from a Gaussian beam evolution fit. Examples of simulated beam widths and the corresponding fits for all three particle sizes are shown in Figure 8.11. The beam width is determined as FWHM of the particle-beam at the detector positions from the simulations. The Gaussian beam evolution fit agrees well with our simulated beam evolution data for all sizes and injector pressures.

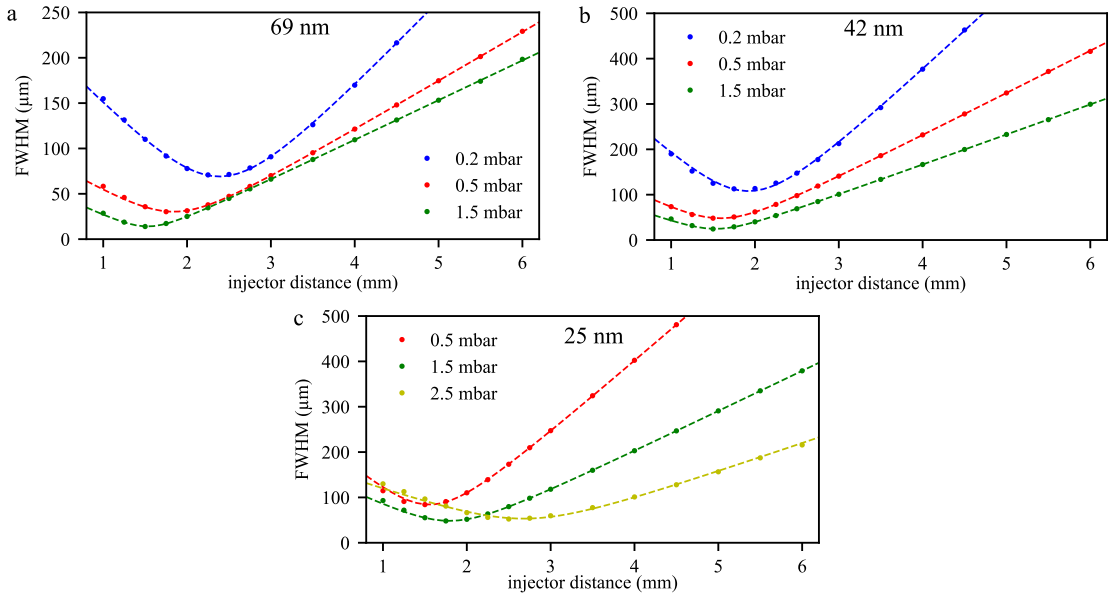

Figure 8.11: Simulated particle-beam evolution curves for (a) 69 nm, (b) 42 nm and (c) 25 nm PS spheres. The simulated beam widths are shown as dots and the dashed line correspond to a Gaussian beam evolution fit. (a) Particle-beam evolution curves for 69 nm PS spheres at 0.2 (blue), 0.5 (red) and 1.5 mbar (green) injector pressure. (b) Particle-beam evolution curves for 42 nm PS spheres at 0.2 (blue), 0.5 (red) and 1.5 mbar (green) injector pressure. (c) Particle-beam evolution curves for 25 nm PS spheres at 0.5 (red), 1.5 (green) and 2.5 mbar (yellow) injector pressure. All simulated beam widths fit well on a Gaussian beam evolution curve.

Particle-Gas Interactions after the ALS exit

To understand the focus position shift with increasing injector pressure, we looked at the simulated phase-space distributions $v_r(r)$ at the injector exit, $z = 0$ mm. The distributions are shown in Figure 8.12 a. The upper panel shows the distributions for 69 nm PS. At 0.4 mbar injector pressure, the distribution $v_r(r)$ is a half-ellipse with a maximum around $r = 0$ and $v_r = 0$. For $r > 0$, v_r is negative, i. e.we observed focusing behavior. At higher injector pressure a smaller $r-$space is occupied and at the same r-positions, particles had higher absolute v_r-values. For comparison, we included the grey line, which is similar in the low and high pressure case. For 25 nm, we observed a similar increase of the absolute values of the radial velocity with increasing injector pressure as shown in Figure 8.12 a lower panel. Using only the radial velocity distribution could not explain the focus shift towards the injector exit for 25 nm PS spheres. Therefore, we looked at the ratio of the radial and the longitudinal velocity, which indeed, explained the focus-shift as described in the main manuscript.

In Figure 8.12 b, we show the simulated longitudinal velocity increase with distance from the injector exit for 25 (red) and 69 nm (blue) PS spheres at 0.4 (solid lines) and 2.0 mbar (dashed lines) injector pressure. The flow field was extended up to 5 mm injector distance to include the acceleration of the particles as seen in the increase of v_z. At 5 mm, the curve is almost flat, indicating a small to negligible particle-gas interaction in this region. Especially for higher pressures it is important to extent the flow field after the injector exit to include the velocity changes, which determines the focus position, see main manuscript for details.

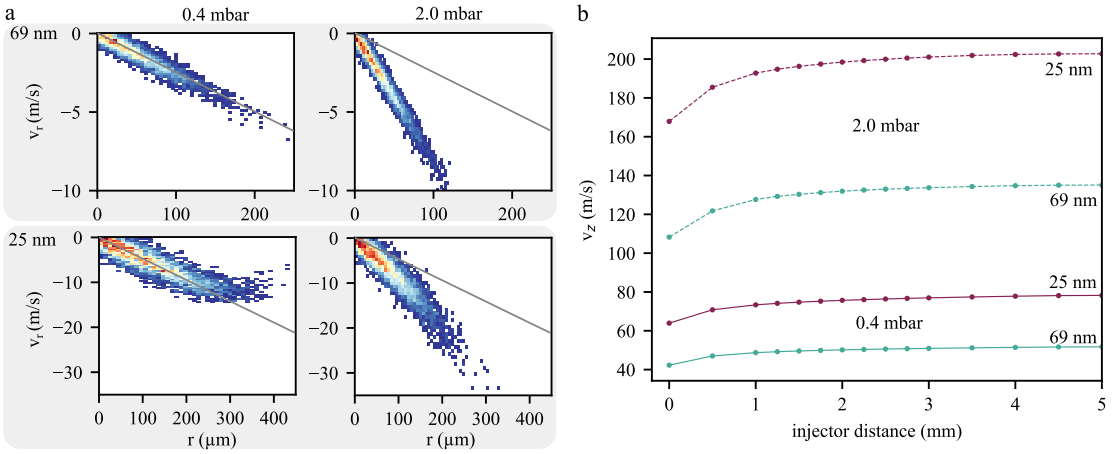

Figure 8.12: (a) Simulated phase-space distributions $v_r(r)$ at the injector exit, $z = 0$, for 69 nm PS spheres (upper panel) and 25 nm PS spheres (lower panel) at 0.4 mbar (left) and 2.0 mbar (right) injector pressure. (b) Simulated mean longitudinal velocity v_z depending on the injector distance for 25 nm and 69 nm PS spheres at 0.4 and 2.0 mbar injector pressure.

Bibliography

[1] M. P. Minitti, J. M. Budarz, A. Kirrander, J. S. Robinson, D. Ratner, T. J. Lane, D. Zhu, J. M. Glownia, M. Kozina, H. T. Lemke, M. Sikorski, Y. Feng, S. Nelson, K. Saita, B. Stankus, T. Northey, J. B. Hastings, and P. M. Weber. Imaging molecular motion: Femtosecond x-ray scattering of an electrocyclic chemical reaction. *Phys. Rev. Lett.*, 114(25):255501, 2015. doi: 10.1103/PhysRevLett.114.255501. URL `http://link.aps.org/doi/10.1103/PhysRevLett.114.255501`.

[2] H. Ihee, V. Lobastov, U. Gomez, B. Goodson, R. Srinivasan, C. Ruan, and A. H. Zewail. Direct imaging of transient molecular structures with ultrafast diffraction. *Science*, 291(5503): 458–462, January 2001. doi: 10.1126/science.291.5503.458. URL `https://www.science.org/doi/abs/10.1126/science.291.5503.458`.

[3] A. Barty, J. Küpper, and H. N. Chapman. Molecular imaging using x-ray free-electron lasers. *Annu. Rev. Phys. Chem.*, 64(1):415–435, April 2013. doi: 10.1146/annurev-physchem-032511-143708. URL `http://dx.doi.org/10.1146/annurev-physchem-032511-143708`.

[4] U. Kannan, L. Giribabu, and S. N. Jammalamadaka. Demagnetization field driven charge transport in a tio2 based dye sensitized solar cell. *Solar Energy*, 187:281–289, 2019. ISSN 0038-092X. doi: https://doi.org/10.1016/j.solener.2019.05.029. URL `https://www.sciencedirect.com/science/article/pii/S0038092X1930492X`.

[5] F.-Y. Kong, J.-W. Zhang, R.-F. Li, Z.-X. Wang, W.-J. Wang, and W. Wang. Unique roles of gold nanoparticles in drug delivery, targeting and imaging applications. *Molecules*, 22: 1445, 2017. doi: 10.3390/molecules22091445. URL `https://www.ncbi.nlm.nih.gov/pmc/articles/PMC6151763/`.

[6] While we appreciate the historic use of Ångström (Å) as a unit of length in crystallography, we point out that it is not a formal part of the International System of Units (SI) and that the International Committee for Weights and Measures officially discourages its use. Throughout this paper we use SI-prefixed derivatives of meter; 1 Å $= 10^{-10}$ m $= 0.1$ nm $= 100$ pm.

[7] R. Neutze, R. Wouts, D. van der Spoel, E. Weckert, and J. Hajdu. Potential for biomolecular imaging with femtosecond x-ray pulses. *Nature*, 406(6797):752–757, August 2000. doi: 10.1038/35021099. URL `http://dx.doi.org/10.1038/35021099`.

[8] K. J. Gaffney and H. N. Chapman. Imaging atomic structure and dynamics with ultrafast x-ray scattering. *Science*, 316(5830):1444–1448, 2007. doi: 10.1126/science.1135923. URL `http://www.sciencemag.org/content/316/5830/1444.abstract`.

[9] J. Hajdu. Single-molecule x-ray diffraction. *Current Opinion in Structural Biology*, 10 (5):569–573, 2000. ISSN 0959-440X. doi: 10.1016/S0959-440X(00)00133-0. URL `https://doi.org/10.1016/S0959-440X(00)00133-0`.

[10] C. Uetrecht and A. J. R. Heck. Modern biomolecular mass spectrometry and its role in studying virus structure, dynamics, and assembly. *Angew. Chem. Int. Ed.*, 50(36):8248–8262, 2011. doi: https://doi.org/10.1002/anie.201008120. URL https://onlinelibrary.wiley.com/doi/abs/10.1002/anie.201008120.

[11] L. E. Kay. Nmr studies of protein structure and dynamics. *Journal of Magnetic Resonance*, 173(2):193–207, 2005. ISSN 1090-7807. doi: https://doi.org/10.1016/j.jmr.2004.11.021. URL https://www.sciencedirect.com/science/article/pii/S1090780704003854.

[12] Y. Shi. A glimpse of structural biology through x-ray crystallography. *Cell*, 159(5):995 – 1014, 2014. ISSN 0092-8674. doi: 10.1016/j.cell.2014.10.051. URL http://www.sciencedirect.com/science/article/pii/S0092867414014238.

[13] K. M. Yip, N. Fischer, E. Paknia, A. Chari, and H. Stark. Atomic-resolution protein structure determination by cryo-em. *Nature*, 587(7832):157–161, 2020. doi: 10.1038/s41586-020-2833-4. URL https://doi.org/10.1038/s41586-020-2833-4.

[14] E. Callaway. The revolution will not be crystallized: a new method sweeps through structural biology. *Nature*, 525:172–174, 2015. doi: 10.1038/525172a. URL https://www.nature.com/news/the-revolution-will-not-be-crystallized-a-new-method-sweeps-through-structural-biology-1.18335.

[15] A. Merk, A. Bartesaghi, S. Banerjee, V. Falconieri, P. Rao, M. I. Davis, R. Pragani, M. B. Boxer, L. A. Earl, J. L. S. Milne, and S. Subramaniam. Breaking cryo-EM resolution barriers to facilitate drug discovery. *Cell*, 165:1698–1707, 2016. doi: 10.1016/j.cell.2016.05.040. URL https://doi.org/10.1016/j.cell.2016.05.040.

[16] J. Arthur, G. Materlik, R. Tatchyn, and H. Winick. The LCLS: A fourth generation light source using the SLAC linac. *Rev. Sci. Instrum.*, 66(2):1987, 1995. doi: 10.1063/1.1145778. URL http://link.aip.org/link/RSINAK/v66/i2/p1987/s1&Agg=doi.

[17] W. Decking, S. Abeghyan, P. Abramian, A. Abramsky, A. Aguirre, C. Albrecht, P. Alou, M. Altarelli, P. Altmann, K. Amyan, V. Anashin, E. Apostolov, K. Appel, D. Auguste, V. Ayvazyan, S. Baark, F. Babies, N. Baboi, P. Bak, V. Balandin, R. Baldinger, B. Baranasic, S. Barbanotti, O. Belikov, V. Belokurov, L. Belova, V. Belyakov, S. Berry, M. Bertucci, B. Beutner, A. Block, M. Blöcher, T. Böckmann, C. Bohm, M. Böhnert, V. Bondar, E. Bondarchuk, M. Bonezzi, P. Borowiec, C. Bösch, U. Bösenberg, A. Bosotti, R. Böspflug, M. Bousonville, E. Boyd, Y. Bozhko, A. Brand, J. Branlard, S. Briechle, F. Brinker, S. Brinker, R. Brinkmann, S. Brockhauser, O. Brovko, H. Brück, A. Brüdgam, L. Butkowski, T. Büttner, J. Calero, E. Castro-Carballo, G. Cattalanotto, J. Charrier, J. Chen, A. Cherepenko, V. Cheskidov, M. Chiodini, A. Chong, S. Choroba, M. Chorowski, D. Churanov, W. Cichalewski, M. Clausen, W. Clement, C. Cloué, J. A. Cobos, N. Coppola, S. Cunis, K. Czuba, M. Czwalinna, B. D'Almagne, J. Dammann, H. Danared, A. de Zubiaurre Wagner, A. Delfs, T. Delfs, F. Dietrich, T. Dietrich, M. Dohlus, M. Dommach, A. Donat, X. Dong, N. Doynikov, M. Dressel, M. Duda, P. Duda, H. Eckoldt, W. Ehsan, J. Eidam, F. Eints, C. Engling, U. Englisch, A. Ermakov, K. Escherich, J. Eschke, E. Saldin, M. Faesing, A. Fallou, M. Felber, M. Fenner, B. Fernandes, J. M. Fernández, S. Feuker, K. Filippakopoulos, K. Floettmann, V. Fogel, M. Fontaine, A. Francés, I. F. Martin, W. Freund, T. Freyermuth, M. Friedland, L. Fröhlich, M. Fusetti, J. Fydrych, A. Gallas, O. García, L. Garcia-Tabares, G. Geloni, N. Gerasimova, C. Gerth, P. Geßler, V. Gharibyan, M. Gloor, J. Głowinkowski, A. Goessel,

Z. Gołębiewski, N. Golubeva, W. Grabowski, W. Graeff, A. Grebentsov, M. Grecki, T. Grevsmuehl, M. Gross, U. Grosse-Wortmann, J. Grünert, S. Grunewald, P. Grzegory, G. Feng, H. Guler, G. Gusev, J. L. Gutierrez, L. Hagge, M. Hamberg, R. Hanneken, E. Harms, I. Hartl, A. Hauberg, S. Hauf, J. Hauschildt, J. Hauser, J. Havlicek, A. Hedqvist, N. Heidbrook, F. Hellberg, D. Henning, O. Hensler, T. Hermann, A. Hidvégi, M. Hierholzer, H. Hintz, F. Hoffmann, M. Hoffmann, M. Hoffmann, Y. Holler, M. Hüning, A. Ignatenko, M. Ilchen, A. Iluk, J. Iversen, M. Izquierdo, L. Jachmann, N. Jardon, U. Jastrow, K. Jensch, J. Jensen, M. Jeżabek, M. Jidda, H. Jin, N. Johansson, R. Jonas, W. Kaabi, D. Kaefer, R. Kammering, H. Kapitza, S. Karabekyan, S. Karstensen, K. Kasprzak, V. Katalev, D. Keese, B. Keil, M. Kholopov, M. Killenberger, B. Kitaev, Y. Klimchenko, R. Klos, L. Knebel, A. Koch, M. Koepke, S. Köhler, W. Köhler, N. Kohlstrunk, Z. Konopkova, A. Konstantinov, W. Kook, W. Koprek, M. Körfer, O. Korth, A. Kosarev, K. Kosiński, D. Kostin, Y. Kot, A. Kotarba, T. Kozak, V. Kozak, R. Kramert, M. Krasilnikov, A. Krasnov, B. Krause, L. Kravchuk, O. Krebs, R. Kretschmer, J. Kreutzkamp, O. Kröplin, K. Krzysik, G. Kube, H. Kuehn, N. Kujala, V. Kulikov, V. Kuzminych, D. La Civita, M. Lacroix, T. Lamb, A. Lancetov, M. Larsson, D. Le Pinvidic, S. Lederer, T. Lensch, D. Lenz, A. Leuschner, F. Levenhagen, Y. Li, J. Liebing, L. Lilje, T. Limberg, D. Lipka, B. List, J. Liu, S. Liu, B. Lorbeer, J. Lorkiewicz, H. H. Lu, F. Ludwig, K. Machau, W. Maciocha, C. Madec, C. Magueur, C. Maiano, I. Maksimova, K. Malcher, T. Maltezopoulos, E. Mamoshkina, B. Manschwetus, F. Marcellini, G. Marinkovic, T. Martinez, H. Martirosyan, W. Maschmann, M. Maslov, A. Matheisen, U. Mavric, J. Meißner, K. Meissner, M. Messerschmidt, N. Meyners, G. Michalski, P. Michelato, N. Mildner, M. Moe, F. Moglia, C. Mohr, S. Mohr, W. Möller, M. Mommerz, L. Monaco, C. Montiel, M. Moretti, I. Morozov, P. Morozov, and D. Mross. A MHz-repetition-rate hard X-ray free-electron laser driven by a superconducting linear accelerator. *Nat. Photon.*, 14(6):391–397, June 2020. ISSN 1749-4893. doi: 10.1038/s41566-020-0607-z. URL `https://doi.org/10.1038/s41566-020-0607-z`.

[18] J. C. H. Spence. XFELs for structure and dynamics in biology. *IUCrJ*, 4(4):322–339, Jul 2017. doi: 10.1107/S2052252517005760. URL `https://doi.org/10.1107/S2052252517005760`.

[19] H. N. Chapman, C. Caleman, and N. Timneanu. Diffraction before destruction. *Phil. Trans. R. Soc. B*, 369(1647):20130313, 2014. ISSN 0962-8436. doi: 10.1098/rstb.2013.0313. URL `https://doi.org/10.1098/rstb.2013.0313`.

[20] H. N. Chapman, P. Fromme, A. Barty, T. A. White, R. A. Kirian, A. Aquila, M. S. Hunter, J. Schulz, D. P. Deponte, U. Weierstall, R. B. Doak, F. R. N. C. Maia, A. V. Martin, I. Schlichting, L. Lomb, N. Coppola, R. L. Shoeman, S. W. Epp, R. Hartmann, D. Rolles, A. Rudenko, L. Foucar, N. Kimmel, G. Weidenspointner, P. Holl, M. Liang, M. Barthelmess, C. Caleman, S. Boutet, M. J. Bogan, J. Krzywinski, C. Bostedt, S. Bajt, L. Gumprecht, B. Rudek, B. Erk, C. Schmidt, A. Hömke, C. Reich, D. Pietschner, L. Strüder, G. Hauser, H. Gorke, J. Ullrich, S. Herrmann, G. Schaller, F. Schopper, H. Soltau, K.-U. Kühnel, M. Messerschmidt, J. D. Bozek, S. P. Hau-Riege, M. Frank, C. Y. Hampton, R. G. Sierra, D. Starodub, G. J. Williams, J. Hajdu, N. Timneanu, M. M. Seibert, J. Andreasson, A. Rocker, O. Jönsson, M. Svenda, S. Stern, K. Nass, R. Andritschke, C.-D. Schröter, F. Krasniqi, M. Bott, K. E. Schmidt, X. Wang, I. Grotjohann, J. M. Holton, T. R. M. Barends, R. Neutze, S. Marchesini, R. Fromme, S. Schorb, D. Rupp, M. Adolph, T. Gorkhover, I. Andersson, H. Hirsemann, G. Potdevin, H. Graafsma, B. Nilsson, and J. C. H. Spence. Femtosecond x-ray protein nanocrystallography. *Nature*, 470(7332):73, Feb 2011. doi: 10.1038/nature09750. URL `http://www.nature.com/nature/journal/v470/n7332/full/nature09750.html`.

[21] S. Boutet, L. Lomb, G. J. Williams, T. R. M. Barends, A. Aquila, R. B. Doak, U. Weierstall, D. P. DePonte, J. Steinbrener, R. L. Shoeman, M. Messerschmidt, A. Barty, T. A. White, S. Kassemeyer, R. A. Kirian, M. M. Seibert, P. A. Montanez, C. Kenney, R. Herbst, P. Hart, J. Pines, G. Haller, S. M. Gruner, H. T. Philipp, M. W. Tate, M. Hromalik, L. J. Koerner, N. van Bakel, J. Morse, W. Ghonsalves, D. Arnlund, M. J. Bogan, C. Caleman, R. Fromme, C. Y. Hampton, M. S. Hunter, L. C. Johansson, G. Katona, C. Kupitz, M. Liang, A. V. Martin, K. Nass, L. Redecke, F. Stellato, N. Timneanu, D. Wang, N. A. Zatsepin, D. Schafer, J. Defever, R. Neutze, P. Fromme, J. C. H. Spence, H. N. Chapman, and I. Schlichting. High-resolution protein structure determination by serial femtosecond crystallography. *Science*, 337(6092):362–364, 2012. doi: 10.1126/science.1217737. URL `http://www.sciencemag.org/content/337/6092/362.abstract`.

[22] A. Barty, C. Caleman, A. Aquila, N. Timneanu, L. Lomb, T. A. White, J. Andreasson, D. Arnlund, S. Bajt, T. R. M. Barends, M. Barthelmess, M. J. Bogan, C. Bostedt, J. D. Bozek, R. Coffee, N. Coppola, J. Davidsson, D. P. Deponte, R. B. Doak, T. Ekeberg, V. Elser, S. W. Epp, B. Erk, H. Fleckenstein, L. Foucar, P. Fromme, H. Graafsma, L. Gumprecht, J. Hajdu, C. Y. Hampton, R. Hartmann, A. Hartmann, G. Hauser, H. Hirsemann, P. Holl, M. S. Hunter, L. Johansson, S. Kassemeyer, N. Kimmel, R. A. Kirian, M. Liang, F. R. N. C. Maia, E. Malmerberg, S. Marchesini, A. V. Martin, K. Nass, R. Neutze, C. Reich, D. Rolles, B. Rudek, A. Rudenko, H. Scott, I. Schlichting, J. Schulz, M. M. Seibert, R. L. Shoeman, R. G. Sierra, H. Soltau, J. C. H. Spence, F. Stellato, S. Stern, L. Strüder, J. H. Ullrich, X. Wang, G. Weidenspointner, U. Weierstall, C. B. Wunderer, and H. N. Chapman. Self-terminating diffraction gates femtosecond x-ray nanocrystallography measurements. *Nat. Photon.*, 6(1): 35–40, 2012. doi: 10.1038/nphoton.2011.297. URL `http://www.nature.com/doifinder/10.1038/nphoton.2011.297`.

[23] M. O. Wiedorn, S. Awel, A. J. Morgan, K. Ayyer, Y. Gevorkov, H. Fleckenstein, N. Roth, L. Adriano, R. Bean, K. R. Beyerlein, J. Chen, J. Coe, F. Cruz-Mazo, T. Ekeberg, R. Graceffa, M. Heymann, D. A. Horke, J. Knoška, V. Mariani, R. Nazari, D. Oberthür, A. K. Samanta, R. G. Sierra, C. A. Stan, O. Yefanov, D. Rompotis, J. Correa, B. Erk, R. Treusch, J. Schulz, B. G. Hogue, A. M. Gañán-Calvo, P. Fromme, J. Küpper, A. V. Rode, S. Bajt, R. A. Kirian, and H. N. Chapman. Rapid sample delivery for megahertz serial crystallography at x-ray FELs. *IUCrJ*, 5(5):574–584, September 2018. doi: 10.1107/S2052252518008369. URL `https://doi.org/10.1107/S2052252518008369`.

[24] A. M. Orville. Recent results in time resolved serial femtosecond crystallography at xfels. *Current Opinion in Structural Biology*, 65:193–208, 2020. ISSN 0959-440X. doi: https://doi.org/10.1016/j.sbi.2020.08.011. URL `https://www.sciencedirect.com/science/article/pii/S0959440X20301482`. Catalysis and Regulation, Protein Nucleic Acid Interaction.

[25] M. J. Bogan, W. H. Benner, S. Boutet, U. Rohner, M. Frank, A. Barty, M. M. Seibert, F. Maia, S. Marchesini, S. Bajt, B. Woods, V. Riot, S. P. Hau-Riege, M. Svenda, E. Marklund, E. Spiller, J. Hajdu, and H. N. Chapman. Single particle x-ray diffractive imaging. *Nano Lett.*, 8(1):310–316, January 2008. doi: 10.1021/nl072728k. URL `http://pubs.acs.org/cgi-bin/abstract.cgi/nalefd/2008/8/i01/abs/nl072728k.html`.

[26] A. Aquila, A. Barty, C. Bostedt, S. Boutet, G. Carini, D. DePonte, P. Drell, S. Doniach, K. H. Downing, T. Earnest, H. Elmlund, V. Elser, M. Gühr, J. Hajdu, J. Hastings, S. P. Hau-Riege, Z. Huang, E. E. Lattman, F. R. N. C. Maia, S. Marchesini, A. Ourmazd, C. Pellegrini, R. Santra, I. Schlichting, C. Schroer, J. C. H. Spence, I. A. Vartanyants,

S. Wakatsuki, W. I. Weis, and G. J. Williams. The linac coherent light source single particle imaging road map. *Struct. Dyn.*, 2(4):041701, July 2015. doi: 10.1063/1.4918726. URL https://doi.org/10.1063/1.4918726.

[27] I. Poudyal, M. Schmidt, and P. Schwander. Single-particle imaging by x-ray free-electron lasers—how many snapshots are needed? *Structural Dynamics*, 7(2):024102, 2020. doi: 10.1063/1.5144516. URL https://doi.org/10.1063/1.5144516.

[28] T. Ekeberg, M. Svenda, C. Abergel, F. R. N. C. Maia, V. Seltzer, J.-M. Claverie, M. Hantke, O. Jönsson, C. Nettelblad, G. van der Schot, M. Liang, D. P. Deponte, A. Barty, M. M. Seibert, B. Iwan, I. Andersson, N. D. Loh, A. V. Martin, H. Chapman, C. Bostedt, J. D. Bozek, K. R. Ferguson, J. Krzywinski, S. W. Epp, D. Rolles, A. Rudenko, R. Hartmann, N. Kimmel, and J. Hajdu. Three-dimensional reconstruction of the giant mimivirus particle with an x-ray free-electron laser. *Phys. Rev. Lett.*, 114(9):098102, March 2015. doi: 10.1103/PhysRevLett.114.098102. URL http://dx.doi.org/10.1103/PhysRevLett.114.098102.

[29] I. V. Lundholm, J. A. Sellberg, T. Ekeberg, M. F. Hantke, K. Okamoto, G. van der Schot, J. Andreasson, A. Barty, J. Bielecki, P. Bruza, M. Bucher, S. Carron, B. J. Daurer, K. Ferguson, D. Hasse, J. Krzywinski, D. S. D. Larsson, A. Morgan, K. Mühlig, M. Müller, C. Nettelblad, A. Pietrini, H. K. N. Reddy, D. Rupp, M. Sauppe, M. Seibert, M. Svenda, M. Swiggers, N. Timneanu, A. Ulmer, D. Westphal, G. Williams, A. Zani, G. Faigel, H. N. Chapman, T. Möller, C. Bostedt, J. Hajdu, T. Gorkhover, and F. R. N. C. Maia. Considerations for three-dimensional image reconstruction from experimental data in coherent diffractive imaging. *IUCrJ*, 5(5):531–541, 2018. doi: 10.1107/S2052252518010047. URL https://doi.org/10.1107/S2052252518010047.

[30] M. Rose, S. Bobkov, K. Ayyer, R. P. Kurta, D. Dzhigaev, Y. Y. Kim, A. J. Morgan, C. H. Yoon, D. Westphal, J. Bielecki, J. A. Sellberg, G. Williams, F. R. Maia, O. M. Yefanov, V. Ilyin, A. P. Mancuso, H. N. Chapman, B. G. Hogue, A. Aquila, A. Barty, and I. A. Vartanyants. Single-particle imaging without symmetry constraints at an x-ray free-electron laser. *IUCrJ*, 5(6):727–736, 2018. doi: 10.1107/S205225251801120X. URL https://doi.org/10.1107/S205225251801120X.

[31] P. J. Ho, B. J. Daurer, M. F. Hantke, J. Bielecki, A. Al Haddad, M. Bucher, G. Doumy, K. R. Ferguson, L. Flückiger, T. Gorkhover, B. Iwan, C. Knight, S. Moeller, T. Osipov, D. Ray, S. H. Southworth, M. Svenda, N. Timneanu, A. Ulmer, P. Walter, J. Hajdu, L. Young, F. R. N. C. Maia, and C. Bostedt. The role of transient resonances for ultra-fast imaging of single sucrose nanoclusters. *Nat. Commun.*, 11(1):167, Jan 2020. ISSN 2041-1723. doi: 10.1038/s41467-019-13905-9. URL https://doi.org/10.1038/s41467-019-13905-9.

[32] K. Ayyer, P. L. Xavier, J. Bielecki, Z. Shen, B. J. Daurer, A. K. Samanta, S. Awel, R. Bean, A. Barty, M. Bergemann, T. Ekeberg, A. D. Estillore, H. Fangohr, K. Giewekemeyer, M. S. Hunter, M. Karnevskiy, R. A. Kirian, H. Kirkwood, Y. Kim, J. Koliyadu, H. Lange, R. Letrun, J. Lübke, T. Michelat, A. J. Morgan, N. Roth, T. Sato, M. Sikorski, F. Schulz, J. C. H. Spence, P. Vagovic, T. Wollweber, L. Worbs, O. Yefanov, Y. Zhuang, F. R. N. C. Maia, D. A. Horke, J. Küpper, N. D. Loh, A. P. Mancuso, and H. N. Chapman. 3D diffractive imaging of nanoparticle ensembles using an x-ray laser. *Optica*, 8(1):15–23, Jan 2021. doi: 10.1364/OPTICA.410851. URL http://www.osapublishing.org/optica/abstract.cfm?URI=optica-8-1-15.

[33] T. Ekeberg, D. Assalauova, J. Bielecki, R. Boll, B. J. Daurer, L. A. Eichacker, L. E. Franken, D. E. Galli, L. Gelisio, L. Gumprecht, L. H. Gunn, J. Hajdu, R. Hartmann, D. Hasse,

A. Ignatenko, J. Koliyadu, O. Kulyk, R. Kurta, M. Kuster, W. Lugmayr, J. Lübke, A. P. Mancuso, T. Mazza, C. Nettelblad, Y. Ovcharenko, D. E. Rivas, M. Rose, A. K. Samanta, P. Schmidt, E. Sobolev, N. Timneanu, S. Usenko, D. Westphal, T. Wollweber, L. Worbs, P. L. Xavier, H. Yousef, K. Ayyer, H. N. Chapman, J. A. Sellberg, C. Seuring, I. A. Vartanyants, J. Küpper, M. Meyer, and F. R. Maia. Observation of a single protein by ultrafast x-ray diffraction. *bioRxiv*, 2022. doi: 10.1101/2022.03.09.483477. URL `https://www.biorxiv.org/content/early/2022/03/12/2022.03.09.483477`.

[34] J. Bielecki, F. R. N. C. Maia, and A. P. Mancuso. Perspectives on single particle imaging with x rays at the advent of high repetition rate x-ray free electron laser sources. *Structural Dynamics*, 7(4):040901, 2020. doi: 10.1063/4.0000024. URL `https://doi.org/10.1063/4.0000024`.

[35] J. E, M. Stransky, Z. Jurek, C. Fortmann-Grote, L. Juha, R. Santra, B. Ziaja, and A. P. Mancuso. Effects of radiation damage and inelastic scattering on single-particle imaging of hydrated proteins with an x-ray free-electron laser. *Sci. Rep.*, 11(1):17976, 2021. doi: 10.1038/s41598-021-97142-5. URL `https://doi.org/10.1038/s41598-021-97142-5`.

[36] J. Peck, L. A. Gonzalez, L. R. Williams, W. Xu, P. L. Croteau, M. T. Timko, J. T. Jayne, D. R. Worsnop, R. C. Miake-Lye, and K. A. Smith. Development of an aerosol mass spectrometer lens system for pm2.5. *Aerosol Sci. Techn.*, 50(8):781–789, 2016. doi: 10.1080/02786826.2016.1190444. URL `https://doi.org/10.1080/02786826.2016.1190444`.

[37] K.-S. Lee, S.-W. Cho, and D. Lee. Development and experimental evaluation of aerodynamic lens as an aerosol inlet of single particle mass spectrometry. *J. Aerosol. Sci.*, 39(4):287–304, April 2008. doi: 10.1016/j.jaerosci.2007.10.011. URL `http://dx.doi.org/10.1016/j.jaerosci.2007.10.011`.

[38] R. A. Kirian, S. Awel, N. Eckerskorn, H. Fleckenstein, M. Wiedorn, L. Adriano, S. Bajt, M. Barthelmess, R. Bean, K. R. Beyerlein, L. M. G. Chavas, M. Domaracky, M. Heymann, D. A. Horke, J. Knoska, M. Metz, A. Morgan, D. Oberthuer, N. Roth, T. Sato, P. L. Xavier, O. Yefanov, A. V. Rode, J. Küpper, and H. N. Chapman. Simple convergent-nozzle aerosol injector for single-particle diffractive imaging with x-ray free-electron lasers. *Struct. Dyn.*, 2(4):041717, July 2015. doi: 10.1063/1.4922648. URL `http://dx.doi.org/10.1063/1.4922648`.

[39] D. P. DePonte, U. Weierstall, K. Schmidt, J. Warner, D. Starodub, J. C. H. Spence, and R. B. Doak. Gas dynamic virtual nozzle for generation of microscopic droplet streams. *J. Phys. D*, 41(19):195505, 2008. doi: 10.1088/0022-3727/41/19/195505. URL `http://iopscience.iop.org/0022-3727/41/19/195505`.

[40] M. Dole, L. Mack, R. Hines, R. Mobley, L. Ferguson, and M. d. Alice. Molecular beams of macroions. *J. Chem. Phys.*, 49(5):2240–2249, 1968. URL `http://dx.doi.org/10.1063/1.1670391`.

[41] M. M. Seibert, T. Ekeberg, F. R. N. C. Maia, M. Svenda, J. Andreasson, O. Jönsson, D. Odić, B. Iwan, A. Rocker, D. Westphal, M. Hantke, D. P. Deponte, A. Barty, J. Schulz, L. Gumprecht, N. Coppola, A. Aquila, M. Liang, T. A. White, A. Martin, C. Caleman, S. Stern, C. Abergel, V. Seltzer, J.-M. Claverie, C. Bostedt, J. D. Bozek, S. Boutet, A. A. Miahnahri, M. Messerschmidt, J. Krzywinski, G. Williams, K. O. Hodgson, M. J. Bogan, C. Y. Hampton, R. G. Sierra, D. Starodub, I. Andersson, S. Bajt, M. Barthelmess, J. C. H. Spence, P. Fromme, U. Weierstall, R. Kirian, M. Hunter, R. B. Doak, S. Marchesini, S. P. Hau-Riege, M. Frank, R. L. Shoeman, L. Lomb, S. W. Epp, R. Hartmann, D. Rolles, A. Rudenko, C. Schmidt, L. Foucar, N. Kimmel, P. Holl, B. Rudek, B. Erk, A. Hömke, C. Reich, D. Pietschner,

G. Weidenspointner, L. Strüder, G. Hauser, H. Gorke, J. Ullrich, I. Schlichting, S. Herrmann, G. Schaller, F. Schopper, H. Soltau, K.-U. Kühnel, R. Andritschke, C.-D. Schröter, F. Krasniqi, M. Bott, S. Schorb, D. Rupp, M. Adolph, T. Gorkhover, H. Hirsemann, G. Potdevin, H. Graafsma, B. Nilsson, H. N. Chapman, and J. Hajdu. Single mimivirus particles intercepted and imaged with an X-ray laser. *Nature*, 470(7332):78, 2011. doi: 10.1038/nature09748. URL http://www.nature.com/nature/journal/v470/n7332/full/nature09748.html.

[42] M. F. Hantke, D. Hasse, M. R. N. C, T. Ekeberg, K. John, M. Svenda, N. D. Loh, A. V. Martin, N. Timneanu, L. S. D, van der SchotGijs, G. H. Carlsson, M. Ingelman, J. Andreasson, D. Westphal, M. Liang, F. Stellato, D. P. DePonte, R. Hartmann, N. Kimmel, R. A. Kirian, M. M. Seibert, K. Mühlig, S. Schorb, K. Ferguson, C. Bostedt, S. Carron, J. D. Bozek, D. Rolles, A. Rudenko, S. Epp, H. N. Chapman, A. Barty, J. Hajdu, and I. Andersson. High-throughput imaging of heterogeneous cell organelles with an x-ray laser. *Nat. Photon.*, 8(12):943–949, 2014. doi: doi:10.1038/nphoton.2014.270. URL http://www.nature.com/nphoton/journal/v8/n12/full/nphoton.2014.270.html.

[43] A. D. Rath, N. Timneanu, F. R. N. C. Maia, J. Bielecki, H. Fleckenstein, B. Iwan, M. Svenda, D. Hasse, G. Carlsson, D. Westphal, K. Mühlig, M. Hantke, T. Ekeberg, M. M. Seibert, A. Zani, M. Liang, F. Stellato, R. Kirian, R. Bean, A. Barty, L. Galli, K. Nass, M. Barthelmess, A. Aquila, S. Toleikis, R. Treusch, S. Roling, M. Wöstmann, H. Zacharias, H. N. Chapman, S. Bajt, D. DePonte, J. Hajdu, and J. Andreasson. Explosion dynamics of sucrose nanospheres monitored by time of flight spectrometry and coherent diffractive imaging at the split-and-delay beam line of the flash soft x-ray laser. *Opt. Exp.*, 22(23):28914–28925, Nov 2014. doi: 10.1364/OE.22.028914. URL http://opg.optica.org/oe/abstract.cfm?URI=oe-22-23-28914.

[44] G. van der Schot, M. Svenda, F. R. N. C. Maia, M. Hantke, D. P. DePonte, M. M. Seibert, A. Aquila, J. Schulz, R. Kirian, M. Liang, F. Stellato, B. Iwan, J. Andreasson, N. Timneanu, D. Westphal, F. N. Almeida, D. Odic, D. Hasse, G. H. Carlsson, D. S. D. Larsson, A. Barty, A. V. Martin, S. Schorb, C. Bostedt, J. D. Bozek, D. Rolles, A. Rudenko, S. Epp, L. Foucar, B. Rudek, R. Hartmann, N. Kimmel, P. Holl, L. Englert, N.-T. Duane Loh, H. N. Chapman, I. Andersson, J. Hajdu, and T. Ekeberg. Imaging single cells in a beam of live cyanobacteria with an x-ray laser. *Nat. Commun.*, 6:5704, February 2015. URL http://dx.doi.org/10.1038/ncomms6704.

[45] N. Roth, D. Horke, J. Lübke, A. K. Samanta, A. D. Estillore, L. Worbs, N. Pohlman, K. Ayyer, A. Morgan, H. Fleckenstein, M. Domaracky, B. Erk, C. Passow, J. Correa, O. Yefanov, A. Barty, M. Prasciolu, S. Bajt, R. Kirian, H. Chapman, and J. Küpper. New aerodynamic lens injector for single particle diffractive imaging. *Rev. Sci. Instrum.*, 2021. submitted.

[46] N. Roth, S. Awel, D. A. Horke, and J. Küpper. Optimizing aerodynamic lenses for single-particle imaging. *J. Aerosol. Sci.*, 124:17–29, 2018. ISSN 0021-8502. doi: 10.1016/j.jaerosci.2018.06.010. URL http://www.sciencedirect.com/science/article/pii/S0021850217304652.

[47] Y. Zhuang, S. Awel, A. Barty, R. Bean, J. Bielecki, M. Bergemann, B. J. Daurer, T. Ekeberg, A. D. Estillore, H. Fangohr, K. Giewekemeyer, M. S. Hunter, M. Karnevskiy, R. A. Kirian, H. Kirkwood, Y. Kim, J. Koliyadu, H. Lange, R. Letrun, J. Lübke, A. Mall, T. Michelat, A. J. Morgan, N. Roth, A. K. Samanta, T. Sato, Z. Shen, M. Sikorski, F. Schulz, J. C. H. Spence, P. Vagovic, T. Wollweber, L. Worbs, P. L. Xavier, O. Yefanov, F. R. N. C. Maia, D. A. Horke, J. Küpper, N. D. Loh, A. P. Mancuso, H. N. Chapman, and K. Ayyer. Unsupervised learning approaches to characterizing heterogeneous samples using x-ray single-particle imaging. *IUCrJ*,

9(2):204–214, Mar 2022. doi: 10.1107/S2052252521012707. URL https://doi.org/10.1107/S2052252521012707.

[48] Y.-P. Chang, D. A. Horke, S. Trippel, and J. Küpper. Spatially-controlled complex molecules and their applications. *Int. Rev. Phys. Chem.*, 34:557–590, 2015. doi: 10.1080/0144235X.2015.1077838. URL https://dx.doi.org/10.1080/0144235X.2015.1077838.

[49] S. Trippel, Y.-P. Chang, S. Stern, T. Mullins, L. Holmegaard, and J. Küpper. Spatial separation of state- and size-selected neutral clusters. *Phys. Rev. A*, 86:033202, September 2012. doi: 10.1103/PhysRevA.86.033202. URL http://pra.aps.org/abstract/PRA/v86/i3/e033202.

[50] M. Johny, J. Onvlee, T. Kierspel, H. Bieker, S. Trippel, and J. Küpper. Spatial separation of pyrrole and pyrrole-water clusters. *Chem. Phys. Lett.*, 721:149–152, 2019. ISSN 0009-2614. doi: 10.1016/j.cplett.2019.01.052. URL https://doi.org/10.1016/j.cplett.2019.01.052.

[51] N. R. Hutzler, H.-I. Lu, and J. M. Doyle. The buffer gas beam: An intense, cold, and slow source for atoms and molecules. *Chem. Rev.*, 112(9):4803–4827, May 2012. doi: 10.1021/cr200362u. URL http://pubs.acs.org/doi/abs/10.1021/cr200362u.

[52] J. Piskorski, D. Patterson, S. Eibenberger, and J. M. Doyle. Cooling, spectroscopy and non-sticking of trans-stilbene and Nile Red. *Chem. Phys. Chem.*, 15:3800–3804, September 2014. doi: 10.1002/cphc.201402502. URL https://doi.org/10.1002/cphc.201402502.

[53] M. Z. Kamrath and T. R. Rizzo. Combining ion mobility and cryogenic spectroscopy for structural and analytical studies of biomolecular ions. *Acc. Chem. Res.*, 51(6):1487–1495, 2018. doi: 10.1021/acs.accounts.8b00133. URL https://pubs.acs.org/doi/abs/10.1021/acs.accounts.8b00133.

[54] A. K. Samanta, M. Amin, A. D. Estillore, N. Roth, L. Worbs, D. A. Horke, and J. Küpper. Controlled beams of shockfrozen, isolated, biological and artificial nanoparticles. *Struct. Dyn.*, 7:024304, 2020. doi: 10.1063/4.0000004. URL https://doi.org/10.1063/4.0000004.

[55] L. Worbs, J. Lübke, N. Roth, A. K. Samanta, D. A. Horke, and J. Küpper. Light-sheet imaging for the recording of transverse absolute density distributions of gas-phase particle-beams from nanoparticle injectors. *Opt. Exp.*, 27:36580–36586, March 2019. doi: 10.1364/OE.27.036580. URL https://doi.org/10.1364/OE.27.036580.

[56] L. Worbs, N. Roth, J. Lübke, A. D. Estillore, P. L. Xavier, A. K. Samanta, and J. Küpper. Optimizing the geometry of aerodynamic lens injectors for single-particle coherent diffractive imaging of gold nanoparticles. *J. Appl. Cryst.*, 54(6):1730–1737, December 2021. doi: 10.1107/S1600576721009973. URL https://arxiv.org/abs/2105.15084.

[57] L. Worbs, J. Lübke, A. D. Estillore, A. K. Samanta, and J. Küpper. Understanding the focusing behavior of small nanoparticles upon pressure changes. *J. Phys. Chem. C*, 2022. in preparation.

[58] L. Worbs, A. D. Estillore, A. K. Samanta, and J. Küpper. Toward cryogenically-cooled particle beams of small nanoparticles and proteins. *Rev. Sci. Instrum.*, 2022. in preparation.

[59] S. Awel, R. A. Kirian, N. Eckerskorn, M. Wiedorn, D. A. Horke, A. V. Rode, J. Küpper, and H. N. Chapman. Visualizing aerosol-particle injection for diffractive-imaging experiments. *Opt. Exp.*, 24(6):6507–6521, 2016. doi: 10.1364/OE.24.006507. URL http://dx.doi.org/10.1364/OE.24.006507.

[60] N. Teschmit, D. A. Horke, and J. Küpper. Spatially separating the conformers of a dipeptide. *Angew. Chem. Int. Ed.*, 57(42):13775–13779, October 2018. doi: 10.1002/anie.201807646. URL https://onlinelibrary.wiley.com/doi/abs/10.1002/anie.201807646.

[61] J. Bielecki, M. F. Hantke, B. J. Daurer, H. K. N. Reddy, D. Hasse, D. S. D. Larsson, L. H. Gunn, M. Svenda, A. Munke, J. A. Sellberg, L. Flueckiger, A. Pietrini, C. Nettelblad, I. Lundholm, G. Carlsson, K. Okamoto, N. Timneanu, D. Westphal, O. Kulyk, A. Higashiura, G. van der Schot, N.-T. D. Loh, T. E. Wysong, C. Bostedt, T. Gorkhover, B. Iwan, M. M. Seibert, T. Osipov, P. Walter, P. Hart, M. Bucher, A. Ulmer, D. Ray, G. Carini, K. R. Ferguson, I. Andersson, J. Andreasson, J. Hajdu, and F. R. N. C. Maia. Electrospray sample injection for single-particle imaging with x-ray lasers. *Science Advances*, 5:eaav8801, 2019. doi: 10.1126/sciadv.aav8801. URL https://advances.sciencemag.org/content/5/5/eaav8801.

[62] R. Nazari, S. Zaare, R. C. Alvarez, K. Karpos, T. Engelman, C. Madsen, G. Nelson, J. C. H. Spence, U. Weierstall, R. J. Adrian, and R. A. Kirian. 3d printing of gas-dynamic virtual nozzles and optical characterization of high-speed microjets. *Opt. Exp.*, 28(15):21749–21765, Jul 2020. doi: 10.1364/OE.390131. URL http://opg.optica.org/oe/abstract.cfm?URI=oe-28-15-21749.

[63] K. Mühlig, A. M. Gañán-Calvo, J. Andreasson, D. S. D. Larsson, J. Hajdu, and M. Svenda. Nanometre-sized droplets from a gas dynamic virtual nozzle. *J. Appl. Cryst.*, 52(4):800–808, Aug 2019. doi: 10.1107/S1600576719008318. URL https://doi.org/10.1107/S1600576719008318.

[64] L. He, S. Malerz, F. Trinter, S. Trippel, L. Tomaník, M. Belina, P. Slavíček, B. Winter, and J. Küpper. Specific versus non-specific solvent interactions of a biomolecule in water, 2022. URL https://arxiv.org/abs/2205.08217.

[65] V. Markmann, M. Dartsch, J. Valerio, L. Frenzel, I. Lokteva, M. Walther, F. Westermeier, G. Grübel, and F. Lehmkühler. Shear-induced ordering in liquid microjets seen by x-ray cross correlation analysis. *Struct. Dyn.*, 7(5):054901, 2020. doi: 10.1063/4.0000038. URL https://doi.org/10.1063/4.0000038.

[66] L. Konermann, E. Ahadi, A. D. Rodriguez, and S. Vahidi. Unraveling the mechanism of electrospray ionization. *Anal. Chem.*, 85(1):2–9, 2013. doi: 10.1021/ac302789c. URL https://doi.org/10.1021/ac302789c. PMID: 23134552.

[67] J. B. Fenn, M. Mann, C. K. Meng, S. F. Wong, and C. M. Whitehouse. Electrospray ionization for mass-spectrometry of large biomolecules. *Science*, 246:64–71, 1989. doi: 10.1126/science.2675315. URL https://doi.org/10.1126/science.2675315.

[68] A. C. Leney and A. J. R. Heck. Native mass spectrometry: What is in the name? *J. Am. Soc. Mass Spectrom.*, 28:5–13, January 2017. doi: 10.1007/s13361-016-1545-3. URL https://doi.org/10.1007/s13361-016-1545-3.

[69] M. Li, S. Guha, R. Zangmeister, M. J. Tarlov, and M. R. Zachariah. Method for determining the absolute number concentration of nanoparticles from electrospray sources. *Langmuir*, 27(24):14732–14739, 2011. doi: 10.1021/la202177s. URL https://doi.org/10.1021/la202177s. PMID: 22032424.

[70] P. Liu, P. J. Ziemann, D. B. Kittelson, and P. H. McMurry. Generating particle beams of controlled dimensions and divergence: I. theory of particle motion in aerodynamic lenses and

nozzle expansions. *Aerosol Sci. Techn.*, 22(3):293–313, 1995. doi: 10.1080/02786829408959748. URL http://dx.doi.org/10.1080/02786829408959748.

[71] P. Liu, P. J. Ziemann, D. B. Kittelson, and P. H. Mcmurry. Generating particle beams of controlled dimensions and divergence: Ii. experimental evaluation of particle motion in aerodynamic lenses and nozzle expansions. *Aerosol Sci. Tech.*, 22(3):314–324, 1995. doi: 10.1080/02786829408959749. URL http://www.tandfonline.com/doi/abs/10.1080/02786829408959749.

[72] X. Wang and P. H. McMurry. A design tool for aerodynamic lens systems. *Aerosol Sci. Technol.*, 40(5):320–334, 2006. doi: 10.1080/02786820600615063. URL http://dx.doi.org/10.1080/02786820600615063.

[73] R. A. Millikan. The isolation of an ion, a precision measurement of its charge, and the correction of Stokes's law. *Science*, 32(822):436–448, 1910. ISSN 0036-8075. doi: 10.1126/science.32.822.436. URL https://science.sciencemag.org/content/32/822/436.

[74] U. Even. The Even-Lavie valve as a source for high intensity supersonic beam. *Eur. Phys. J. Techn. Instrumen.*, 2(1):17, December 2015. doi: 10.1140/epjti/s40485-015-0027-5. URL https://doi.org/10.1140/epjti/s40485-015-0027-5.

[75] W. F. Tivol, A. Briegel, and G. J. Jensen. An improved cryogen for plunge freezing. *Microsc. Microanal.*, 14(5):375–379, 2008. doi: 10.1017/S1431927608080781. URL https://doi.org/10.1017/S1431927608080781.

[76] J. Dubochet, M. Adrian, J.-J. Chang, J.-C. Homo, J. Lepault, A. W. McDowall, and P. Schultz. Cryo-electron microscopy of vitrified specimens. *Q. Rev. Biophys.*, 21(2):129–228, 1988. doi: 10.1017/S0033583500004297. URL https://doi.org/10.1017/S0033583500004297.

[77] F. A. Barreda, C. Nicolas, J. B. Sirven, F. X. Ouf, J. L. Lacour, E. Robert, S. Benkoula, J. Yon, C. Miron, and O. Sublemontier. In-situ characterization of nanoparticle beams focused with an aerodynamic lens by laser-induced breakdown detection. *Sci. Rep.*, 5, 2015. doi: 10.1038/srep15696. URL https://doi.org/10.1038/srep15696.

[78] M. Davino, T. Saule, N. G. Helming, J. A. Powell, and C. Trallero-Herrero. Characterization of an aerosolized nanoparticle beam beyond the diffraction limit through strong field ionization. *Sci. Rep.*, 12(1):9277, 2022. doi: 10.1038/s41598-022-13466-w. URL https://doi.org/10.1038/s41598-022-13466-w.

[79] C. F. Bohren and D. R. Huffman. *Absorption and Scattering of Light by Small Particles*. John Wiley & Sons, 1998.

[80] M. F. Hantke, J. Bielecki, O. Kulyk, D. Westphal, D. S. D. Larsson, M. Svenda, H. K. N. Reddy, R. A. Kirian, J. Andreasson, J. Hajdu, and F. R. N. C. Maia. Rayleigh-scattering microscopy for tracking and sizing nanoparticles in focused aerosol beams. *IUCrJ*, 5(6):673–680, Nov 2018. doi: 10.1107/S2052252518010837. URL https://doi.org/10.1107/S2052252518010837.

[81] B. P. Marsh, N. Chada, R. R. Sanganna Gari, K. P. Sigdel, and G. M. King. The Hessian blob algorithm: Precise particle detection in atomic force microscopy imagery. *Sci. Rep.*, 8:978, 2018. doi: 10.1038/s41598-018-19379-x. URL https://doi.org/10.1038/s41598-018-19379-x.

[82] Comsol. Multiphysics 5.5, 2019. COMSOL Multiphysics v. 5.5. http://www.comsol.com. COMSOL AB, Stockholm, Sweden.

[83] T. O. Foundation. OpenFOAM | free CFD software, v2012 (20 12). Website, URL: https://openfoam.org/, Dec 2020. URL https://openfoam.org/.

[84] N. Roth, M. Amin, A. K. Samanta, and J. Küpper. Microscopic force for aerosol transport. *submitted*, 2020.

[85] A. Li and G. Ahmadi. Dispersion and deposition of spherical particles from point sources in a turbulent channel flow. *Aerosol Sci. Techn.*, 16(24):209–226, January 1992. doi: 10.1080/02786829208959550. URL http://www.tandfonline.com/doi/abs/10.1080/02786829208959550.

[86] S. Welker, M. Amin, and J. Küpper. CMInject: Python framework for the numerical simulation of nanoparticle injection pipelines. *Comp. Phys. Comm.*, 270:108138, 2022. ISSN 0010-4655. doi: 10.1016/j.cpc.2021.108138. URL https://www.sciencedirect.com/science/article/pii/S0010465521002502.

[87] M. J. Bogan, S. Boutet, H. N. Chapman, S. Marchesini, A. Barty, W. H. Benner, U. Rohner, M. Frank, S. P. Hau-Riege, S. Bajt, B. Woods, M. M. Seibert, B. Iwan, N. Timneanu, J. Hajdu, and J. Schulz. Aerosol imaging with a soft x-ray free electron laser. *Aerosol Sci. Techn.*, 44(3):i–vi, 2010. doi: 10.1080/02786820903485800. URL http://dx.doi.org/10.1080/02786820903485800.

[88] D. A. Horke, N. Roth, L. Worbs, and J. Küpper. Characterizing gas flow from aerosol particle injectors. *J. Appl. Phys.*, 121(12):123106, 2017. doi: 10.1063/1.4978914. URL http://dx.doi.org/10.1063/1.4978914.

[89] T. Kierspel, J. Wiese, T. Mullins, J. Robinson, A. Aquila, A. Barty, R. Bean, R. Boll, S. Boutet, P. Bucksbaum, H. N. Chapman, L. Christensen, A. Fry, M. Hunter, J. E. Koglin, M. Liang, V. Mariani, A. Morgan, A. Natan, V. Petrovic, D. Rolles, A. Rudenko, K. Schnorr, H. Stapelfeldt, S. Stern, J. Thøgersen, C. H. Yoon, F. Wang, S. Trippel, and J. Küpper. Strongly aligned molecules at free-electron lasers. *J. Phys. B*, 48(20):204002, 2015. doi: 10.1088/0953-4075/48/20/204002. URL https://doi.org/10.1088/0953-4075/48/20/204002.

[90] K. R. Beyerlein, L. Adriano, M. Heymann, R. Kirian, J. Knoska, F. Wilde, H. N. Chapman, and S. Bajt. Ceramic micro-injection molded nozzles for serial femtosecond crystallography sample delivery. *Rev. Sci. Instrum.*, 86(12):125104, December 2015. doi: 10.1063/1.4936843. URL http://dx.doi.org/10.1063/1.4936843.

[91] R. J. Bean, A. Aquila, L. Samoylova, and A. P. Mancuso. Design of the mirror optical systems for coherent diffractive imaging at the SPB/SFX instrument of the European XFEL. *Journal of Optics*, 18(7):074011, 2016. URL http://stacks.iop.org/2040-8986/18/i=7/a=074011.

[92] B. Deppe, G. Huber, C. Kränkel, and J. Küpper. High-intracavity-power thin-disk laser for alignment of molecules. *Opt. Exp.*, 23(22):28491, 2015. doi: 10.1364/OE.23.028491. URL http://opg.optica.org/oe/abstract.cfm?URI=oe-23-22-28491.

[93] H. N. Chapman, A. Barty, M. J. Bogan, S. Boutet, S. Frank, S. P. Hau-Riege, S. Marchesini, B. W. Woods, S. Bajt, W. H. Benner, L. W. A., E. Plönjes, M. Kuhlmann, R. Treusch, S. Düsterer, T. Tschentscher, J. R. Schneider, E. Spiller, T. Möller, C. Bostedt, M. Hoener, D. A. Shapiro, K. O. Hodgson, D. van der Spoel, F. Burmeister, M. Bergh, C. Caleman, G. Huldt, M. M. Seibert, F. R. N. C. Maia, R. W. Lee, A. Szöke, N. Timneanu, and J. Hajdu.

Femtosecond diffractive imaging with a soft-x-ray free-electron laser. *Nat. Phys.*, 2:839–843, 2006. doi: 10.1038/nphys461. URL http://dx.doi.org/10.1038/nphys461.

[94] W. H. Benner, M. J. Bogan, U. Rohner, S. Boutet, B. Woods, and M. Frank. Non-destructive characterization and alignment of aerodynamically focused particle beams using single particle charge detection. *J. Aerosol. Sci.*, 39(11):917–928, NOV 2008. doi: 10.1016/j.jaerosci.2008.05.008. URL https://doi.org/10.1016/j.jaerosci.2008.05.008.

[95] M. R. Canagaratna, J. T. Jayne, J. L. Jimenez, J. D. Allan, M. R. Alfarra, Q. Zhang, T. B. Onasch, F. Drewnick, H. Coe, A. Middlebrook, A. Delia, L. R. Williams, A. M. Trimborn, M. J. Northway, P. F. DeCarlo, C. E. Kolb, P. Davidovits, and D. R. Worsnop. Chemical and microphysical characterization of ambient aerosols with the aerodyne aerosol mass spectrometer. *Mass Spectrom. Rev.*, 26(2):185–222, 2007. doi: 10.1002/mas.20115. URL http://dx.doi.org/10.1002/mas.20115.

[96] G. Schmid and U. Simon. Gold nanoparticles: assembly and electrical properties in 1–3 dimensions. *Chem. Commun.*, pages 697–710, 2005. doi: 10.1039/B411696H. URL http://dx.doi.org/10.1039/B411696H.

[97] L. Dykman and N. Khlebtsov. Gold nanoparticles in biomedical applications: recent advances and perspectives. *Chem. Soc. Rev.*, 41(6):2256–2282, 2012. ISSN 1460-4744. doi: 10.1039/C1CS15166E. URL https://pubs.rsc.org/en/content/articlelanding/2012/cs/c1cs15166e.

[98] X. Wang and P. H. McMurry. An experimental study of nanoparticle focusing with aerodynamic lenses. *Int. J. Mass Spectrom.*, 258(1):30–36, 2006. doi: 10.1016/j.ijms.2006.06.008. URL http://www.sciencedirect.com/science/article/pii/S138738060600306X.

[99] J. F. De La Mora and P. Riesco-Chueca. Aerodynamic focusing of particles in a carrier gas. *J. Fluid Mech.*, 195:1–21, 1988. doi: 10.1017/S0022112088002307. URL https://doi.org/10.1017/S0022112088002307.

[100] S. Fuerstenau, A. Gomez, and J. F. de la Mora. Visualization of aerodynamically focused subsonic aerosol jets. *J. Aerosol Sci*, 25(1):165–173, 1994. doi: 10.1016/0021-8502(94)90188-0. URL https://doi.org/10.1016/0021-8502(94)90188-0.

[101] N.-T. D. Loh and V. Elser. Reconstruction algorithm for single-particle diffraction imaging experiments. *Phys. Rev. E*, 80:026705, August 2009. doi: 10.1103/PhysRevE.80.026705. URL http://link.aps.org/doi/10.1103/PhysRevE.80.026705.

[102] A. M. R. de Graff, M. J. Hazoglou, and K. A. Dill. Highly charged proteins: The achilles' heel of aging proteomes. *Structure*, 24(2):329–336, February 2016. doi: 10.1016/j.str.2015.11.006. URL https://doi.org/10.1016/j.str.2015.11.006.

[103] J. Lübke, N. Roth, L. Worbs, D. A. Horke, A. D. Estillore, A. K. Samanta, and J. Küpper. Charge-state distribution of aerosolized nanoparticles. *J. Phys. Chem. C*, 125(46):25794–25798, 2021. doi: 10.1021/acs.jpcc.1c06912. URL https://doi.org/10.1021/acs.jpcc.1c06912.

[104] L. Zhang, J. Shao, X. Chen, J. Zhang, and Q. Si. Design and evaluation of aerodynamic lens system for focusing sub-10 nm nanoparticles. *Appl. Phys. A*, 122(11):953, 2016. doi: 10.1007/s00339-016-0489-6. URL https://doi.org/10.1007/s00339-016-0489-6.

[105] K. Ayyer. Reference-enhanced x-ray single-particle imaging. *Optica*, 7(6):593–601, May 2020. doi: 10.1364/OPTICA.391373. URL http://opg.optica.org/optica/abstract.cfm?URI=optica-7-6-593.

[106] D.-H. Tsai, F. W. DelRio, A. M. Keene, K. M. Tyner, R. I. MacCuspie, T. J. Cho, M. R. Zachariah, and V. A. Hackley. Adsorption and conformation of serum albumin protein on gold nanoparticles investigated using dimensional measurements and in situ spectroscopic methods. *Langmuir*, 27(6):2464–2477, 2011. doi: 10.1021/la104124d. URL https://doi.org/10.1021/la104124d. PMID: 21341776.

[107] S. Chowdhury, V. Katta, and B. Chait. Electrospray ionization mass spectrometric peptide mapping: A rapid, sensitive technique for protein structure analysis. *Biochemical and Biophysical Research Communications*, 167(2):686–692, 1990. ISSN 0006-291X. doi: 10.1016/0006-291X(90)92080-J. URL https://www.sciencedirect.com/science/article/pii/0006291X9092080J.

[108] K.-H. Choi, K. Rahman, A. Khan, and D.-S. Kim. Cross-talk effect in electrostatic based capillary array nozzles. *Journal of Mechanical Science and Technology*, 25(12):3053–3062, 2011. doi: 10.1007/s12206-011-0903-0. URL https://doi.org/10.1007/s12206-011-0903-0.

[109] R. Bocanegra, D. Galán, M. Márquez, I. Loscertales, and A. Barrero. Multiple electrosprays emitted from an array of holes. *J. Aerosol. Sci.*, 36(12):1387–1399, 2005. ISSN 0021-8502. doi: https://doi.org/10.1016/j.jaerosci.2005.04.003. URL https://www.sciencedirect.com/science/article/pii/S0021850205000728.

[110] B. Erk, J. P. Müller, C. Bomme, R. Boll, G. Brenner, H. N. Chapman, J. Correa, S. Düsterer, S. Dziarzhytski, S. Eisebitt, H. Graafsma, S. Grunewald, L. Gumprecht, R. Hartmann, G. Hauser, B. Keitel, C. von Korff Schmising, M. Kuhlmann, B. Manschwetus, L. Mercadier, E. Müller, C. Passow, E. Plönjes, D. Ramm, D. Rompotis, A. Rudenko, D. Rupp, M. Sauppe, F. Siewert, D. Schlosser, L. Strüder, A. Swiderski, S. Techert, K. Tiedtke, T. Tilp, R. Treusch, I. Schlichting, J. Ullrich, R. Moshammer, T. Möller, and D. Rolles. CAMP@FLASH: an end-station for imaging, electron- and ion-spectroscopy, and pump–probe experiments at the FLASH free-electron laser. *J. Synchrotron Rad.*, 25(5):1529–1540, September 2018. doi: 10.1107/S1600577518008585. URL https://doi.org/10.1107/S1600577518008585.

[111] J. N. Clark, L. Beitra, G. Xiong, A. Higginbotham, D. M. Fritz, H. T. Lemke, D. Zhu, M. Chollet, G. J. Williams, M. Messerschmidt, B. Abbey, R. J. Harder, A. M. Korsunsky, J. S. Wark, and I. K. Robinson. Ultrafast Three-Dimensional Imaging of Lattice Dynamics in Individual Gold Nanocrystals. *Science*, 341(6141):56–59, 2013. doi: 10.1126/science.1236034. URL https://www.science.org/doi/abs/10.1126/science.1236034.

[112] M. F. Hantke, T. Ekeberg, and F. R. N. C. Maia. *Condor*: a simulation tool for flash x-ray imaging. *J. Appl. Cryst.*, 49(4):1356–1362, Aug 2016. doi: 10.1107/S1600576716009213. URL https://doi.org/10.1107/S1600576716009213.

[113] D. Höing, R. Salzwedel, L. Worbs, Y. Zhuang, A. Samanta, J. Lübke, A. D. Estillore, K. Dlugolecki, C. Passow, B. Erk, N. Ekanayake, D. Ramm, J. Correa, C. C. Papadopoulou, A. T. Noor, F. Schulz, M. Selig, A. Knorr, K. Ayyer, J. Küpper, and H. Lange. Optically induced electron density gradients drive coherent plasmonic nanoparticle oscillations, 2022. in preparation.

[114] J. Stark and G. Wendt. Beobachtungen über den Effekt des elektrischen Feldes auf Spektrallinien. II. Längseffekt. *Ann. Phys.*, 348(7):983–990, 1914. ISSN 1521-3889. doi: 10.1002/andp.19143480703. URL http://dx.doi.org/10.1002/andp.19143480703.

[115] J. Lübke. *Control of Bionanoparticles with Electric Fields*. Dissertation, Universität Hamburg, Hamburg, Germany, 2022. in preparation.

[116] M. Amin, H. Samy, and J. Küpper. Robust and accurate computational estimation of the polarizability tensors of macromolecules. *J. Phys. Chem. Lett.*, 10:2938–2943, April 2019. doi: 10.1021/acs.jpclett.9b00963. URL https://dx.doi.org/10.1021/acs.jpclett.9b00963.

[117] M. Amin, J.-M. Hartmann, A. K. Samanta, and J. Küpper. Analysis of laser-induced alignment of nanoparticles and macromolecules for imaging applications. 2022. in preparation.

[118] H. Stapelfeldt and T. Seideman. Colloquium: Aligning molecules with strong laser pulses. *Rev. Mod. Phys.*, 75(2):543–557, 2003. doi: 10.1103/RevModPhys.75.543. URL http://link.aps.org/abstract/RMP/v75/p543.

[119] E. T. Karamatskos, S. Raabe, T. Mullins, A. Trabattoni, P. Stammer, G. Goldsztejn, R. R. Johansen, K. Długołęcki, H. Stapelfeldt, M. J. J. Vrakking, S. Trippel, A. Rouzée, and J. Küpper. Molecular movie of ultrafast coherent rotational dynamics of OCS. *Nat. Commun.*, 10:3364, 2019. doi: 10.1038/s41467-019-11122-y. URL https://dx.doi.org/10.1038/s41467-019-11122-y.

[120] M. Yon, C. Pibourret, J.-D. Marty, and D. Ciuculescu-Pradines. Easy colorimetric detection of gadolinium ions based on gold nanoparticles: key role of phosphine-sulfonate ligands. *Nanoscale Adv.*, 2:4671–4681, 2020. doi: 10.1039/D0NA00374C. URL http://dx.doi.org/10.1039/D0NA00374C.

Acronyms

1D	one dimensional
2D	two dimensional
3D	three dimensional
ADL	aerodynamic lens
ALS	aerodynamic lens stack
AuNP	gold nanoparticle
BGC	buffer-gas cell
BGC-ALS	buffer-gas cell aerodynamic lens stack
BSA	Bovine serum albumin
CAMP	CFEL-ASG Multi-Purpose instrument
CEM	cryo-electron microscopy
CPC	condensation particle counter
CW	continuous wave
DMA	differential-mobility-analyzer
ESI	electrospray ionization
FLASH	Free-Electron Laser in Hamburg
FWHM	full width at half maximum
GDVN	gas-dynamic virtual nozzle
ID	inner diameter
LIBD	laser-induced breakdown detection
LSI	light-sheet imaging
Nd:YAG	neodymium-doped yttrium aluminum garnet
NMR	nuclear magnetic resonance spectroscopy
NP	nanometer-sized particles / nanoparticles
PS	polystyrene sphere
SFX	Serial femtosecond x-ray crystallography
SPI	Single-particle x-ray coherent diffractive imaging
SVI	side-view imaging
TA	transient absorption
TEM	transmission electron microscopy
ToF	time-of-flight
XFEL	x-ray free-electron laser

Acknowledgments

This thesis is not the result of me working alone. It is built on discussion, motivation, collaborative laboratory work and the result of available funding by Deutsches Elektronen-Synchrotron DESY. The importance of working together became evident when home office, lab restrictions and other social distancing rules were enforced during my PhD time. Especially then, I was thankful for all the support, motivation and scientific discussions we all had online.

First, I thank Jochen Küpper, my supervisor for this project for a place in the Controlled Molecule Imaging group at CFEL and this overall opportunity. I am thankful for the scientific input and especially the opportunities to join various beamtimes during my PhD studies. I thank Holger Lange as my co-supervisor of this thesis. I am grateful for endless support from Amit Samanta as a team leader, as scientific coordinator and as mentor in general discussions about the research world. I left every discussion with motivation to work and explore the data further. Thank you for this!

A special thanks goes to all former and current CMI PhD students I got to know, especially Nils Roth, Joss Wiese, Helen Bieker and Melby Johny. In my memory you will remain the cool senior PhD gang I looked up to and who inspired me. I am happy we spent long coffee breaks and lunches talking and you showed me that those breaks for socializing are just as important as spending long days in the lab taking data. I am grateful you showed me there is an end to a PhD thesis and our careers are just starting. A big thank you goes to Nils Roth, who passed on his knowledge about the experimental setup and the simulation framework. Your experimental setup is still alive and already passed on to the next generation. Your efforts are very much appreciated and we were able to turn your setup into the paper-fabrication machine of the lab. Jannik Lübke, thank you for fighting through our PhD studies together. I am thankful we worked together so much in the lab and sharing offices, (not) understanding the data, improving the setup and that we kept on motivating each other. We are almost there! I am grateful for all the aerosol knowledge gained from Armando Estillore and all the nice lab distractions. Danke, Armando. I thank Nidin Vadassery for the newly gained knowledge about coffee and generally interesting conversations in the office and Guang Yang for working late writing our theses and motivational speeches.

I thank the whole CMI group and especially the COMOTION team for scientific discussions, lab assistance and fun at other occasions.

I thank everyone I met during beamtimes. Spending night shifts with scientific nonsense discussions was my favorite part besides knowing there are scientists out there interested in what we were doing and realizing how much can be achieved with team work in a short time.

Outside of the research group, I thank Mabel Ruiz-López for her mentoring and keeping my mind open for an academic career. Your words motivated me immensely and were in fact the push I needed. In addition, I thank the mentoring program DynaMENT with all the workshops, interesting and fruitful discussions with the other mentees about our situations and motivation coming from each time we met. Thank you to the people within the DESY-PR tours, opening my scientific horizon to the research on campus, networking and having fun while communicating science. I thank everyone I met on campus for long scientific and general academic structure discussions, for

motivation when needed and distraction when urgently needed. I thank the PIER graduate school for all the nice events to bring together PhD students from campus, creating a nice atmosphere to talk to others and interesting lectures and seminars.

For motivation and support from outside the campus, I thank my family and friends. I want to mention in particular Clara, Felix and Ivonne. Finally, I thank René for the motivation in the past months to finish this work and the ability to turn off my overthinking head distracting me from all of this.

List of publications

Publications within this thesis

- L. Worbs, J. Lübke, N. Roth, A. K. Samanta, D. A. Horke, and J. Küpper. Light-sheet imaging for the recording of transverse absolute density distributions of gas-phase particle-beams from nanoparticle injectors. *Opt. Exp.*, 27:36580–36586, March 2019. doi: 10.1364/OE.27.036580. URL `https://doi.org/10.1364/OE.27.036580`

- L. Worbs, N. Roth, J. Lübke, A. D. Estillore, P. L. Xavier, A. K. Samanta, and J. Küpper. Optimizing the geometry of aerodynamic lens injectors for single-particle coherent diffractive imaging of gold nanoparticles. *J. Appl. Cryst.*, 54(6):1730–1737, December 2021. doi: 10.1107/S1600576721009973. URL `https://arxiv.org/abs/2105.15084`

- L. Worbs, J. Lübke, A. D. Estillore, A. K. Samanta, and J. Küpper. Understanding the focusing behavior of small nanoparticles upon pressure changes. *J. Phys. Chem. C*, 2022. in preparation

- L. Worbs, A. D. Estillore, A. K. Samanta, and J. Küpper. Toward cryogenically-cooled particle beams of small nanoparticles and proteins. *Rev. Sci. Instrum.*, 2022. in preparation

Publications I have contributed to during my PhD study

- A. K. Samanta, M. Amin, A. D. Estillore, N. Roth, L. Worbs, D. A. Horke, and J. Küpper. Controlled beams of shockfrozen, isolated, biological and artificial nanoparticles. *Struct. Dyn.*, 7:024304, 2020. doi: 10.1063/4.0000004. URL `https://doi.org/10.1063/4.0000004`

- J. Lübke, N. Roth, L. Worbs, D. A. Horke, A. D. Estillore, A. K. Samanta, and J. Küpper. Charge-state distribution of aerosolized nanoparticles. *J. Phys. Chem. C*, 125(46):25794–25798, 2021. doi: 10.1021/acs.jpcc.1c06912. URL `https://doi.org/10.1021/acs.jpcc.1c06912`

- N. Roth, D. Horke, J. Lübke, A. K. Samanta, A. D. Estillore, L. Worbs, N. Pohlman, K. Ayyer, A. Morgan, H. Fleckenstein, M. Domaracky, B. Erk, C. Passow, J. Correa, O. Yefanov, A. Barty, M. Prasciolu, S. Bajt, R. Kirian, H. Chapman, and J. Küpper. New aerodynamic lens injector for single particle diffractive imaging. *Rev. Sci. Instrum.*, 2021. submitted

- K. Ayyer, P. L. Xavier, J. Bielecki, Z. Shen, B. J. Daurer, A. K. Samanta, S. Awel, R. Bean, A. Barty, M. Bergemann, T. Ekeberg, A. D. Estillore, H. Fangohr, K. Giewekemeyer, M. S. Hunter, M. Karnevskiy, R. A. Kirian, H. Kirkwood, Y. Kim, J. Koliyadu, H. Lange, R. Letrun, J. Lübke, T. Michelat, A. J. Morgan, N. Roth, T. Sato, M. Sikorski, F. Schulz, J. C. H. Spence, P. Vagovic, T. Wollweber, L. Worbs, O. Yefanov, Y. Zhuang, F. R. N. C. Maia, D. A. Horke, J. Küpper, N. D. Loh, A. P. Mancuso, and H. N. Chapman. 3D diffractive imaging of nanoparticle ensembles using an x-ray laser. *Optica*, 8(1):15–23, Jan 2021. doi:

10.1364/OPTICA.410851. URL http://www.osapublishing.org/optica/abstract.cfm?URI=optica-8-1-15

- Y. Zhuang, S. Awel, A. Barty, R. Bean, J. Bielecki, M. Bergemann, B. J. Daurer, T. Ekeberg, A. D. Estillore, H. Fangohr, K. Giewekemeyer, M. S. Hunter, M. Karnevskiy, R. A. Kirian, H. Kirkwood, Y. Kim, J. Koliyadu, H. Lange, R. Letrun, J. Lübke, A. Mall, T. Michelat, A. J. Morgan, N. Roth, A. K. Samanta, T. Sato, Z. Shen, M. Sikorski, F. Schulz, J. C. H. Spence, P. Vagovic, T. Wollweber, L. Worbs, P. L. Xavier, O. Yefanov, F. R. N. C. Maia, D. A. Horke, J. Küpper, N. D. Loh, A. P. Mancuso, H. N. Chapman, and K. Ayyer. Unsupervised learning approaches to characterizing heterogeneous samples using x-ray single-particle imaging. *IUCrJ*, 9(2):204–214, Mar 2022. doi: 10.1107/S2052252521012707. URL https://doi.org/10.1107/S2052252521012707

- T. Ekeberg, D. Assalauova, J. Bielecki, R. Boll, B. J. Daurer, L. A. Eichacker, L. E. Franken, D. E. Galli, L. Gelisio, L. Gumprecht, L. H. Gunn, J. Hajdu, R. Hartmann, D. Hasse, A. Ignatenko, J. Koliyadu, O. Kulyk, R. Kurta, M. Kuster, W. Lugmayr, J. Lübke, A. P. Mancuso, T. Mazza, C. Nettelblad, Y. Ovcharenko, D. E. Rivas, M. Rose, A. K. Samanta, P. Schmidt, E. Sobolev, N. Timneanu, S. Usenko, D. Westphal, T. Wollweber, L. Worbs, P. L. Xavier, H. Yousef, K. Ayyer, H. N. Chapman, J. A. Sellberg, C. Seuring, I. A. Vartanyants, J. Küpper, M. Meyer, and F. R. Maia. Observation of a single protein by ultrafast x-ray diffraction. *bioRxiv*, 2022. doi: 10.1101/2022.03.09.483477. URL https://www.biorxiv.org/content/early/2022/03/12/2022.03.09.483477

Earlier publications

- D. A. Horke, N. Roth, L. Worbs, and J. Küpper. Characterizing gas flow from aerosol particle injectors. *J. Appl. Phys.*, 121(12):123106, 2017. doi: 10.1063/1.4978914. URL http://dx.doi.org/10.1063/1.4978914

Eidesstattliche Versicherung

Hiermit versichere ich an Eides statt, die vorliegende Dissertationschrift selbst verfasst und keine anderen als die angegebenen Hilfsmittel und Quellen benutzt zu haben. Die Dissertation wurde in der vorgelegten oder einer ähnlichen Form nicht schon einmal in einem früheren Promotionsverfahren angenommen oder als ungenügend beurteilt.

Hamburg, den 18. Oktober 2022

Lena Worbs